

Estimating the magnetic field strength in the interstellar medium



Raphael Skalidis

Supervisor: Konstantinos Tassis

Department of Physics
University of Crete

This dissertation is submitted for the degree of
Doctor of Philosophy

October 2022

To my loving parents and uncle, Dr. K. Christidis, who introduced me to the magical world of science.

Declaration

I hereby declare that except where specific reference is made to the work of others, the contents of this dissertation are original and have not been submitted in whole or in part for consideration for any other degree or qualification in this, or any other university. This dissertation is my own work and contains nothing which is the outcome of work done in collaboration with others, except as specified in the text and Acknowledgements.

Raphael Skalidis
October 2022

Acknowledgements

I would like to express my deepest gratitude to K. Tassis for being an inspiring mentor, and V. Pavlidou for the excellent collaboration we had all these years. I would like to thank my PhD defense committee: P. André, J. Tan, I. Papadakis, J. Antoniadis, V. Charmandaris, and A. Zezas. I also thank G. V. Panopoulou, V. Pelgrims, and A. Tritsis for being excellent friends and collaborators, and J. Sternberg, J. R. Beattie, who contributed in some of the published works presented in this thesis. I would like to thank all the graduate students at the Institute of Astrophysics: E. Kiritsis, M. Kopsacheili, A. Konstantinou, N. Mandarakas, G. Korkidis, A. Tsouros, S. Romanopoulos, R. Fernandez, and K. Kovlakas and the members of the Institute of Astrophysics: N. D. Kylafis, A. C. S Readhead, P. Reig, T. Diaz, C. Casadio, E. Tsenteliero, P. Evangelopoulos, A. Steiakaki, T. Kougentakis, G. Paterakis, V. Pantoulas, M. Paleologou, I. Leonidaki, G. Maravelias, E. Notrmousi, K. Anastasopoulou, I. Liodakis, K. Gkimisi, and F. Bouzelou. My deepest gratitude to P. Kallemi for being an excellent companion during the PhD years and for her constant moral support. I would like to thank all the people whose feedback helped us to improve the quality of the published works and the PASIPHAE, and RoboPol collaborations. This thesis has received funding from the European Research Council (ERC) under the European Unions Horizon 2020 research and innovation programme under grant agreement No. 771282.

Abstract

A large scale magnetic field permeates the interstellar medium (ISM) of our Galaxy. The ISM magnetic field strength is notoriously difficult to measure, and for this reason there is a longstanding debate about its dynamical importance in the star formation process. The magnetic field strength can be directly measured, with the Zeeman effect, only in a limited number of cases. For this reason, indirect methods have been developed for estimating the magnetic field strength. The most widely accessible methods are based on dust polarization. Dust polarization probes directly the plane-of-the-sky magnetic field morphology, but not its strength. These indirect magnetic field strength estimation methods are based on the energy balance of incompressible turbulence. Observations, however, indicate that turbulence in the ISM is highly compressible, hence the assumptions of the existing methods are incompatible with the observations. In this thesis, we propose a novel method for estimating the magnetic field strength from dust polarization based on the energetics of compressible turbulence. We assess the accuracy of the proposed method with synthetic data produced from a suite of numerical simulations. We find that with the proposed method an accuracy better than a factor of two can be achieved.

Table of contents

List of figures	xiii
List of tables	xv
Nomenclature	xvii
1 Introduction	1
1.1 Competing forces in star formation	2
1.1.1 The role of gravity	2
1.1.2 The role of magnetic fields	3
1.1.3 The role of turbulence	4
1.2 Probing the ISM magnetic field	5
1.2.1 Direct detection of the ISM magnetic field strength	6
1.2.2 Indirect estimates of the magnetic field strength	7
2 Numerical simulations	11
3 Overview of past methods	13
3.1 Classical DCF method	13
3.1.1 Foundations of the method	13
3.1.2 Caveats of the method	14
3.2 HH09 method	19
3.2.1 Foundations of the method	19
3.2.2 Caveats of the method	20
4 Compressible sub-Alfvénic turbulence energetics	23
4.1 Lagrangian formulation	25
4.2 Energetics	31
4.3 Comparison against numerical simulations	34

5	A new method for estimating the magnetic field strength from dust polarization	35
5.0.1	An analogy with gravity	39
5.0.2	Comments on the assumptions and approximations of the proposed method	43
6	Numerical assessment of interstellar magnetic field strength estimation methods	45
6.0.1	How good are the energy equipartition assumptions?	45
6.0.2	How does the forcing affect the energetics?	46
6.0.3	Testing HH09 with 3D simulations	48
6.1	Testing scalings with numerical simulations	52
6.2	Applying the DCF and the proposed method in synthetic data	53
6.2.1	Statistical properties of ϵ_{DCF} and ϵ_{ST}	56
6.2.2	How does forcing affect the polarization data?	56
7	Conclusions	61
	References	65
	Appendix A Dispersion function fitting	83

List of figures

3.1	Distribution of the synthetic polarization angles for different simulation models. Black histogram corresponds to observations weighted by density, while the red one without the density weighting. Left: Simulation model with $M_S = 0.7$, Middle: Simulation model with $M_S = 2.0$, Right: Simulation model with $M_S = 7.0$	15
4.1	Comparison between analytical and numerical results. Solid and dashed thick black lines correspond to the $E_{\text{harmonic}}/E_{\text{coupling}}$ ratio obtained analytically for $\mathcal{M}_A \rightarrow 0$ ($\zeta = 0$) and $\mathcal{M}_A \rightarrow 1$ ($\zeta = \sqrt{2}$) respectively. Numerical data are shown with colored dots. The blue line corresponds to the analytically-obtained $E_{\text{kinetic}}/E_{\text{coupling}}$ ratio, while colored triangles show the same quantities calculated from numerical data. Red boxes correspond to $E_{\text{kinetic}}/E_{\text{m,total}}$. The thin green line shows energy terms in equipartition. The colorbar shows the sonic Mach number (\mathcal{M}_s) of the simulations.	33
5.1	Ratio of perpendicular over parallel LOS averaged magnetic field fluctuations.	38
6.1	Relative ratio of kinetic over magnetic energy density using Eq. (3.2) (vertical axis) and Eq. (5.2) (horizontal axis). Colors correspond to different \mathcal{M}_A as shown in the legend. Dots correspond to simulations with $\mathcal{M}_s < 1$, "x" to $1 < \mathcal{M}_s \leq 4$ and triangles to $\mathcal{M}_s > 4$	46
6.2	Same as in Fig. 6.1, but the dots correspond to models driven with a mixture of compressible and solenoidal modes and "x" denotes models driven solenoidally.	47
6.3	Black dots correspond to the dispersion function computed using Eq. (3.13) for the $M_S = 0.7$ model. The model fit at large scales is shown with the black broken curve. Blue points mark the dispersion function subtracted with the black broken line and the blue line shows the fit of Eq. (6.1).	49
6.4	Absolute relative deviation ($ \varepsilon $) of each method estimate for the different simulation models. All the models have $\mathcal{M}_A = 0.7$	51

6.5	Polarization angle dispersion as a function of the Alfvénic Mach number. Blue line: scaling of the proposed method; magenta line: DCF scaling. The two lines are normalized so that they pass through the data for $\mathcal{M}_A = 1.0$	53
6.6	Left panel: Relative error of the DCF method versus the relative error of the ST method. Colors correspond to different \mathcal{M}_A as shown in the legend. Dots correspond to simulations with $\mathcal{M}_s < 1$, "x" to $1 < \mathcal{M}_s \leq 4$, and triangles to $\mathcal{M}_s > 4$. The black dotted box marks the zoomed in region shown in the right panel. Right panel: Zoomed region of the left panel.	54
6.7	Left panel: Kernel density estimation of ε_{DCF} for different \mathcal{M}_A simulations. Right panel: Zoomed in region of the left panel.	55
6.8	Kernel density estimation of ε_{ST} of simulations with different \mathcal{M}_A	57
6.9	Polarization angle distributions for two different simulations with $\mathcal{M}_A = 2.0$ and $\mathcal{M}_s = 2.0$. Black histogram corresponds to solenoidally driven cloud, while the blue to mixed forcing. Both histograms are normalized by dividing each bin with the total number of measurements. The legend shows the type of forcing.	59
A.1	As in Fig. 6.3 for the simulation models with $M_s = 1.2 - 7.0$	84

List of tables

6.1	3D MHD simulations	48
6.2	Simulation properties and methods results.	58
A.1	Fitting parameters of the HH09 method.	83

Nomenclature

ρ	Gas volume density
c_s	sound speed
n	Gas number density
B_{LOS}	Line-of-sight magnetic field component
\vec{B}_0	Initial magnetic field component
B_{POS}	Plane-of-the-sky magnetic field component
\vec{B}_t or $\delta\vec{B}$	Perturbed magnetic field component
\mathcal{M}_A	Alfvénic Mach number
\mathcal{M}_S	Sonic Mach number
χ or θ	Polarization angle
V_A	Alfvénic speed
$\delta\theta$ or $\delta\chi$	Dispersion of polarization angles
EVPA	Polarization angle
LOS	Line of sight
POS	Plane of the sky

Chapter 1

Introduction

"The nitrogen in our DNA, the calcium in our teeth, the iron in our blood, the carbon in our apple pies were made in the interiors of collapsing stars. We are made of starstuff", Carl Sagan.

The interstellar medium (ISM) is the space between stars and consists of radiation, magnetic fields, and matter (gas and dust). The ISM matter can be found in three stable phases, where gas heating balances cooling [52, 119]: 1) the cold neutral medium (CNM), 2) the warm neutral medium (WNM), and 3) the warm ionized medium (WIM). In the CNM, temperature (T) ranges from 10 up to 500 K while densities are $n \geq 50 \text{ cm}^{-3}$, in the WNM $T \sim 10^3 - 10^4 \text{ K}$ and $n \sim 0.1 \text{ cm}^{-3}$, while in the WIM $T \sim 10^4 \text{ K}$ and $n \sim 0.1 \text{ cm}^{-3}$. There is also an unstable phase, referred to as the lukewarm neutral medium (LNM), where gas is exchanged between WNM and CNM [157, 73, 91]. It is considered that colder and denser phases are embedded within warmer and more diffuse phases [119]. Therefore, CNM, and WIM have the minimum and maximum volume filling factors in the ISM respectively. Star formation takes place in CNM overdensities (clouds).

CNM clouds can be classified into three different classes, based on the atomic-to-molecular hydrogen abundance [17]: 1) atomic clouds with $\log N_{\text{H}} \lesssim 20 \text{ cm}^{-2}$, where gas is mostly atomic, 2) transition clouds with $20 \lesssim \log N_{\text{H}} \lesssim 21 \text{ cm}^{-2}$, where gas is mixed with both atomic and molecular hydrogen, and 3) molecular clouds with $\log N_{\text{H}} > 22 \text{ cm}^{-2}$, where hydrogen is molecular.

Stars form in molecular clouds because only there gravitational energy is sufficient, due to high densities, to initiate the gravitational collapse. However, self-gravity is not the only force exerted in molecular clouds. There are three kinds of pressure which oppose self-gravity: 1) thermal, 2) turbulent, and 3) magnetic pressure. Only thermal pressure can be neglected since typical temperatures in ISM molecular clouds are very low, $T \sim 10 \text{ K}$.

There is a longstanding debate on the relative role of turbulence and magnetic fields in the star formation process [118]. The debate is open for decades, because kinetic and magnetic energies are in rough equipartition in the ISM [44], and thus it is challenging to distinguish the dominant component (turbulence or magnetic fields). In order to study the relative ratio between turbulence and magnetic pressure we need high accuracy measurements of the magnetic field properties. For this reason, some of the most important questions in the star formation process are still open [95], e.g.: Why is the star formation rate in our galaxy so low ($\sim 1.3 \text{ M}_\odot/\text{yr}$) compared to the total mass reservoir of the ISM gas which suggests that the star formation rate should be of the order $\sim 100 \text{ M}_\odot/\text{yr}$ [188, 189, 47]? What is the characteristic timescale of star formation? What is the origin of the initial mass function? Depending on whether we consider turbulence or magnetic fields as dominant we obtain different answers. Below we briefly explain the role of each of the three major "players", gravity, turbulence, and magnetic fields in the star formation process.

1.1 Competing forces in star formation

1.1.1 The role of gravity

A spherical cloud supported only by its own thermal pressure is gravitationally unstable under perturbations with wavelengths $\lambda > \lambda_J$, where λ_J is the Jeans' length defined as $\lambda_J = c_s \sqrt{\pi/G\rho}$, c_s is the sound speed, ρ is the gas density, and G the gravitational constant. This is called the Jeans instability [87]. In that case, a cloud would collapse due to its own self-gravity. On the other hand, if $\lambda < \lambda_J$ a cloud would remain gravitationally stable. According to Jeans' model, the collapse of an unstable cloud happens at the free-fall time, which in that case represents the characteristic timescale of star formation, and is [118],

$$t_{ff} = 1.37 \times 10^6 \left(\frac{10^3 \text{ cm}^{-3}}{n} \right) \text{ yr}. \quad (1.1)$$

Jeans' instability leads naturally to hierarchical fragmentation [85]. According to the so-called hierarchical collapse model when the global collapse of a cloud is initiated, then the density of the cloud increases, hence λ_J can decrease locally. As a result, during the cloud collapse there are several sub-regions within the parent cloud satisfying the gravitational collapse criterion ($\lambda > \lambda_J$). As time progresses, λ_J keeps decreasing, and hence even more sub-regions satisfy the gravitational collapse condition. This means that the gravitational collapse is transferred from cloud to smaller scales, hence forming a cascade-like behaviour of mass transfer [71, 181, 182, 187, 101, 183]. This hierarchical fragmentation ends when

monolithic structures have been formed at very small scales, i.e. stars. It has been proposed that low mass stars are born first at Myrs timescales, while after a few Myrs more massive stars form [183]. The low star formation efficiency can be attributed to feedback processes [e.g., 173] from newly born stars which slow down the formation of next generation stars.

1.1.2 The role of magnetic fields

The ISM of our Galaxy is magnetized [e.g., 80, 153]. For magnetized clouds, it is essential to introduce the mass-to-flux ratio (μ_ϕ) defined as the ratio between the self-gravitating mass and the magnetic flux. Clouds can collapse only if μ_ϕ is larger than a critical value, which is $\mu_{\phi,cr} = 1/\sqrt{63G}$ [134]. In that case self-gravity dominates over magnetic pressure and clouds are considered to be super-critical. If $\mu_\phi < \mu_{\phi,cr}$, then the cloud is considered to be magnetically supported and cannot collapse, (sub-critical cloud); even moderate magnetic field strengths, $\sim 1\mu\text{G}$, can prevent a cloud from collapsing, provided that the magnetic field is frozen in the gas [28, 120]. Flux-freezing (or Alfvén's theorem) [1] states that in a medium with infinite conductivity, gas is perfectly attached to the field lines, and magnetic flux is preserved. For example, if we consider a spherical cloud with an initial radius R_0 and magnetic field strength B_0 , and then compress the size of the cloud by a factor of 10, ($R_1 = 0.1R_0$), then the magnetic field strength would become 100 times larger than the initial field. The contraction of a cloud keeps increasing the magnetic flux and thus the gravitational force will eventually be balanced by magnetic pressure, if the cloud is initially sub-critical. Since magnetic forces are exerted perpendicular to the field lines, clouds are magnetically supported only perpendicular to them, while along the field lines gas can free stream and collapse. This process is known as non-homologous collapse and leads to oblate cloud shapes [129, 131].

Flux freezing is an accurate approximation when gas densities are relatively small, $n \sim 100 \text{ cm}^{-3}$, and the ionization fraction of a cloud is high due to the penetrating UV interstellar radiation, hence the conductivity is high. However, as density increases the ionization rate is significantly reduced in the interior of a cloud. The reason is that density enhancements can shield the interior of the clouds from the ISM radiation field [67]. Lower ionization means that the collision rate between ions and neutrals is reduced. Magnetic forces are directly exerted on the ions and indirectly to neutrals, since ions drag neutrals due to collisions. If the ion-neutral collision rate is reduced, then neutrals are not perfectly dragged by ions hence a velocity drift between the two species is induced. This process is known as *ambipolar diffusion*.

There are two types of ambipolar diffusion processes: magnetically-, and gravitationally-driven ambipolar diffusion [133]. Magnetically-driven ambipolar diffusion refers to the

relative drift between neutrals and ions due to their imperfect coupling and can be present even in the absence of self-gravity. On the other hand, gravitationally-driven ambipolar diffusion takes place when overdensities have been formed and act as local centers of gravity by attracting preferentially neutral gas, since the attraction of the ionized gas is balanced by magnetic forces. Magnetically-driven diffusion precedes and may lead to the onset of gravitationally-driven ambipolar diffusion (by dissipating turbulence and hence any extra support by turbulent pressure), which tends to increase μ_ϕ in the inner parts of a cloud and initiate the gravitational collapse when the critical value is exceeded.

The characteristic timescale of magnetically-driven ambipolar diffusion is [133],

$$\tau_{\text{AD,m}} \approx 7.5^5 \left(\frac{\lambda}{1\text{pc}} \right)^2 \left(\frac{30\mu\text{G}}{B} \right)^2 \left(\frac{n}{2 \times 10^3 \text{cm}^{-3}} \right)^2 \left(\frac{\chi_{i,o}}{2 \times 10^{-7}} \right) \text{yr}, \quad (1.2)$$

where $\chi_{i,o}$ is the gas ionization, and λ is the wavelength of waves propagating in the cloud. The timescale of gravitationally-driven ambipolar diffusion is [133],

$$\tau_{\text{AD,g}} \approx 1.1 \times 10^6 \left(\frac{\chi_{i,o}}{10^{-7}} \right). \quad (1.3)$$

Ambipolar diffusion sets the magnetically-driven star formation timescale which could be up to an order of magnitude larger than the free-fall time [175, 135, 10]. The magnetized star formation process is significantly slower than the non-magnetized, and this can explain the low star formation rate [47].

1.1.3 The role of turbulence

If we ignore magnetic fields, and consider that clouds are "born" super-critical ($\mu_\phi > \mu_{\phi,cr}$) [97, 98, 96], then only turbulence pressure can withstand self-gravity.

In the turbulence-driven star formation scenario the sonic length scale (λ_s) defines the scale where turbulent motions transition from supersonic ($\mathcal{M}_s > 1$) to subsonic ($\mathcal{M}_s < 1$) [51]; \mathcal{M}_s is the sonic Mach number. Numerical simulations [51] show that λ_s is strongly correlated with the formation of filamentary structures in clouds. Filaments have been widely observed in ISM clouds and observations show that they host protostellar objects [7, 125]. However, the sonic scale theories do not take into account the observational evidence that filaments are significantly affected by magnetic fields [6, 143, 115, 116, 145].

A brief overview of the sonic scale theories [97] is the following: Consider a cloud which is initially spherical with uniform density. If the cloud is highly supersonic, $\mathcal{M}_s \sim 10$ [90], then turbulent flows will form local regions of highly compressed gas. These local overdensities are the sites where gas can become gravitationally unstable, since thermal and

turbulent pressure cannot withstand self-gravity. The necessary condition for collapse is $\lambda_J < \lambda_s$. This theory postulates that molecular cloud density distributions are log-normal. Log-normal density distributions are found in many kinds of numerical simulations [16, 180, 146, 124]. Observations had originally been thought to show log-normal density distributions [89], though recent evidence suggests that observational uncertainties may be hampering our ability to measure them [2]. Regions satisfying the gravitational collapse condition lie at the tails of the log-normal density distribution, which correspond to a minor fraction of the cloud, while the majority of the cloud remains supported due to turbulence pressure ($\lambda_J > \lambda_s$). It is important to note that the two forms of the Kennicutt-Schmidt relation [158, 159, 93, 92] naturally arise from this theory.

1.2 Probing the ISM magnetic field

The major difference between the various star formation theories is the assumed initial conditions regarding the magnetization level of ISM clouds. If clouds were initially sub-critical ($\mu_\phi < \mu_{\phi,cr}$) [30], then collapse could only happen through ambipolar diffusion, because otherwise magnetic forces would support a cloud against its self-gravity. On the other hand, if clouds were initially super-critical ($\mu_\phi > \mu_{\phi,cr}$), then collapse could happen in highly compressed regions due to supersonic turbulent flows or due to gravitational hierarchical collapse.

The mass-to-flux ratio of ISM clouds can be observationally constrained from the magnetic field strength versus density relation, $B \propto n^\alpha$ where α is a proxy of μ_ϕ . When $\alpha = 2/3$, then the collapse is homologous, which is realizable only in clouds with dynamically insignificant magnetic field, while for $\alpha = 1/2$ the collapse is non-homologous as indicated by the ambipolar diffusion theory, which means that clouds could be initially sub-critical [177]. We need high accuracy measurements of the magnetic field strength in order to be able to distinguish the two α indices. The question is, how well can we measure the ISM magnetic field properties?

There are five observables tracing the ISM magnetic field properties:

- *Zeeman effect*: Data of Zeeman splitting of atomic or molecular emission lines. With these data one can directly probe the magnitude and orientation of the line of sight (LOS) component of the magnetic field [39, 40].
- *Faraday rotation*: Tracing the rotation of polarization angle of a radio polarization signal as it passes through the ISM [170–172]. Faraday rotation is the integrated product of thermal electron density and the LOS magnetic field strength.

- *Synchrotron Radiation*: Radiation emitted when relativistic charged particles are accelerated. Synchrotron radiation traces the plane of the sky (POS) orientation of the magnetic field.
- *Goldreich-Kylafis (GK) effect*: Emission lines get polarized due to anisotropies in the radiation transfer induced by magnetic fields. The imparted polarization can be either parallel or perpendicular to the magnetic field [63, 64].
- *Dust polarization*: Probes the density-weighted magnetic field orientation in the POS [4].

1.2.1 Direct detection of the ISM magnetic field strength

Zeeman is the only observable which traces directly the amplitude of the LOS magnetic field component in CNM clouds. Using Zeeman data, Crutcher et al. [40] found that the maximum total magnetic field strength scales as,

$$B \propto \begin{cases} \text{constant}, & n \leq 300 \text{ cm}^{-3} \\ n^{2/3}, & n > 300 \text{ cm}^{-3} \end{cases} \quad (1.4)$$

The same authors concluded that the $2/3$ scaling is consistent with spherically collapsing cores where the magnetic field has but a minor role in the cloud dynamics, which means that clouds should have been "born" super-critical. In addition, they mentioned that $\alpha = 0$ at $n \leq 300 \text{ cm}^{-3}$ because gas accumulates preferentially along the magnetic field lines. However, the data of Crutcher et al. [40] are noisy and in order to reach to the aforementioned scalings (Eq. 1.4), they relied on several prior assumptions applied within a Bayesian framework. For this reason, the conclusions of Crutcher et al. [40] have been questioned [177, 88].

Tritsis et al. [177] mentioned that the gas volume density uncertainties in the analysis of Crutcher et al. [40] have been significantly underestimated. These authors used the same Zeeman dataset, but considered only the most accurate density points. They concluded that the data are better described by $B \propto n^{1/2}$ at $n > 300 \text{ cm}^{-3}$ [177]. The $\alpha = 1/2$ scaling is consistent with the non-homologous collapse model, which is consistent with the ambipolar diffusion theory [130, 132]. Other authors [88] pointed out that the results of Crutcher et al. [40] are debatable since the Zeeman data are too noisy, hence their analysis is dominated by statistical biases.

There is also another caveat in the Zeeman analysis of Crutcher et al. [40]. Zeeman data trace the LOS magnetic field strength, while in order to constrain α , the total strength of the field is required. In order to overcome this problem Crutcher et al. [40] hypothesized that

the magnetic field inclination angle with respect to the LOS throughout their data sample is random; this allowed them to reconstruct the posterior distribution of the total magnetic field strength through a Bayesian analysis. However, it has been pointed out that there is a projection bias which tends to favor geometries where the magnetic field is mostly on the POS and not uniform [3, 148, 151].

The interpretation of the $B \propto n^\alpha$ constraints (Eq. 1.4) is complicated if we consider numerical simulations. Zeeman observations suggest that in the diffuse ISM, $n \leq 300 \text{ cm}^{-3}$, the α index is zero [40], while numerical simulations show that for these densities $\alpha > 0$ [155, 21].

Zeeman data are the only direct measurement of the ISM magnetic field strength. For this reason, Zeeman data were considered as the golden standard for assessing the role of the ISM magnetic field. However, these data are notoriously difficult to obtain, and as we mentioned above their interpretation is highly complex. Therefore, the question whether clouds are initially sub-, or super-critical is still open and Zeeman does not seem to be able to provide a robust way to attack this problem.

1.2.2 Indirect estimates of the magnetic field strength

Dust polarization is the most accessible observable, amongst the other, tracing the ISM magnetic field properties in CNM clouds. Dust polarization is induced by the interaction of the ISM magnetic field with aspherical dust grains. Aspherical grains align their short axis with the local magnetic field [41]. The prevailing theory suggests that this alignment happens due to radiative torques induced by radiation feedback [4, 5, 43, 45, 103]. Aligned dust grains act as polarizers and when starlight passes through a dusty cloud it gets preferentially extinct along the long dust grain axis, inducing polarization parallel to the magnetic field. In addition, the same dust grains emit thermally polarized radiation at sub-mm wavelengths; in this case the emission is polarized along the long axis of dust grains, which is perpendicular to the magnetic field. Both optical and sub-mm polarization trace accurately the magnetic field orientation in the plane of the sky (POS) [4, 164]; there is a π ambiguity in the polarization angle, hence only the orientation of the magnetic field can be constrained and not the direction of the field.

Dust polarization also traces the magnetic field properties of ISM clouds at various scales. There are several projection biases affecting the interpretation of dust polarization data [190], but they are usually densely sampled [115, 116, 144, 145, 38, 143, 152, 163, 9, 149], which allows us to use statistical tools to account for these biases. The major limitation is that dust polarization probes only the morphology of the magnetic field in the POS and not its

strength. However, there are indirect ways to infer the POS magnetic field strength from dust polarization maps, given some assumptions about the properties of the ISM clouds [42, 27].

The first method to estimate the magnetic field strength from dust polarization was presented by Davis [42] and Chandrasekhar and Fermi [27] (DCF). They assumed that magnetic field lines are distorted due to the propagation of the incompressible transverse magnetohydrodynamic (MHD) waves, known as Alfvén waves. This distortion induces spread in the polarization angle distribution, which, combined with the gas turbulent motions from spectroscopic data, allows the estimation of the true magnetic field strength. It was realized that external forces, like self-gravity, can bend the field lines and induce extra dispersion in the polarization angle distribution. In order to treat the problem, one can fit parabolas to the polarization data and remove the large-scale hour-glass bending from the polarization data of a pre-stellar core [62]. A similar, but more sophisticated approach, was followed by Pattle et al. [150]. On the other hand, Hildebrand et al. 2009 and Houde et al. 2009 [78, 84] (HH09) developed an analytical model for the polarization data, which measures the turbulence-induced spread in the presence of any external source of magnetic field bending. There are many modifications of the DCF method [72, 99, 48, 35, 186, 104] summarized in several reviews [148, 86, 149]. *All these methods rely on the assumption that the Alfvén waves are producing the observed polarization angle dispersion, and use the linewidths in the emission spectra to infer the turbulent velocity spreads.*

The interstellar medium (ISM) is, however, highly compressible [70] and other than the Alfvén waves, contains MHD wave modes that induce density compressions. These are known as fast and slow magnetosonic modes and their existence in astrophysical plasmas is inevitable because they are excited by the Alfvén waves [76]. In addition, the so-called entropy modes can contribute to the observed compressibility of the ISM [109], however they produce zero velocity and magnetic field fluctuations. Compressible modes have not been taken into account in the DCF method and this can lead to significant inaccuracies in the estimates.

DCF considered that the mean magnetic, $\langle \delta B^2 \rangle / (8\pi)$, and kinetic, $\rho \delta \langle u_{turb}^2 \rangle / 2$, energy densities reach an equipartition. However, numerical simulations of strongly magnetized and compressible turbulence show that the kinetic energy is always larger than the magnetic, i.e. $\rho \delta \langle u_{turb}^2 \rangle / 2 > \langle \delta B^2 \rangle / (8\pi)$ [72, 49, 108, 14] and that their ratio is a function of the strength of the initial magnetic field component (\vec{B}_0) [50, 108, 14, 161, 15]. For this reason, the classical DCF method (without an appropriately calibrated f factor) is found to be highly inaccurate when tested in compressible MHD simulations. There are several authors who attributed this bias to projection effects [190, 139, 84, 35]. But, DCF produces highly biased estimates even when it is combined with sophisticated techniques [162], such as the

dispersion function analysis [78, 84, 83], which takes into account the LOS effects. The DCF method produces reasonable estimates only when $f \leq 1/2$ [139, 72, 142, 162, 110], which means that DCF estimates without a fine-tuned f are more than 100% larger than the actual values. The major limitation of the DCF method is that it misses a large fraction of the total energy, which corresponds to the compressible modes.

Then, the following questions arise: Can compressible modes account for the bias of the DCF method? Do kinetic and magnetic energies reach an equipartition when compressible modes are present? Can we add the compressible modes contribution in the estimation of the magnetic field strength from dust polarization? If yes, then do we achieve better estimates of the magnetic field strength? The aforementioned questions can be summarized in one question, which defines the problem that we aim to answer in the current thesis: **How can we estimate the magnetic field strength from dust polarization with high accuracy, such as that deviations do not exceed a factor of two?**

The timing for addressing this problem is excellent. The reason is that the polarization data influx has dramatically increased over the last decade due to the Planck satellite [153] and balloon experiments [53], and will keep increasing over the next decade due to upcoming optical polarization surveys, such as PASIPHAE [176]. In addition, Gaia [58, 59] enabled for the first time the accurate characterization of the 3D shapes of ISM clouds [69, 102, 106], hence of gas volume density, which is essential for magnetic field studies (e.g., Eq. 1.4).

The thesis presents a novel method for estimating the magnetic field strength from dust polarization in compressible media, like the ISM clouds, and is organized as follows: in § 2 we present the numerical simulations employed in this work, in § 3 we present an overview and criticism on the past methods for estimating the magnetic field strength from dust polarization. In § 4 we explore analytically the energetics of compressible fluctuations using a Lagrangian formulation and show that by taking into account the compressible modes we can perfectly describe the properties of numerical simulations. In § 5 we present a new method for estimating the magnetic field strength from dust polarization, while in § 6 we test both the DCF and our proposed method in synthetic data that we produce from numerical simulations. Finally, in § 7 we summarize our results.

Chapter 2

Numerical simulations

The Alfvénic Mach number (\mathcal{M}_A) is the ratio between turbulent velocities over the characteristic propagation speed V_A (Alfvénic speed) of magnetized fluctuations; \mathcal{M}_A is a metric of the magnetic fluctuations' contrast in a fluid ($\mathcal{M}_A \equiv \sqrt{\langle u^2 \rangle} / V_A$). The sonic Mach number (\mathcal{M}_s) is the ratio between turbulent velocities over the sound speed and is a metric of the density contrast in a fluid ($\mathcal{M}_s \equiv \sqrt{\langle u^2 \rangle} / c_s$). ISM turbulence spans a wide range of \mathcal{M}_A and \mathcal{M}_s values. There is overwhelming observational evidence that ISM turbulence is sub-, trans-Alfvénic ($\mathcal{M}_A \lesssim 1$) [135, 55, 152, 145, 154, 38, 179] and highly compressible ($\mathcal{M}_s > 1$) [70, 122, 22, 25, 138, 137, 13]. The numerical simulations employed in this work enable us to test our theoretical arguments and the various magnetic field strength estimation methods to a large number of MHD simulations with a wide range of parameters consistent with observations.

We used data from the following simulations in our tests. "Cho-ENO" [33, 24, 156, 20] simulations from the publicly available CATS¹ database [23]: These are ideal-MHD, isothermal simulations without self-gravity. Turbulence is driven in velocity Fourier space by injecting solenoidal modes only at scales equal to half the size of the simulated cube. Models are characterized by $\mathcal{M}_A = 0.7$ and 2.0, while \mathcal{M}_s ranges between 0.7 and 7.0. [162] have tested the two methods in the $\mathcal{M}_A = 0.7$ simulations of this dataset, but we also included them in our results for completeness. Simulation data are dimensionless and scale-free. A dimensionless sound speed, which is defined as $\tilde{c}_s = \sqrt{\tilde{P}/\tilde{\rho}}$, regulates the units. We assume that the sound speed is 0.91 km/s for every model and follow [79] in order to convert to cgs units. The resolution is 256^3 .

"AREPO" simulations from the CATS database [23]: The simulations setup is presented in detail in [123, 26]. These are isothermal, ideal-MHD simulations run with the AREPO code [166]. Turbulence is driven solenoidally until a quasi-static state was reached with

¹<https://www.mhdturbulence.com/>

$\mathcal{M}_s = 10$ and then self-gravity is switched on. We used the model with $\mathcal{M}_A = 0.35$ at a time step without self-gravity. The resolution of this model is 256^3 .

Simulations from [14, 16]. They solve the ideal-MHD equations without self-gravity and isothermal conditions using a modified version of the FLASH code [56, 46, 51]. Turbulence is driven in Fourier space by injecting the same amount of power between compressible and solenoidal modes at large scales. Sound speed is $c_s = 1$ in every model and gas velocities are expressed in \mathcal{M}_s units. The Alfvénic and sonic Mach numbers cover a wide range of the parameter space, $\mathcal{M}_A = 0.1 - 2.0$ and $\mathcal{M}_s = 0.5 - 20$. Models with $\mathcal{M}_s = 0.5$ have resolution equal to 576^3 , while every other model 512^3 .

Simulations of [94]. These are ideal-MHD, isothermal simulations without self-gravity, which were run with the FLASH code [56]. These simulations are in cgs units with $T = 11$ K, that is sound speed is equal to 0.2 km/s, and $n = 536 \text{ cm}^{-3}$. We used the model with $\mathcal{M}_A = 0.5$ and $\mathcal{M}_s = 7.5$ driven solenoidally. The resolution is 512^3 .

Boundary conditions are periodic in every simulation presented here. In total we used 26 MHD numerical simulations with properties summarized in Table 6.2.

Chapter 3

Overview of past methods

In this chapter we present a brief overview of the two most widely used methods for estimating the magnetic field strength from dust polarization: 1) the classical DCF [42, 27], and 2) the combination of the DCF with the Hildebrand and Houde (HH09) method [78, 84]. We also stress the major caveats of each method.

3.1 Classical DCF method

3.1.1 Foundations of the method

We decompose the total magnetic field into a mean, \vec{B}_0 , and a fluctuating component $\vec{\delta B}$, and consider that \vec{B}_0 is in the POS. The total field is $\vec{B} = \vec{B}_0 + \vec{\delta B}$ with a total magnetic energy density equal to,

$$\frac{B^2}{8\pi} = \frac{1}{8\pi}[B_0^2 + \delta B^2 + 2\vec{\delta B} \cdot \vec{B}_0], \quad (3.1)$$

The last two terms correspond to changes of the magnetic energy, $\delta\epsilon_m$, due to $\vec{\delta B}$ fluctuations. DCF assumed that the ISM plasma conductivity is infinite. This means that the magnetic field is "frozen-in" the gas, hence both gas and field lines oscillate in phase. Turbulent gas motions perturb the field lines and initiate small amplitude fluctuations, $|\vec{\delta B}| \ll |\vec{B}_0|$, *in the form of Alfvén waves* about the mean field. DCF assumed that the kinetic energy of turbulent motions will be equal to the fluctuating magnetic energy density,

$$\frac{1}{2}\rho\langle v_{\perp}^2 \rangle = \frac{\langle \delta B^2 \rangle}{8\pi}, \quad (3.2)$$

where ρ is the gas density and $\langle v_{\perp}^2 \rangle^{1/2}$ the rms velocity. Note that $\vec{B}_0 \cdot \vec{\delta B} = 0$, since Alfvén waves are transverse. We divide both sides by B_0^2 and after rearranging we obtain,

$$B_0 = \sqrt{4\pi\rho} \langle v_{\perp}^2 \rangle^{1/2} \left[\frac{\delta B}{B_0} \right]^{-1}. \quad (3.3)$$

The magnetic field orientation is traced by dust polarization (with a π ambiguity) and the dispersion of the polarization angle distribution, $\delta\theta$, is a metric of $\delta B/B_0$. If the mean field is stronger than the fluctuating component, the field lines will appear approximately straight, hence $\delta\theta$ will be small. If, on the other hand, the fluctuations are relatively large, field lines will be dispersed by turbulent motions and $\delta\theta$ will increase. Thus, DCF assumed $\delta\theta = \delta B/B_0$, yielding,

$$B_0 = \sqrt{\frac{4\pi\rho}{3}} \frac{\langle v_{\perp}^2 \rangle^{1/2}}{\delta\theta}, \quad (3.4)$$

where the factor $1/\sqrt{3}$ was inserted by DCF because they assumed that turbulent motions are isotropic and only one of the three Cartesian velocity components perturbs the field lines. Other authors [139] proposed a different correction factor f . The generalized DCF equation is then,

$$B_0 = f \sqrt{4\pi\rho} \frac{\langle v_{\perp}^2 \rangle^{1/2}}{\delta\theta}. \quad (3.5)$$

The mean magnetic field, B_0 , can be written in velocity units by dividing by $\sqrt{4\pi\rho}$ thus,

$$V_A = f \frac{\langle v_{\perp}^2 \rangle^{1/2}}{\delta\theta}, \quad (3.6)$$

where V_A is the Alfvén speed and is equal to $V_A = B_0/\sqrt{4\pi\rho}$.

3.1.2 Caveats of the method

The DCF approach is based on the assumption of equipartition between kinetic and magnetic energy, which holds for travelling MHD waves. For standing waves the total energy oscillates between magnetic and kinetic forms. Since our observables (polarization angles and spectroscopic data) are instantaneous, equipartition between kinetic and magnetic energies can only happen in standing waves twice in a phase cycle. Standing waves have been produced in MHD simulations [99], and have been identified in the ISM, e.g. in the Musca molecular cloud [179]. We consider only travelling MHD waves.

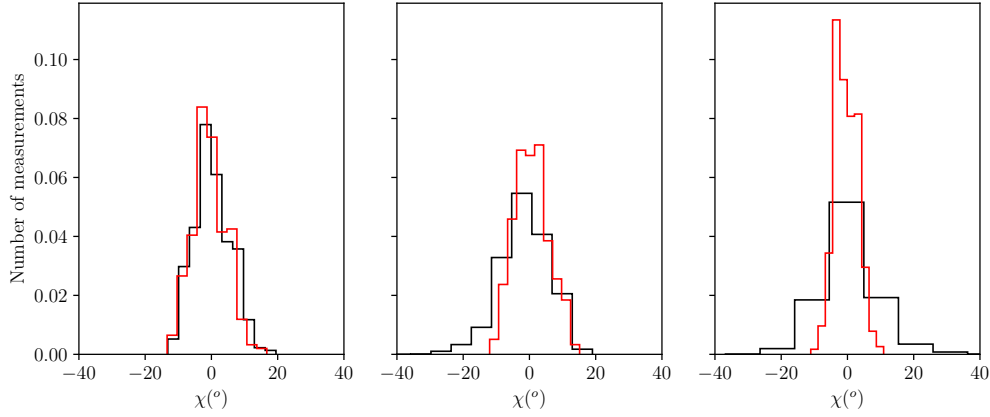


Fig. 3.1 Distribution of the synthetic polarization angles for different simulation models. Black histogram corresponds to observations weighted by density, while the red one without the density weighting. **Left:** Simulation model with $M_S = 0.7$, **Middle:** Simulation model with $M_S = 2.0$, **Right:** Simulation model with $M_S = 7.0$.

Turbulent velocities and compressible modes

The DCF method has been used extensively in atomic and molecular clouds. Turbulent velocities, denoted as δv or σ_v , are measured using spectroscopic data, e.g. HI 21cm line, CO(J=1-0) line, etc. Emission lines are approximated as Gaussians and non-thermal linewidths are usually observed. The non-thermal broadening, $\sigma_{v,turb}$, is attributed to turbulent gas motions,

$$\sigma_{v,turb}^2 = \sigma_{v,tot}^2 - \sigma_{v,thermal}^2, \quad (3.7)$$

where $\sigma_{v,tot}$ is the total observed spread and $\sigma_{v,thermal}$ the thermal broadening.

Turbulent broadening, $\sigma_{v,turb}$, may contain contributions from wave modes other than the Alfvén modes. MHD plasma also supports the propagation of fast and slow modes, which can be excited even if they are not initially in the system [76], due to their coupling with Alfvén modes. These modes could induce extra dispersion in the observed velocities and affect the DCF method, which neglects their contribution.

The ISM is highly compressible [70]. This implies that $\sigma_{v,turb}$ includes velocities from both Alfvén and compressible modes. As a result, $\sigma_{v,turb}$ will always be higher than by Alfvén waves alone, hence B_0 will be overestimated. This makes the mode decomposition necessary in order to apply the DCF method accurately. However, mode decomposition is not trivial in observations.

Projection effects and the polarization angle distribution

Similar to velocities, fast and slow modes can also induce $\delta B/B$ variations [32]. As a result, non-Alfvénic modes will contribute to the observed signal, which will be larger than the Alfvénic. Observationally $\delta B/B_0$ is computed from the spread in the polarization angle distribution, $\delta\theta$. However, $\delta\theta$ may not trace $\delta B/B_0$ accurately. We present two projection effects that are related to this discrepancy. The first one has been demonstrated in previous works, while to our knowledge we are the first to demonstrate the second.

1. Degeneracy with the LOS angle

According to Eq. (3.5), B_0 is inversely proportional to $\delta\theta$. This means that regions with highly disordered magnetic field, i.e. high $\delta\theta$, have a weak field strength. However, high $\delta\theta$ can also be obtained if the magnetic field is mostly parallel to the LOS. In this case, even small perturbations will lead to POS fields that look highly disordered [139, 48, 74]. Thus, there is a degeneracy in $\delta\theta$ between the viewing angle of the magnetic field and the field strength [139, 48]. Houde [82] demonstrated the appropriate geometrical modification of the DCF method in order to account for magnetic fields inclined with respect to the LOS. Such approach, however, requires knowledge of the magnetic field LOS viewing angle.

2. Non-homogeneity effect

It was proposed that the dispersion of the polarization angles, $\delta\theta$, is systematically lower due to line of sight averaging of the magnetic field directions [190, 136]. The reason is that the polarization signal is averaged over N distinct, independent regions (turbulent cells) along the LOS. Thus, due to the central limit theorem, $\delta\theta$ is biased towards lower values, and the magnetic field strength is systematically overestimated [184, 84, 35].

Consider, however, a Cartesian coordinate system with (discrete) independent variables i, j, k . The ij plane is the POS and k is parallel to the LOS. The Stokes parameters are [105, 48],

$$I_{ij} = \sum_{k=1}^L \rho_{ijk}, \quad (3.8)$$

$$Q_{ij} = \sum_{k=1}^L \rho_{ijk} \frac{(B_{ijk}^i)^2 - (B_{ijk}^j)^2}{B_{ijk}^2}, \quad (3.9)$$

$$U_{ij} = \sum_{k=1}^L 2\rho_{ijk} \frac{B_{ijk}^i B_{ijk}^j}{B_{ijk}^2}, \quad (3.10)$$

where L is the LOS dimension of the cloud, ρ_{ijk} the volume density of the gas, B_{ijk}^i, B_{ijk}^j are the i and j component of the magnetic field respectively, and B_{ijk}^2 the square of the total field

strength. The polarization angle is,

$$\chi = 0.5 \arctan(U/Q), \quad (3.11)$$

and the degree of polarization,

$$p = \sqrt{Q^2 + U^2}. \quad (3.12)$$

Since the Stokes parameters are averages with density weights, density variations along the LOS may increase $\delta\theta$. We produce synthetic observations of 3D simulations in order to demonstrate this effect. Here we assume infinite resolution, which corresponds to optical polarization data. However, beam convolution should be taken into account if sub-mm data were to be simulated [72, 184, 48, 84].

We use data from the the "Cho-ENO" (§ 2) numerical simulations. We only use the models with $\mathcal{M}_A = 0.7$ in order to match observations, which indicate that the ISM turbulence is sub/trans-Alfvénic (§ 3.1.2).

We create synthetic polarization maps for every simulation model by computing the Stokes parameters and the polarization angles with equations (3.8) - (3.11). The dispersion of the polarization angles, $\delta\theta$, for each model is shown in Table 6.1 in column 4.

In Fig. 3.1, we show the polarization angle distributions from three different simulation setups with $\mathcal{M}_s = 0.7$ (left panel), $\mathcal{M}_s = 2.0$ (middle panel), $\mathcal{M}_s = 7.0$ (right panel). The black histogram corresponds to the polarization angles computed using Eq. (3.11). The red histograms correspond to the distribution of polarization angles when we integrate by setting $\rho = 1$ everywhere in the box. Histograms are normalized so that the area under each histogram integrates to one. The un-weighted distributions become narrower at larger \mathcal{M}_s , because more independent turbulent cells are created along the LOS. On the other hand, the density-weighted distributions (black) become wider, because more significant overdensities are created due to enhanced compression at larger \mathcal{M}_s . It appears that density fluctuations can induce extra dispersion in the observed polarization angle distribution. This result is consistent with previous works [48], where it is found that the degree of polarization decreases as \mathcal{M}_s increases. Thus, in contrast to previous works [190, 136], we have found that the LOS averaging of the polarization angles can induce extra dispersion, and as a result the magnetic field strength is systematically underestimated.

Different f values

DCF assumed that *turbulent motions are isotropic* and they adopted $f = 1/\sqrt{3}$. If the field strength is weak, turbulent motions will drag the field lines towards random directions and turbulence will be isotropic (super-Alfvénic turbulence). However, there is overwhelming

observational evidence that magnetic fields in the ISM have well-defined directions indicating that turbulence is sub/trans-Alfvénic, and hence turbulent properties are highly anisotropic [128, 160, 77, 168, 65, 66]. CO data revealed that velocity structures in Taurus are highly anisotropic [75]. In the same region other authors [68] reported the existence of highly-anisotropic density structures, which are aligned parallel to the mean field, known as striations. Striations have also been observed in the Polaris Flare [144], and Musca [38, 179] and they are formed due to magnetosonic waves [178] in sub-Alfvénic turbulence [12]. More evidence for ordered magnetic fields in molecular clouds have been reported by several other authors [55, 54, 152, 81, 174]. Stephens et al. [169] explored the magnetic field properties of 52 star forming regions in our Galaxy and concluded that more than 80% of their targets exhibit ordered magnetic fields. The diffuse atomic clouds in our Galaxy are preferentially aligned with the magnetic field [37] implying the importance of the magnetic field in their formation. Planck Collaboration et al. [154] studied a larger sample of molecular clouds in the Gould Belt and concluded that density structures align parallel or perpendicular to the local mean field direction. This is also consistent with sub/trans-Alfvénic turbulence [165]. In addition, Mouschovias et al. [135], using Zeeman data, concluded that turbulence in molecular clouds is slightly sub-Alfvénic as well. All these lines of evidence indicate that ISM turbulence is sub/trans-Alfvénic, and hence anisotropic.

Other f values were proposed when the DCF method was applied in numerical simulations. Ostriker et al. [139] performed MHD numerical simulations of giant molecular clouds. They produced synthetic observations and suggested that the DCF equation with $f = 0.5$ produces accurate measurements for their sub-Alfvénic model. Padoan et al. [142] simulated protostellar cores and tested the DCF equation in three different cores in a super-Alfvénic MHD turbulent box. They varied the position of the observer with respect to the magnetic field direction and found that on average $f = 0.4$. However, note that their values range from 0.29 up to 0.74 (see their Table 1). Heitsch et al. [72] performed 3D MHD simulations of molecular clouds. They found that f lies in the interval 0.3 – 0.5 (Figure 6 [72]) in their three models with strong magnetic fields (sub-Alfvénic turbulence).

In these works f was found to vary significantly, but a value of $f = 0.5$ is widely used [148]. However, no physical connection of f with the turbulent properties of the medium or with specific LOS averaging effects has been demonstrated. Thus, it remains unclear, which value of f is most appropriate for any given real physical cloud. The number of turbulent eddies along the line of sight may be a relevant metric of f and can be estimated with the HH09 method or following other approaches [35, 186].

3.2 HH09 method

3.2.1 Foundations of the method

An alternative way to estimate the $\delta B/B_0$ ratio has been presented by HH09. The method was developed in order to avoid inaccurate estimates of the magnetic field strength induced by sources other than MHD waves, e.g. large-scale bending of the magnetic field due to gravity [62]. HH09 computed the *isotropic dispersion function* of the polarization map as,

$$\langle \cos [\Delta\phi(l)] \rangle = \langle \cos [\Phi(\tilde{x}) - \Phi(\tilde{x} + \tilde{l})] \rangle. \quad (3.13)$$

The quantity $\Phi(x)$ denotes the polarization angle measured in radians, \vec{x} denotes the 2D coordinates in the POS, \vec{l} the spatial separation of two polarization measurements in the POS and brackets averaging over the entire polarization map. The polarization angle differences are constrained in the interval $[0^\circ, 90^\circ]$.

HH09 defined the total magnetic field as $\vec{B}_{tot} = \vec{B}_0 + \vec{B}_t$, where \vec{B}_0 is the mean magnetic field component and \vec{B}_t the turbulent (or random) component. HH09 assumed that the strength of \vec{B}_0 is uniform and \vec{B}_t is induced by gas turbulent motions. They derived the following analytical relation for Eq. (3.13),

$$1 - \langle \cos [\Delta\phi(l)] \rangle \simeq \sqrt{2\pi} \frac{\langle B_t^2 \rangle}{B_0^2} \frac{\delta^3}{(\delta^2 + 2W^2)\Delta'} \times (1 - e^{l^2/2(\delta^2 + 2W^2)}) + ml^2, \quad (3.14)$$

where m is a constant, Δ' is the effective cloud depth and W the beam size. The effective cloud depth is always smaller than the size of the cloud (L), $\Delta' \leq L$, and is defined as the FWHM of the auto-correlation function of the polarized intensity [84]. The validity of this relation is limited to spatial scales $\delta \leq l \leq d$, where δ is the correlation length of \vec{B}_t and d is the upper limit below which \vec{B}_0 remains uniform. This equation is used to estimate the $\langle B_t^2 \rangle^{1/2}/B_0$ term, which is then inserted in the DCF formula as,

$$V_A^{\text{DCF+HH09}} \simeq \sigma_v \left[\frac{\langle B_t^2 \rangle^{1/2}}{B_0} \right]^{-1}. \quad (3.15)$$

The only difference to the classical DCF is that the $\delta B/B_0$ term is obtained from the fit of Eq. (3.14) instead of the dispersion of the polarization angle distribution.

In order to use the method, one has to compute the dispersion function using Eq. (3.13), and then fit the model in the right hand side of Eq. (3.14). The fit has the following three free parameters: $\langle B_t^2 \rangle/B_0^2$, δ and m .

3.2.2 Caveats of the method

Omission of the $\vec{B}_0 \cdot \delta\vec{B}$ term

Hildebrand et al. [78], and Houde et al. [84] assumed that *the correlation of B_t and B_0 is zero, i.e. $\langle \vec{B}_0 \cdot \vec{B}_t \rangle = 0$* , where the averaging is over the full map (see their equation A2). We identify three different regimes, in which $\langle \delta\vec{B} \cdot \vec{B}_0 \rangle = 0$ ¹:

1. Super-Alfvénic turbulence

In the highly super-Alfvénic regime, MHD turbulence behaves like hydro turbulence and $\delta\vec{B}$ is random, i.e. $\langle \delta\vec{B} \rangle = 0$. In this case \vec{B}_0 is much weaker than $\delta\vec{B}$ and the two quantities are statistically independent. Thus,

$$\langle \delta\vec{B} \cdot \vec{B}_0 \rangle = \langle \delta\vec{B} \rangle \cdot \langle \vec{B}_0 \rangle = 0. \quad (3.16)$$

2. Purely Alfvénic (or incompressible) turbulence

For Alfvénic turbulence $\delta\vec{B} \cdot \vec{B}_0 = 0$, because Alfvén waves are transverse and their field fluctuations, $\delta\vec{B}$, are always perpendicular to the mean field \vec{B}_0 [65].

3. Force-free field

If we use the linearized ($|\delta\vec{B}| \ll |\vec{B}_0|$) induction equation,

$$\delta\vec{B} = \vec{\nabla} \times (\vec{\xi} \times \vec{B}_0), \quad (3.17)$$

where $\vec{\xi}$ denotes the gas displacements vector, it can be shown that [167],

$$\langle \delta\vec{B} \cdot \vec{B}_0 \rangle = -\frac{1}{4\pi} \int \vec{\xi} \cdot [(\vec{\nabla} \times \vec{B}_0) \times \vec{B}_0] dV. \quad (3.18)$$

If the field is force-free, $(\vec{\nabla} \times \vec{B}_0) \times \vec{B}_0 = 0$, the above equation implies that $\langle \delta\vec{B} \cdot \vec{B}_0 \rangle = 0$. Although it is occasionally used as an approximation a force-free field naturally decays without causing fluid motions [29].

The cross term, $\langle \delta\vec{B} \cdot \vec{B}_0 \rangle$, is connected with the compressible modes [127], for which $\delta\vec{B} \cdot \vec{B}_0 \neq 0$ [65]. Using standard perturbation theory it can be shown that [18, 19]:

$$\frac{\delta\vec{B} \cdot \vec{B}_0}{4\pi} + \delta P = 0, \quad (3.19)$$

¹Note that we use the more general notation $\delta\vec{B}$ instead of \vec{B}_t since it refers to the fluctuating component of the magnetic field not necessarily in turbulent conditions.

where δP^2 is the gas-pressure perturbations. The equation of state connects gas density and pressure, and hence,

$$\delta \rho \propto \delta \vec{B} \cdot \vec{B}_0 \quad (3.20)$$

where $\delta \rho$ are the gas density perturbations. Eq. (3.20) explicitly shows the coupling between $\delta \rho$ and $\delta \vec{B} \cdot \vec{B}_0$. The omission of the $\delta \vec{B} \cdot \vec{B}_0$ term may lead to significant inaccuracies of the estimate of $\langle B_t^2 \rangle^{1/2}/B_0$ when the HH09 method is applied in sub/trans-Alfvénic and compressible turbulence.

Isotropic turbulence

HH09 assumed that *turbulence is isotropic* and they used a global correlation length, δ . However, this is against observational evidence, which shows highly anisotropic structures and properties (§ 3.1.2). Anisotropic media exhibit different correlation lengths perpendicular and parallel to the mean field. This has been shown in observations [77, 75] and by theoretical works [160, 65, 168, 34, 117]; for a recent review on this topic we refer to Oughton and Matthaeus [140]. This indicates that anisotropic structure functions should be used instead [34, 117]. Chitsazzadeh et al. [31] and Houde et al. [83] refined the HH09 method and considered the anisotropic turbulent properties of sub/trans-Alfvénic turbulence. Our criticism, however, focuses on the original isotropic version of the method, which is still often applied [e.g., 36].

Sparsity of data and the HH09 method

The computation of the dispersion function (Eq. 3.13) for sparsely sampled data introduces a bias. When the dispersion function is computed with optical polarization it is slightly different than the one computed with sub-mm data [164]. The structure function with the optical data systematically overestimates the intercept of the function. As a result, for the case of the sparse sampling, the $\langle B_t^2 \rangle^{1/2}/B_0$ parameter would be biased towards higher values. No solution to this problem has been suggested yet.

²Note that Bhattacharjee and Hameiri [18] and Bhattacharjee et al. [19] use the subscript 1 instead of δ for the perturbed quantities.

Chapter 4

Compressible sub-Alfvénic turbulence energetics

The incompressible turbulence energy equipartition employed by DCF reads: $\rho \langle u^2 \rangle / 2 = \langle \delta B^2 \rangle / 8\pi$. However, direct numerical simulations of sub-Alfvénic and compressible turbulence show that kinetic energy is larger than $\langle \delta B^2 \rangle / 8\pi$ [72, 108], and that their ratio is a function of the strength of the initial magnetic field component (\vec{B}_0), or equally of \mathcal{M}_A [50, 108, 14, 161, 15]. DCF omitted the compressible modes contribution expressed by $\vec{B}_0 \cdot \delta \vec{B}$, which is the dominant potential term when turbulence is sub-Alfvénic, because since $|\vec{B}_0| \gg |\delta \vec{B}|$, the $\vec{B}_0 \cdot \delta \vec{B}$ term is of first order while δB^2 is of second order. The coupling potential is realizable only in compressible turbulence [127, 18, 19, 57], since for incompressible turbulence it is by definition zero [65].

In this section, we present an analytical description of the energy exchange in sub-Alfvénic, compressible turbulence. Using a Lagrangian formulation of elastically interacting cylindrical fluid parcels, we calculate analytically the energetics as a function of \mathcal{M}_A only, and derive explicitly the contribution of $\vec{B}_0 \cdot \delta \vec{B}$ to the energetics. The cylindrical fluid parcel approach allows us to study turbulence dynamics without specifying the properties of individual modes, or modes coupling [114, 61, 117, 32, 185, 61], since the motion of a fluid parcel is the net effect of all modes propagating through it.

Statistical properties of strongly magnetized turbulence are axially symmetric, with \vec{B}_0 being the axis of symmetry [65, 117]. For this reason, we consider a fluid consisting of coherent flux tube segments (or fluid parcels) with coordinates $(r(t), \phi(t), z(t))$. We assume the following initial conditions: 1) uniform temperature; 2) uniform density (ρ); 3) no bulk velocity; 4) uniform static magnetic field ($\vec{B}_0 = B_0 \hat{z}$). We ignore gravity.

We perturb the magnetic field of a fluid parcel (perturbation volume) by $\delta \vec{B}$ such that $|\vec{B}_0| \gg |\delta \vec{B}|$, which applies to sub-Alfvénic turbulence. Magnetic perturbations tend to

redistribute the magnetic flux within a fluid. For ideal-MHD (flux-freezing) conditions, the magnetic flux is preserved. Thus, the perturbed volume's surface \vec{S} would follow the magnetic field lines. The motion of the field lines, and hence of \vec{S} , can be either parallel or perpendicular to \vec{B}_0 ; squeezing and stretching of \vec{S} along \vec{B}_0 leads to parallel motions, $\dot{z} \neq 0$; fluctuations of r lead to perpendicular motions, $\dot{r} \neq 0$; twisting of the perturbed volume leads to rotational motions, $\dot{\phi} \neq 0$. The motion of \vec{S} is coherent, which means that every sub-volume embedded within the perturbation volume would follow the aforementioned movement. This naturally defines the height z and radius r as the coherence lengths of the perturbed volume parallel and perpendicular to \vec{B}_0 respectively. We invoke as a boundary condition the presence of a local environment beyond the coherence length that defines the size of our fluid parcel ("pressure wall").

The flux freezing theorem can be expressed as,

$$\frac{d\vec{B}}{dt} \cdot \vec{S} = -\vec{B} \cdot \frac{d\vec{S}}{dt}. \quad (4.1)$$

The cross sections of the perturbed volume perpendicular and parallel to the initial field \vec{B}_0 are $\vec{S}_\perp = 2\pi r z \hat{r}$, and $\vec{S}_\parallel = \pi r^2 \hat{z}$ respectively, where \hat{r} and \hat{z} are the corresponding unit vectors for each direction. The cross section related to the rotational motion of the perturbed volume is $\vec{S}_\phi = z r \hat{\phi}$. The total magnetic field in cylindrical coordinates can be expressed as $\vec{B} = \delta B_r \hat{r} + \delta B_\phi \hat{\phi} + (B_0 + \delta B_\parallel) \hat{z}$. From Eq. 4.1 we obtain that when $|\vec{B}_0| \gg |\delta \vec{B}|$ magnetic perturbations along \vec{S}_\parallel are associated with a movement of the perturbed volume surface such that,

$$\dot{r}(t) = -\frac{\delta \dot{B}_\parallel(t)}{2B_0 + \delta B_\parallel} r(t) \approx -\frac{\delta \dot{B}_\parallel(t)}{2B_0} r(t), \quad (4.2)$$

along \vec{S}_\perp we find that,

$$\dot{z}(t) \approx -\left(\frac{\delta \dot{B}_r(t)}{\delta B_r(t)} - \frac{\delta \dot{B}_\parallel(t)}{2B_0} \right) z(t), \quad (4.3)$$

while along \vec{S}_ϕ is,

$$\dot{\phi}(t) \approx -\left(\frac{\delta \dot{B}_r(t)}{\delta B_r(t)} - \frac{\delta \dot{B}_\phi(t)}{\delta B_\phi(t)} \right). \quad (4.4)$$

In order to derive the above equation we have used the following relation,

$$\frac{\delta \dot{B}_r(t)}{\delta B_r(t)} \approx -\left(\frac{\dot{r}(t)}{r(t)} + \frac{\dot{z}(t)}{z(t)} \right), \quad (4.5)$$

which can be obtained from Eqs. 4.2, and 4.3.

4.1 Lagrangian formulation

We employ the Lagrangian of the perturbed volume in order to explore its dynamics. We place the reference frame at the center of mass of the perturbed fluid parcel, and hence there is no bulk velocity term in the Lagrangian. Therefore, all the velocity components are solely due to internal motions induced by magnetic perturbations. In addition, we focus on low plasma beta fluids where thermal pressure is subdominant, and hence can be neglected. Then, the local perturbed Lagrangian [8, 100] of the perturbed volume is:

$$\delta\mathcal{L} = \frac{1}{2}\rho u^2 - \frac{B_0\delta B_{\parallel}}{4\pi} - \frac{\delta B^2}{8\pi} \quad (4.6)$$

For a cylinder $\vec{u} = u_r\hat{r} + u_{\phi}\hat{\phi} + u_z\hat{z}$, which is equal to $\vec{u} = \dot{r}\hat{r} + r\dot{\phi}\hat{\phi} + \dot{z}\hat{z}$. Through Eqs. 4.2, 4.3, and 4.4 the Lagrangian can be written as:

$$\begin{aligned} \delta\mathcal{L} = & \frac{1}{2}\rho \frac{\delta\dot{B}_{\parallel}^2}{4B_0^2} L^2 + \frac{1}{2}\rho \frac{\delta\dot{B}_r^2}{\delta B_r^2} L^2 + \frac{1}{2}\rho \frac{\delta\dot{B}_{\phi}^2}{\delta B_{\phi}^2} r^2 - \rho \frac{\delta\dot{B}_r}{\delta B_r} \frac{\delta\dot{B}_{\phi}}{\delta B_{\phi}} r^2 - \\ & - \frac{1}{2}\rho \frac{\delta\dot{B}_r}{\delta B_r} \frac{\delta\dot{B}_{\parallel}}{B_0} z^2 - \frac{\delta B_{\parallel}^2}{8\pi} - \frac{\delta B_r^2}{8\pi} - \frac{\delta B_{\phi}^2}{8\pi} - \frac{B_0\delta B_{\parallel}}{4\pi}, \end{aligned} \quad (4.7)$$

where $L^2 = r^2 + z^2$.

When $\mathcal{M}_A \ll 1$, magnetic tension ($\vec{B} \cdot \nabla \vec{B}/4\pi$) dominates over the magnetic pressure ($\nabla B^2/8\pi$) force due to the presence of the strong background field [147]. The large tension rapidly suppresses transverse oscillations of the perturbed volume, such as kink motions, and induces large restoring torques. This means that the perturbed volume would primarily oscillate as an untwisted body [14], hence motions would be mostly longitudinal. $\dot{\phi}$ has minimum contribution to the dynamics [e.g., 112], for this reason, we neglect twisting ($\dot{\phi}, \delta B_{\phi} \approx 0$).

The parallel and perpendicular velocity components of the cylindrical fluid parcel would be $u_{\parallel} = \dot{z}$, and $u_{\perp} = \dot{r}$. Since $\delta\mathcal{L}$ has no δB_{ϕ} dependence, perpendicular fluctuations would be due to δB_r , hence $\delta B_{\perp} = \delta B_r$. Then, due to Eqs. 4.2, and 4.3, δB_{\parallel} , and δB_{\perp} are generalized coordinates of $\delta\mathcal{L}$ which can be split into parallel (\parallel) and perpendicular (\perp) terms to \vec{B}_0 ; for simplicity we henceforth use the following notation: $z = L_{\parallel}$, and $r = L_{\perp}$,

then $\delta\mathcal{L}$:

$$\delta\mathcal{L} = \overbrace{\left(\frac{1}{2}\rho\frac{\delta B_{\perp}^2}{\delta B_{\perp}^2}L_{\perp}^2 - \frac{\delta B_{\perp}^2}{8\pi}\right)}^{\delta\mathcal{L}_{\perp}} + \overbrace{\left(\frac{1}{2}\rho\frac{\delta B_{\parallel}^2}{B_0^2}[L_{\perp}^2 + L_{\parallel}^2] - \frac{B_0\delta B_{\parallel}}{4\pi} - \frac{\delta B_{\parallel}^2}{8\pi}\right)}^{\delta\mathcal{L}_{\parallel}} - \overbrace{\rho\frac{\delta B_{\perp}}{\delta B_{\perp}}\frac{\delta B_{\parallel}}{B_0}L_{\parallel}^2}^{\delta\mathcal{L}_{\perp}*\delta\mathcal{L}_{\parallel}}. \quad (4.8)$$

Since we have not imposed any physical constraints on the length scales L_{\parallel} and L_{\perp} , the dynamics of the perturbed volume are scale free.

In the sub-Alfvénic regime, Eqs. 4.2, and 4.3 can be simplified, to first order, as,

$$u_{\perp}(t) \equiv \Delta\dot{r}(t) \approx -\frac{\delta\dot{B}_{\parallel}(t)}{2B_0}L_{\perp}(t) \approx -\frac{\delta\dot{B}_{\parallel}(t)}{2B_0}L_{\perp,0}, \quad (4.9)$$

where we have considered that $L_{\perp,0}$, which is the initial dimension of the perturbed volume perpendicular to the ordered magnetic field B_0 , is much larger than its perturbations, and,

$$u_{\parallel}(t) \equiv \Delta\dot{z}(t) = -\left(\frac{\delta\dot{B}_{\perp}(t)}{\delta B_{\perp}(t)} - \frac{\delta\dot{B}_{\parallel}(t)}{2B_0}\right)L_{\parallel}(t) \approx -\frac{\delta\dot{B}_{\perp}(t)}{\delta B_{\perp}(t)}L_{\parallel}(t). \quad (4.10)$$

In the approximate expressions we have employed that $|\vec{B}_0| \gg |\delta\vec{B}|$. In that case parallel and perpendicular motions can be considered independent, hence $\delta\mathcal{L}_{\perp} * \delta\mathcal{L}_{\parallel} \approx 0$ in Eq. 4.8. However, Eq. 4.3 makes the coupling of parallel and perpendicular perturbations inevitable when $|\vec{B}_0| \sim |\delta\vec{B}|$; this coupling would initiate sausage-like oscillations.

The approximate (uncoupled) expressions of Eqs. 4.9, and 4.10 imply that,

$$\delta B_{\parallel}(t) \propto -B_0 \log L_{\perp}(t), \quad (4.11)$$

$$\delta B_{\perp}(t) \propto L_{\parallel}^{-1}(t). \quad (4.12)$$

When L_{\perp} decreases, i.e. the perturbed fluid parcel's surface is compressed and magnetic field lines are dragged with it, then, according to Eq. 4.11, δB_{\parallel} increases, while when the surface is stretched, δB_{\parallel} decreases. Similarly, when L_{\parallel} increases, the side surface is stretched along B_0 , and, according to Eq. 4.12, any δB_{\perp} fluctuations decrease (and vice versa). This behavior is consistent with Bernoulli's principle for magnetized fluids.

The scaling difference in Eqs. 4.11 and 4.12 is due to the Lorentz force by \vec{B}_0 , which affects perpendicular motions, while it has no effect in parallel motions. As a result, it is harder to compress (or rarefy) δB_{\parallel} , which is associated with perpendicular motions, than δB_{\perp} , associated with parallel motions. This explains why the relation in Eq. 4.11 is logarithmic and not linear as in Eq. 4.12.

From Eq. 4.12, we obtain that $L_{\parallel}(t) = C/\delta B_{\perp}(t)$, where C is a constant determined from the initial conditions. With this expression we eliminate L_{\parallel} from the Lagrangian, which up to second order terms, is:

$$\delta \mathcal{L}_{\perp}(\delta B_{\perp}, \delta \dot{B}_{\perp}) \approx \frac{1}{2} \rho C^2 \frac{\delta \dot{B}_{\perp}^2}{\delta B_{\perp}^4} - \frac{\delta B_{\perp}^2}{8\pi}, \quad (4.13)$$

$$\delta \mathcal{L}_{\parallel}(\delta B_{\parallel}, \delta \dot{B}_{\parallel}) \approx \frac{1}{8} \rho \frac{\delta \dot{B}_{\parallel}^2}{B_0^2} L_{\perp,0}^2 - \frac{B_0 \delta B_{\parallel}}{4\pi} - \frac{\delta B_{\parallel}^2}{8\pi}, \quad (4.14)$$

where $L_{\perp}(t=0) = L_{\perp,0}$, and $\delta \mathcal{L}_{\perp} * \delta \mathcal{L}_{\parallel} \approx 0$ since fluctuations are sub-Alfvénic. Below we present the solutions of the Euler-Lagrange equations for $\delta \mathcal{L}_{\parallel}$ and $\delta \mathcal{L}_{\perp}$.

Solutions of $\delta \mathcal{L}_{\parallel}$

Dropping the second-order term, the Euler-Lagrange equation of $\delta \mathcal{L}_{\parallel}$ becomes:

$$\delta \ddot{B}_{\parallel}(t) + \frac{4B_0 V_A^2}{L_{\perp,0}^2} \approx 0, \quad (4.15)$$

where V_A is the Alfvénic speed.

Initially we compress the perturbed volume perpendicularly to \vec{B}_0 , then release it and let the compression propagate (initial conditions: $u_{\perp}(t=0) = 0$, $\delta B_{\parallel}(t=0) = \delta B_{\parallel,\max}$). We derive that,

$$\delta B_{\parallel}(t) \approx \delta B_{\parallel,\max} - \frac{2B_0 V_A^2}{L_{\perp,0}^2} t^2. \quad (4.16)$$

The above solution through Eq. 4.9 yields,

$$u_{\perp}(t) \approx \frac{2V_A^2}{L_{\perp,0}} t. \quad (4.17)$$

Since $u_{\perp}(t) = \Delta \dot{r}$, we obtain that the stretching of the perturbed volume perpendicular to \vec{B}_0 is:

$$L_{\perp}(t) \approx L_{0,\perp} \left(1 + \frac{V_A^2}{L_{0,\perp}^2} t^2 \right). \quad (4.18)$$

As the magnetic field of our perturbed volume decompresses, magnetic energy converts to kinetic, and u_{\perp} increases. However, for sub-Alfvénic flows $u_{\perp} < V_A$, which means that the increase of u_{\perp} cannot continue forever. Therefore, the edge of the fluid parcel will ultimately "bounce" off the rest of the fluid, reversing the direction of u_{\perp} when $\delta B_{\parallel} = -\delta B_{\parallel,\max}$, as we argue below.

When we initially compress the magnetic field of the perturbed volume, then due to Eq. 4.11, L_\perp decreases. This decrease of L_\perp will make the surface of the environment of the perturbed volume to increase by equal amounts. Thus, the initial increase of the magnetic field by $+\delta B_{\parallel,\max}$ of the fluid parcel forces the magnetic field of the environment to decrease by $-\delta B_{\parallel,\max}$ due to flux freezing. If we consider that the fluid is ergodic, then different fluid parcels correspond to different oscillation phases of the target fluid parcel [126, 60]. Therefore, the $-\delta B_{\parallel,\max}$ of the environment, corresponds to the maximum rarefaction of the perturbed volume.

Non-linear effects can break the symmetry between $+\delta B_{\parallel,\max}$ and $-\delta B_{\parallel,\max}$. When $\delta B_{\parallel}(t) < -\delta B_{\parallel,\max}$, then u_\perp starts growing non-linearly until it forms a shock. During the shock formation the perturbed volume interacts with its environment, which acts as a pressure wall and reverses the motion instantaneously. At the post-shock phase, perpendicular motions are reversed and the perturbed volume starts contracting again, but it does not have enough energy to reach $+\delta B_{\parallel,\max}$ since energy has been dissipated by the shock. These "damped" oscillations will continue until all the energy is dissipated [11]. However, if we consider the presence of an external turbulent driving mechanism [113], energy can be maintained in a steady state. This is equivalent to adding kinetic energy to the perturbed volume, during the reversal of the motion, such that the maximum increase of the magnetic field would always be $+\delta B_{\parallel,\max}$.

The perturbed volume spends most of its time in the linear regime, since the non-linear growth is very fast. This means that our approximation only misses a minor fraction of the dynamics. However, the energetics of the perturbed volume are equivalent to that of quasi-static turbulence, since time symmetry is preserved in the approximated Lagrangians (Eq. 4.13, 4.14), hence energy is conserved.

Overall, in the linear approximation δB_{\parallel} would follow ballistic profiles, $\delta B_{\parallel} \propto t^2$, and bounce between $+\delta B_{\parallel,\max}$ and $-\delta B_{\parallel,\max}$ with period $T_b = 4L_{\perp,0}V_A^{-1}\sqrt{\delta B_{\parallel,\max}/2B_0}$. The perturbed volume would spend most of its time in the compressed state, since there the velocity is minimum. On the other hand, the velocity of the fluid parcel is maximum when it is rarefied, and hence the fluid parcel would spend minimum amount of time there. As a result, due to ergodicity, the majority of the fluid parcels at a given time should be compressed ($\delta B_{\parallel} > 0$), which is verified by numerical simulations [15].

Solutions of $\delta\mathcal{L}_\perp$

From the Euler-Lagrange equation of $\delta\mathcal{L}_\perp$ we obtain,

$$\delta\ddot{B}_\perp(t)\delta B_\perp(t) - 2\delta\dot{B}_\perp^2(t) + \frac{\delta B_\perp^6(t)}{4\pi\rho C^2} = 0 \quad (4.19)$$

From Eq. 4.12 we can determine the constant C . If we consider the following initial condition: $\delta B_\perp(0) = \delta B_{\perp,\max}$ and $L_\parallel(0) = L_{\parallel,0}$, then $C = L_{\parallel,0}\delta B_{\perp,\max}$. We divide the Eq. 4.27 with B_0^2 and obtain that,

$$\ddot{g}g - 2\dot{g}^2 + 2g^2 + \frac{\delta B_\perp^2}{4\pi\rho} \frac{\delta B_\perp^2}{\delta B_{\perp,\max}} \frac{1}{L_{\parallel,0}} = 0 \quad (4.20)$$

where $g(t) = \delta B_\perp(t)/B_0$. The units of the above equation are T^{-2} . Thus, we can write the equation in a dimensionless form if we multiply with some characteristic timescale. The Alfvénic speed introduces naturally the following timescale: $T_A = L_{0,\parallel}/V_A$, which corresponds to the crossing time of the fluid parcel along \vec{B}_0 . Then Eq. 4.27 in dimensionless form becomes:

$$\ddot{g}gT_A^2 - 2\dot{g}T_A^2 + g^2 \frac{4\pi\rho L_{\parallel,0}}{B_0^2} \frac{\delta B_\perp^2}{4\pi\rho} \frac{\delta B_\perp^2}{\delta B_{\perp,\max}} \frac{1}{L_{\parallel,0}} = 0, \quad (4.21)$$

which is simplified to,

$$\ddot{g}gT_A^2 - 2\dot{g}T_A^2 + g^4 \frac{\delta B_\perp^2}{\delta B_{\perp,\max}^2} = 0. \quad (4.22)$$

We change variables in the above equation from t to $\tau = t/T_A$ following the chain rule:

$$\dot{g} = \frac{dg}{dt} = \frac{dg}{d\tau} \frac{d\tau}{dt} = \frac{1}{T_A} \frac{dg}{d\tau} = \frac{1}{T_A} g' \quad (4.23)$$

$$\ddot{g} = \frac{d^2g}{dt^2} = \frac{d^2g}{d\tau^2} \left(\frac{d\tau}{dt}\right)^2 + \frac{dg}{d\tau} \frac{d^2\tau}{dt^2} = \frac{1}{T_A} \frac{d^2g}{d\tau^2} = \frac{1}{T_A} g'' \quad (4.24)$$

Then we obtain that:

$$gg'' - 2(g')^2 + g^4 \frac{\delta B_\perp^2}{\delta B_{\perp,\max}^2} = 0, \quad (4.25)$$

The g^4 is a fourth order term and is multiplied with a fraction which is always smaller than one, since $\delta B_\perp(t) \leq \delta B_{\perp,\max}$. Therefore, the g^4 term is negligible compared to the other two terms for every time. Then the above equation can be simplified to:

$$gg'' - 2(g')^2 \approx 0, \quad (4.26)$$

which in dimensional form is,

$$\delta\ddot{B}_\perp(t)\delta B_\perp(t) - 2\delta\dot{B}_\perp^2(t) \approx 0. \quad (4.27)$$

Solutions of the above equation have the following form:

$$\delta B_\perp(t) = -\frac{1}{c_1 t + c_2}, \quad (4.28)$$

where c_1 and c_2 are constants determined from the initial conditions.

The total pressure of the perturbed fluid volume exerted by δB_\perp is transferred to parallel motions (Eq. 4.10) and then $\rho u_{\parallel,\max}^2/2 = \delta B_{\perp,\max}^2/(8\pi)$. For Eq. 4.27 we derive the following solutions:

$$\delta B_\perp(t) \approx \frac{fB_0}{1 \pm fV_A L_{\parallel,0}^{-1}t}, \quad u_\parallel(t) \approx \pm fV_A, \quad (4.29)$$

where $L_\parallel(t=0) = L_{\parallel,0}$, and $f = \delta B_{\perp,\max}/B_0 \ll 1$. Initially we consider that $\delta B_\perp(t=0) = \delta B_{\perp,\max}$, and $u_\parallel(t=0) = u_{\parallel,\max}$. In the above equations signs depend on the initial conditions. The adopted initial conditions lead to positive signs.

Perpendicular motions are suppressed, while parallel motions can free stream due to the absence of any restoring force. If we do not add initial velocity along \vec{B}_0 , then both u_\parallel and δB_\perp would remain static. In general, there is always a coupling of parallel and perpendicular motions, due to Eq. 4.10. Therefore, parallel motions, and hence δB_\perp , will eventually start evolving when $\delta\dot{B}_\parallel \neq 0$. However, in the linear regime that we are focusing this cannot happen, and hence we initiate parallel motions from the initial conditions. From Eq. 4.12 we obtain that the free streaming of our perturbed fluid volume causes L_\parallel to expand as:

$$L_\parallel(t) \approx L_{\parallel,0} \left(1 + \frac{fV_A}{L_{\parallel,0}} t \right) \quad (4.30)$$

However, this expansion will not continue forever. As the target fluid parcel expands its environment along the \vec{B}_0 axis contracts, provided that the fluid has fixed boundaries. Due to the expansion of the target volume, the initial velocity of the environment would be $u_\parallel(t=0) = -u_{\parallel,\max}$, which results to negative sign in the denominator of Eq. 4.29, and hence δB_\perp increases in the environment. On the other hand, δB_\perp in the target volume stops increasing when $t_c = L_{\parallel,0}/(fV_A)$, because δB_\perp in the environment becomes infinite. In sub-Alfvénic flows $|\vec{B}_0| \gg |\delta\vec{B}_\perp|$ and hence this infinity should be treated as an asymptotic behaviour of δB_\perp , which means that there is a physical limit above which δB_\perp cannot grow. After t_c , the motion will be reversed and the environment, along \vec{B}_0 , will start expanding, hence causing

the target volume to contract with δB_\perp growing as $\delta B_\perp(t) \approx fB_0/(2 - fV_A L_{\parallel,0}^{-1}t)$ ¹ until it reaches $\delta B_{\perp,\max}$. If the interaction between the target fluid parcel and its environment were elastic, then the target volume would oscillate periodically, since there would be no energy losses, between $\delta B_{\perp,\max}$ and $\delta B_{\perp,\max}/2$ with period $T_\parallel = 2L_{\parallel,0}/(fV_A)$.

4.2 Energetics

For an ergodic fluid [126, 60], fluctuations of a single fluid parcel resemble the statistical properties of the total volume of the fluid: other fluid parcels oscillate at different phases, but with similar amplitudes. The volume-averaged energetics of the fluid at a given time are equivalent to the time-averaged energetics of a single fluid parcel. We next calculate analytically the time-averaged and compare against the volume-averaged energetics, extracted from MHD numerical simulations.

Kinetic energy

The averaged total kinetic energy of our perturbed volume is,

$$\frac{1}{2}\rho \left(\langle u_\perp^2 \rangle + \langle u_\parallel^2 \rangle \right) \approx \frac{B_0 \delta B_{\parallel,\max}}{6\pi} + \frac{\delta B_{\perp,\max}^2}{8\pi}, \quad (4.31)$$

where brackets denote averaging over a single period. The kinetic energy is dominated, to first order, by u_\perp . Thus, the average Alfvénic Mach number is, to first order,

$$\mathcal{M}_A \equiv \frac{\langle v^2 \rangle^{1/2}}{V_A} \approx \sqrt{\frac{4\delta B_{\parallel,\max}}{3B_0}}. \quad (4.32)$$

Harmonic potential

From Eqs. 4.16, and 4.29 we find that $\langle \delta B_\parallel^2 \rangle = 7\delta B_{\parallel,\max}^2/15$, and $\langle \delta B_\perp^2 \rangle = \delta B_{\perp,\max}^2/2$. The total average harmonic potential energy density is equal to,

$$\frac{\langle \delta B_{\text{tot}}^2 \rangle}{8\pi} \approx \frac{\delta B_{\parallel,\max}^2}{8\pi} \left(\frac{7}{15} + \frac{\zeta^2(\mathcal{M}_A)}{2} \right), \quad (4.33)$$

where $\zeta = \delta B_{\perp,\max}/\delta B_{\parallel,\max}$. Sub-Alfvénic turbulence is anisotropic [160, 77, 141, 65], with the anisotropy between δB_\perp and δB_\parallel depending on \mathcal{M}_A [14]. To account for this property

¹This solution is obtained by considering that the initial conditions in the reversed motion of the fluid parcel are: $\delta B_\perp(0) = \delta B_{\perp,\max}/2$, $u_\parallel(0) = -u_{\parallel,\max}$, and $L_\parallel(0) = 2L_{\parallel,0}$. These values correspond to the solutions of Eqs. 4.29, and 4.30 for $t = t_c$.

in our formalism we consider that ζ , which is a metric of anisotropy between parallel and perpendicular magnetic perturbations, is a function of \mathcal{M}_A . When $\mathcal{M}_A \rightarrow 0$, \vec{B}_0 suppresses any bending of the magnetic field lines with the amplitude of δB_{\parallel} being larger than that of δB_{\perp} [14], hence $\zeta \rightarrow 0$. For $\mathcal{M}_A \rightarrow 1$, fluctuations tend to become more isotropic, and hence $\zeta \rightarrow \sqrt{2}$. These limiting behaviors are consistent with numerical simulations [14, 15].

Coupling potential

According to Eq. 4.31, $\vec{B}_0 \cdot \delta \vec{B}$ contributes to the average kinetic energy of the fluid element as,

$$\frac{B_0 \delta B_{\parallel, \max}}{6\pi} = \sqrt{\frac{15}{7}} \frac{B_0 \langle \delta B_{\parallel}^2 \rangle^{1/2}}{6\pi} \approx \frac{B_0 \langle \delta B_{\parallel}^2 \rangle^{1/2}}{4\pi}. \quad (4.34)$$

This demonstrates that energy stored in the coupling term is in equipartition with the average kinetic energy when turbulence is sub-Alfvénic.

Energetics ratios

We compute the following two energy ratios: 1) kinetic (E_{kinetic} , Eq. 4.31) over coupling term (E_{coupling} , Eq. 4.34), and 2) E_{coupling} over the harmonic potential (E_{harmonic} , Eq. 4.38).

For the first ratio we find that,

$$\frac{E_{\text{kinetic}}}{E_{\text{coupling}}} = \frac{2\pi\rho \langle u_{\text{tot}}^2 \rangle}{B_0 \langle \delta B_{\parallel}^2 \rangle^{1/2}} \approx 1 + \frac{9}{16} \mathcal{M}_A^2 \zeta^2(\mathcal{M}_A). \quad (4.35)$$

When $\mathcal{M}_A \rightarrow 0$ the coupling term is equal to the kinetic energy, while for $\mathcal{M}_A \rightarrow 1$ kinetic energy becomes larger than the coupling term energy. The reason is that the contribution of u_{\parallel} in the total kinetic energy increases at larger \mathcal{M}_A . When $\mathcal{M}_A \rightarrow 1$, $\zeta \approx \sqrt{2}$, so the $E_{\text{kinetic}}/E_{\text{coupling}}$ ratio would scale with \mathcal{M}_A as,

$$\frac{E_{\text{kinetic}}}{E_{\text{coupling}}} \approx 1 + \frac{9}{8} \mathcal{M}_A^2. \quad (4.36)$$

Regarding the $E_{\text{harmonic}}/E_{\text{coupling}}$ ratio we find that,

$$\frac{\langle \delta B_{\text{tot}}^2 \rangle}{2B_0 \langle \delta B_{\parallel}^2 \rangle^{1/2}} = \frac{3}{8} \sqrt{\frac{15}{7}} \mathcal{M}_A^2 \left(\frac{7}{15} + \frac{\zeta^2(\mathcal{M}_A)}{2} \right), \quad (4.37)$$

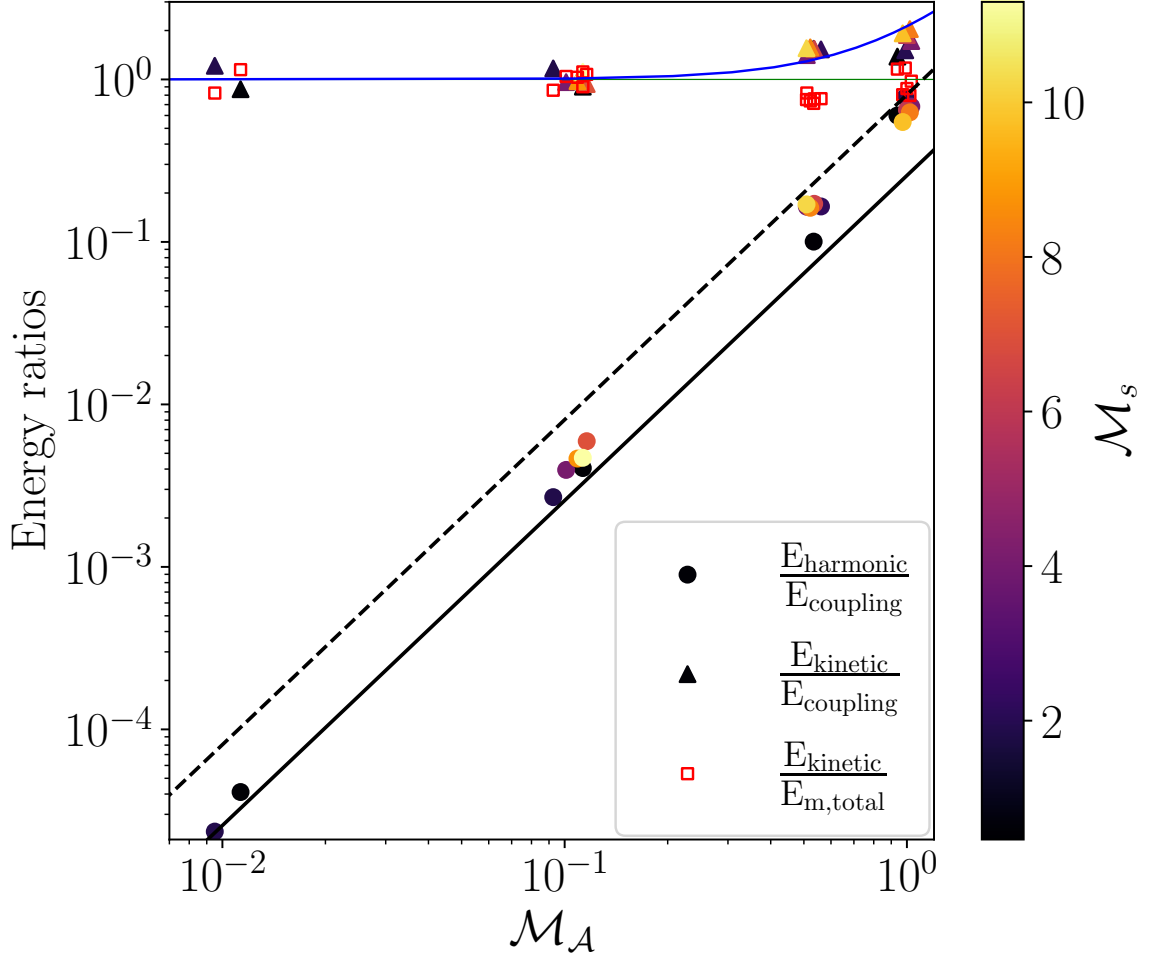


Fig. 4.1 Comparison between analytical and numerical results. Solid and dashed thick black lines correspond to the $E_{\text{harmonic}}/E_{\text{coupling}}$ ratio obtained analytically for $\mathcal{M}_A \rightarrow 0$ ($\zeta = 0$) and $\mathcal{M}_A \rightarrow 1$ ($\zeta = \sqrt{2}$) respectively. Numerical data are shown with colored dots. The blue line corresponds to the analytically-obtained $E_{\text{kinetic}}/E_{\text{coupling}}$ ratio, while colored triangles show the same quantities calculated from numerical data. Red boxes correspond to $E_{\text{kinetic}}/E_{\text{m,total}}$. The thin green line shows energy terms in equipartition. The colorbar shows the sonic Mach number (\mathcal{M}_s) of the simulations.

which, for the limiting cases, becomes,

$$\frac{E_{\text{harmonic}}}{E_{\text{coupling}}} \approx \begin{cases} 0.25 \mathcal{M}_A^2, & \mathcal{M}_A \rightarrow 0 \\ 0.80 \mathcal{M}_A^2, & \mathcal{M}_A \rightarrow 1 \end{cases}. \quad (4.38)$$

4.3 Comparison against numerical simulations

We compare our analytically calculated energy ratios against numerical results extracted from a published table [15]. The numerical data correspond to simulations of ideal, isothermal MHD turbulence, without self-gravity.

In Fig. 4.1 we show the comparison between analytical and numerical results. The black solid and dotted lines show the analytical relation for $E_{\text{harmonic}}/E_{\text{coupling}}$ when $\mathcal{M}_A \rightarrow 0$ and $\mathcal{M}_A \rightarrow 1$ respectively. Colored dots correspond to the numerical ratios. The numerical data behave exactly as predicted by the two limiting cases in Eq. 4.38. For $\mathcal{M}_A > 1$, points start deviating from the inferred limits, as expected, since our $|\vec{B}_0| \gg |\delta\vec{B}|$ approximation breaks down in this case.

The blue solid curve corresponds to the $E_{\text{kinetic}}/E_{\text{coupling}}$ ratio calculated analytically, while triangles correspond to the numerical ratios. Triangles follow the analytical curve remarkably well. Here also the numerical data deviate from our analytical relations when $\mathcal{M}_A > 1$. Accounting for the contribution from both $\vec{B}_0 \cdot \delta\vec{B}$ and δB^2 , the total energy stored ($E_{\text{m,total}} = E_{\text{coupling}} + E_{\text{harmonic}}$) in magnetic fluctuations is very close to equipartition with kinetic energy, as shown by the red boxes.

We conclude that when $\mathcal{M}_A \leq 1$, the total magnetic energy density transferred to kinetic is equal to $(2B_0\sqrt{\langle\delta B_{\parallel}^2\rangle} + \langle\delta B^2\rangle)/8\pi$. This result emphasizes the significance of compressible modes in the energetics of MHD turbulence.

Chapter 5

A new method for estimating the magnetic field strength from dust polarization

Motivated by the existence of compressible modes and the contamination they induce in the DCF method, we propose a generalized method, which takes into account these modes. Similar to DCF, we assume that gas is perfectly attached to the magnetic field and that turbulent motions are completely transferred to magnetic fluctuations. Unlike DCF method, we assume *that all MHD modes are excited, including the compressible modes*. In this case, we do not omit the cross-term in the magnetic energy, which for the general case is $\delta\vec{B} \cdot \vec{B}_0 \neq 0$ (§ 3.2.2). When $|\delta\vec{B}| \ll |\vec{B}_0|$, the dominant potential energy term is (§ 4):

$$\delta\epsilon_m \approx \frac{B_0 \delta B_{\parallel}}{4\pi}. \quad (5.1)$$

We also showed that, to first order, when turbulence is sub-Alfvénic the energy stored in the coupling potential reaches an equipartition with the kinetic energy as (§ 4):

$$\frac{1}{2}\rho \langle v_{\perp}^2 \rangle \approx \frac{B_0 \langle \delta B_{\parallel}^2 \rangle^{1/2}}{4\pi} \quad (5.2)$$

We rearrange the above equation and obtain:

$$B_0 \approx \sqrt{4\pi\rho} \sqrt{\langle u_{\perp}^2 \rangle} \left[2 \frac{\sqrt{\langle \delta B_{\parallel}^2 \rangle}}{B_0} \right]^{-1/2}. \quad (5.3)$$

Since the turbulent-to-ordered magnetic field ratio can be estimated from the dispersion of the polarization angles, we assume that $\delta\theta = \langle \delta B_{\parallel}^2 \rangle^{1/2} / B_0$, and we obtain [161, 162]:

$$B_0 \approx \sqrt{4\pi\rho} \frac{\langle u_{\perp}^2 \rangle^{1/2}}{\sqrt{2\delta\theta}}, \quad (5.4)$$

which can be solved in terms of the Alfvénic speed as,

$$V_A \approx \frac{\langle u_{\perp}^2 \rangle^{1/2}}{\sqrt{2\delta\theta}}. \quad (5.5)$$

We note that the $\langle u_{\perp}^2 \rangle$ that we probe observationally refers to the LOS component of the velocity, since velocity dispersions are obtained from the Doppler broadening of emission lines.

Overall, as in the DCF method, we assume that there is a guiding field about which MHD waves propagate. We also assume that turbulent kinetic energy is equal to the fluctuating magnetic energy, *which is given by $\vec{B}_0 \cdot \delta\vec{B}$, since it is the dominant (first order) term in the magnetic energy.*

Can we trace $\vec{B}_0 \cdot \delta\vec{B}$ with polarization data?

Polarization angle spread is considered to be tracing only fluctuations perpendicular to the mean magnetic field [191] and, as such, is dominated by the Alfvénic modes. However, in the proposed method (Eq. 5.4) it is the $\langle \delta B_{\parallel}^2 \rangle^{1/2} / B_0$ term that is inserted in the energetics, rather than $\langle \delta B_{\perp}^2 \rangle^{1/2} / B_0$. Here we explore if this indeed poses a problem, or whether we can indeed probe parallel magnetic fluctuations from $\delta\theta$.

Consider an ISM cloud permeated initially by an undisturbed and homogeneous magnetic field $\vec{B}_0 = (B_0, 0, 0)$. We perturb \vec{B}_0 with $\delta\vec{B} = (\delta B_x, \delta B_y, \delta B_z)$ and we assume that $\delta\vec{B}$ is random, and hence $\langle \delta\vec{B} \rangle = 0$. The total magnetic field is $\vec{B}_{\text{tot}} = \vec{B}_0 + \delta\vec{B}$,

$$\vec{B}_{\text{tot}} = (B_x, B_y, B_z) = (B_0 \pm \delta B_x, \pm \delta B_y, \pm \delta B_z). \quad (5.6)$$

If the LOS is parallel to the z-axis, then the projected magnetic field morphology of \vec{B}_{tot} as traced by dust polarization will be given by the Stokes parameters [105],

$$I(x, y) = \int \rho dz, \quad (5.7)$$

$$Q(x, y) = \int \rho \frac{B_x^2 - B_y^2}{|B|^2} dz, \quad (5.8)$$

$$U(x, y) = 2 \int \rho \frac{B_x B_y}{|B|^2} dz, \quad (5.9)$$

where $|B|$ denotes the total strength of the field and we have considered perfect grain alignment. The above equations hold when dust grain properties are uniform and temperature is constant throughout the cloud. For simplicity we assume that density is uniform along each LOS and that $|B|^2$ variations along the LOS are negligible (that is that the ρ_0 and B_0^2 terms strongly dominate ρ and $|B|^2$, respectively, and thus the latter can be pulled out of the integrals). From Eq. (5.6) and (5.8), we derived for the Q Stokes parameter,

$$Q(x, y) \approx \rho_0 B_0^{-2} \int \left(B_0^2 \pm 2B_0 \delta B_x + \tilde{\delta} B^2 \right) dz, \quad (5.10)$$

where $\tilde{\delta} B^2 = \delta B_x^2 - \delta B_y^2$. Using Eq. (5.6) and (5.9), the U Stokes parameter can be expressed as,

$$U(x, y) \approx 2\rho_0 B_0^{-2} \int (\pm B_0 \delta B_y \pm \delta B_x \delta B_y) dz. \quad (5.11)$$

If $|\vec{B}_0| \gg |\delta \vec{B}|$, then we can drop the second-order terms, obtaining:

$$Q(x, y) \approx \rho_0 B_0^{-2} \int (B_0^2 \pm 2B_0 \delta B_x) dz, \quad (5.12)$$

$$U(x, y) \approx \rho_0 B_0^{-2} \int 2(\pm B_0 \delta B_y) dz. \quad (5.13)$$

The polarization angle is $\tan 2\theta = U/Q$. In the $|\vec{B}_0| \gg |\delta \vec{B}|$ regime θ is small and $\tan 2\theta \approx 2\theta$. From Eq. (5.12) and (5.13) we obtain,

$$\theta \approx \frac{U}{2Q} \approx \frac{\int (\pm \delta B_y) dz}{\int (B_0 \pm 2\delta B_x) dz}. \quad (5.14)$$

The δB_x term in the denominator of Eq. (5.14) is due to turbulence compressibility. In the limit where perturbations are limited only to Alfvén waves, this term is by definition zero and θ traces the perpendicular fluctuations of the magnetic field fluctuations [191].

The dispersion of polarization angles is $\delta \theta^2 = \langle \theta^2 \rangle_{2D} - \langle \theta \rangle_{2D}^2 = \langle \theta^2 \rangle_{2D}$, since $\langle \theta \rangle_{2D} = 0$, where brackets here denote averaging in the x-y plane. For convenience we adopt the

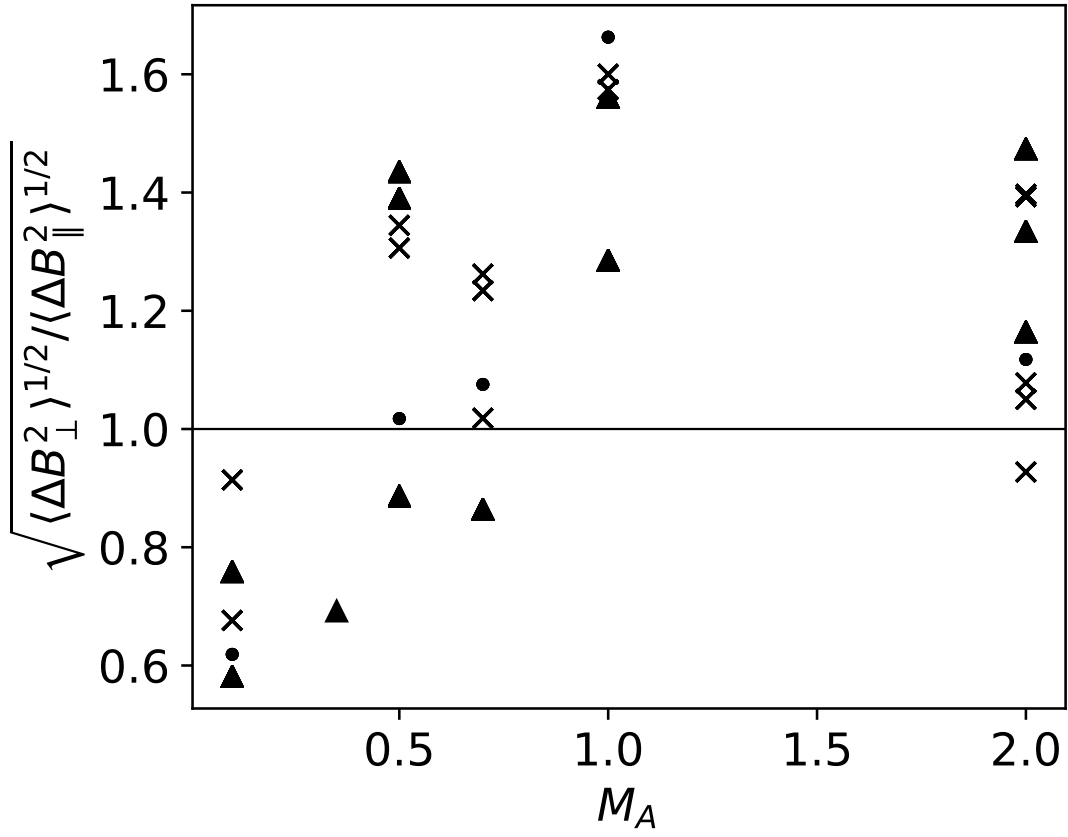


Fig. 5.1 Ratio of perpendicular over parallel LOS averaged magnetic field fluctuations.

following notation:

$$\Delta B_y = \int (\pm \delta B_y) dz, \quad (5.15)$$

$$\Delta B_x = \int (\pm \delta B_x) dz, \quad (5.16)$$

$$\tilde{B}_0 = \int B_0 dz. \quad (5.17)$$

Thus, we obtain,

$$\delta \theta = \left\langle \frac{\Delta B_y^2}{\tilde{B}_0^2 + 4\tilde{B}_0 \Delta B_x + 4\Delta B_x^2} \right\rangle_{2D}^{1/2}. \quad (5.18)$$

Since $|\vec{B}_0| \gg |\delta\vec{B}|$, $4\Delta B_x^2$ is of second order, and hence $\delta\theta$ is simplified to,

$$\delta\theta \approx \left\langle \frac{\Delta B_y^2}{\vec{B}_0^2 + 4\vec{B}_0\Delta B_x} \right\rangle_{2D}^{1/2}. \quad (5.19)$$

The $\vec{B}_0\Delta B_x$ term is due to δB_x and represents the average coupling of \vec{B}_0 with $\delta\vec{B}$.

It is therefore clear that although ΔB_x does contribute to the dispersion of $\delta\theta$, this contribution comes from a first-order term in the denominator of the average in the right hand side of Eq. (5.19). When $|\vec{B}_0| \gg |\delta\vec{B}|$, parallel fluctuations have but a limited contribution in $\delta\theta$ and can be neglected. Thus, to first order, $\delta\theta$ represents perpendicular fluctuations: $\delta\theta \sim \sqrt{\langle\Delta B_y^2\rangle}/\vec{B}_0$.

However, in the proposed method (Eq. 5.4), it is parallel fluctuations that need to be estimated and used in. Only when $\langle\Delta B_y^2\rangle_{2D}/\vec{B}_0 \sim \langle\Delta B_x^2\rangle_{2D}/\vec{B}_0$ would $\delta\theta$ be an adequate metric of parallel fluctuations. The question then becomes: do parallel and perpendicular fluctuations have similar dispersions in compressible turbulence?

The answer is “yes”, as we show in Fig. 5.1, where we have plotted the $\sqrt{\langle\Delta B_\perp^2\rangle_{2D}/\langle\Delta B_\parallel^2\rangle_{2D}}$ ratio, calculated from numerical simulation, as a function of \mathcal{M}_A . We find that in all cases the dispersion of perpendicular fluctuations is comparable to that of parallel fluctuations, with deviations always smaller than a factor of 2. These results are consistent with numerical simulations [14]. We note that in Fig. 5.1 we are displaying the square root of the dispersions of the LOS averages of perpendicular and parallel fluctuations, respectively, since these are the relevant quantities in relating our observable ($\delta\theta$) with the quantity of interest for the proposed method (δB_\parallel).

5.0.1 An analogy with gravity

For incompressible turbulence, one can directly derive the classical DCF equation, Eq. (3.5), with the substitutions $\delta u \rightarrow \sqrt{\langle\delta u^2\rangle}$ and $\delta B \rightarrow \sqrt{\langle\delta B^2\rangle}$, with $\delta\theta$ probing $\sqrt{\langle\delta B^2\rangle}/B_0$. For compressible turbulence $\vec{B}_0 \cdot \delta\vec{B} \neq 0$, since it is connected with the density fluctuations [18, 19]. However, for a periodic signal the number of rarefactions ($\delta\vec{B} \cdot \vec{B}_0 < 0$) is equal to the number of compressions ($\delta\vec{B} \cdot \vec{B}_0 > 0$), and hence $\langle\delta\vec{B} \cdot \vec{B}_0\rangle = 0$ [107, 111, 104]. This on a first reading implies that the DCF method (Eq. 3.5) also applies to compressible turbulence. And yet, the DCF energy equipartition is found to be highly inaccurate when tested in compressible MHD simulations (Fig. 4.1). On the other hand, the energy equipartition that we derived, including the coupling term is significantly more accurate in simulations with compressible turbulence than the DCF (Fig. 4.1). Therefore the argument that the

$\vec{B}_0 \cdot \delta \vec{B}$ term cancels out in the averaged energetics of strongly magnetized and compressible turbulence does not hold. Below we discuss why is so, by doing an analogy with gravity.

Does the $\vec{B}_0 \cdot \delta \vec{B}$ term contribute to the average energetics of compressible turbulence?

The coupling term is by definition zero in the incompressible regime and the averaged total energy (kinetic and magnetic) in the perturbations/waves is,

$$\langle \delta \mathcal{E} \rangle = \frac{1}{2} \rho_0 \langle \delta u^2 \rangle + \frac{\langle \delta B^2 \rangle}{8\pi}. \quad (5.20)$$

This is similar to the energy equation of a harmonic oscillator, where energy fluctuates between kinetic and potential (here magnetic) forms. The physical analogy in incompressible Alfvénic turbulence works well: the magnetic field oscillates harmonically about \vec{B}_0 . The lowest value of the potential energy is achieved at the equilibrium state where $\delta B = 0$. We can thus consider each fluid element as a harmonic oscillator perturbed around $B_0^2/(8\pi)$. According to the ergodic theorem, time averaging is equivalent to spatial averaging (equivalently, we can say that within the cloud there exist all possible oscillation phases); Eq. (5.20) therefore holds - but, in addition, as in the harmonic oscillator, the average values of kinetic and potential energy are equal, $\rho_0 \langle \delta u^2 \rangle / 2 = \langle \delta B^2 \rangle / 8\pi$, whence DCF Eq. (3.5) is obtained.

In compressible and strongly magnetized turbulence the fluctuations are also periodic. The $\vec{B}_0 \cdot \delta \vec{B}$ term, although much higher in absolute value than δB^2 , can be either negative or positive. Therefore $\langle \vec{B}_0 \cdot \delta \vec{B} \rangle = 0$, Eq. (5.20) holds, and it would appear that once again the problem can be reduced to that of a harmonic oscillation. However, in this case the physical analogy is incorrect. There are two reasons for this.

First, unlike a harmonic oscillator, the equilibrium state ($\delta B = 0$) is not the state of lowest potential energy; the maximum rarefaction state ($\delta B = -|\delta B|_{\max}$) is. The cross term, $\vec{B}_0 \cdot \delta \vec{B}$, can be either positive or negative and this means that locally it can either add or remove magnetic flux from the fluid elements. When $\vec{B}_0 \cdot \delta \vec{B} > 0$, then the mean energy density, $B_0^2/(8\pi)$, locally increases by $2|\vec{B}_0 \cdot \delta \vec{B}|/(8\pi)$ due to the compression of the magnetic field lines. On the other hand, in regions where $\vec{B}_0 \cdot \delta \vec{B} < 0$ the mean energy density locally decreases by $-2|\vec{B}_0 \cdot \delta \vec{B}|/(8\pi)$ due to the decompression of the magnetic field lines. In contrast, in a harmonic oscillator (as well as incompressible Alfvénic turbulence), any deviation from the equilibrium position will only increase the potential energy (the magnetic energy, in the case of our fluid elements).

Second, the dependence of the "potential energy" on the perturbation (here of the magnetic field) is linear: $\delta \mathcal{E}_{\text{p,compressible}} \propto \delta B$. In contrast, in a harmonic oscillator the dependence is quadratic: $\delta \mathcal{E}_{\text{p,harmonic}} \propto \delta B^2$. Therefore, neither δu nor δB of a fluid element will behave

harmonically with time. It is thus clear that the harmonic oscillator is not the appropriate physical analog to our problem. Can we substitute it with a more appropriate mechanical analog to guide our intuition?

Indeed we can. Let us consider a shaft with depth $|h|$ below the Earth's surface. We let a basketball fall from height $+h$ above the Earth's surface into the shaft. In classical Newtonian mechanics, the ball will accelerate from a height $+h$ down to the bottom of the hole, $-h$, where it will bounce upward. In the absence of energy losses, the ball executes the reverse motion as if the clock now runs backwards, and the ball will again reach $+h$, before moving once more downwards toward the bottom of the shaft, continuing these oscillations forever. Consider now that we make the choice of taking the zero point of gravitational potential energy to be at the Earth's surface, at its midpoint between its highest value (achieved at $+h$) and lowest value (achieved at $-h$). Now the potential energy mgz is positive above the surface of the Earth ($z > 0$), negative below the surface of the earth ($z < 0$), and its average value over an entire cycle is $\langle mgz \rangle = 0$. At the same time, the kinetic energy is always non-negative, $\langle mv^2/2 \rangle > 0$. It is obvious that in this case, unlike the harmonic oscillator, $\langle mv^2/2 \rangle \neq \langle mgz \rangle$. Equating them would lead to an absurdity. The absurdity is resolved when we compare the absolute maximum potential energy (that is the difference in potential energy between highest and lowest points) with the maximum kinetic energy¹: $mv_{\max}^2/2 = 2mgh$ yields the correct relation between the maximum positive height h , and maximum velocity, v_{\max} .

The analogy with $\vec{B}_0 \cdot \delta \vec{B}$ oscillations works very well if we replace the basketball with a fluid element and the gravitational potential energy with magnetic energy, where δB_{\parallel} now plays a role similar to the height of the bouncing ball. The magnetic field of fluid elements oscillates around \vec{B}_0 , just as the ball height fluctuates around $z = 0$. For this reason $\vec{B}_0 \cdot \delta \vec{B}$ can be positive or negative, that is fluctuations in magnetic energy can be positive or negative if its zero point is defined at $\delta B_{\parallel} = 0$ ($\vec{B} = \vec{B}_0$), just as fluctuations in the gravitational potential energy of the ball can be positive or negative if its zero point is defined at $z = 0$. If oscillations are periodic, we obtain $\langle \vec{B}_0 \cdot \delta \vec{B} \rangle = 0$. Still, we should not be concluding that the coupling term does not contribute to the average energy budget, any more than we should conclude that the potential energy of the bouncing ball does not contribute to its average energy budget.

¹The reader might notice that this is not an exact mechanical equivalent to the case of fluid elements in magnetized compressible turbulence, since in the case of turbulence a second-order term which is always positive is present. To preserve the exact analogy, consider in our mechanical analog that the ball is attached to a spring which is anchored to the bottom of the shaft, with natural length h , and with spring constant k such that $kh^2/2 \ll 2mgh$. The potential energy term is still dominated by mgz and the average kinetic energy will be comparable to $2mgh$; equating it to the average of $kz^2/2$ would still lead to an absurd result, exactly as DCF leads to an incorrect estimate of the ordered magnetic field strength, and an incorrect scaling of $\delta \theta$ with M_A when the $\vec{B}_0 \cdot \delta \vec{B}$ term is dominant in absolute magnitude over δB^2 .

For each fluid element energy oscillates between kinetic and magnetic forms. The total energy density of a fluid element is,

$$E_{tot} = \frac{1}{2}\rho\delta u^2 + \frac{B^2}{8\pi}, \quad (5.21)$$

where $E_{tot} = E_0 + \delta\epsilon$. In the unperturbed case the total energy of each fluid element is $E_0 = B_0^2/(8\pi)$, which is the mean magnetic energy density. When $|\vec{B}_0| \gg |\delta\vec{B}|$, the perturbed energy of each fluid element is,

$$\delta\epsilon \approx \frac{1}{2}\rho\delta u^2 + 2\frac{\vec{B}_0 \cdot \delta\vec{B}}{8\pi}, \quad (5.22)$$

in the fluid rest frame where $u_0 = 0$. The $\delta B^2/8\pi$ term is second order, and hence it was neglected. The $\delta\epsilon$ are energy fluctuations around E_0 and can be negative when $\delta u \rightarrow 0$ and $\vec{B}_0 \cdot \delta\vec{B} < 0$. If we assume undamped oscillations, then the kinetic energy is completely transferred to magnetic and backwards periodically. It is reasonable to assume that kinetic energy fluctuations are dominated by δu^2 fluctuations when the temperature is constant within a cloud implying $\rho \approx \rho_0$.

To make further progress, we should identify the physically correct way to relate the kinetic energy term with the first-order magnetic energy term. As in the case of the bouncing ball, the maximum kinetic energy of the fluid element will be comparable to the absolute maximum magnetic energy (that is the difference between maximum compression and maximum rarefaction):

$$\rho_0\delta u_{\max}^2/2 \sim 2B_0\delta B_{\parallel,\max}/4\pi. \quad (5.23)$$

Of course, neither δu_{\max} nor $\delta B_{\parallel,\max}$ can be probed observationally. The quantities that we do have access to from observations are the spatially-averaged kinetic energy fluctuations, $\langle\delta u^2\rangle$ and magnetic field fluctuations $\sqrt{\langle\delta B^2\rangle}$ (Sect. 5), which, by virtue of the ergodic theorem, correspond to the time-averaged fluctuations over an entire period of the evolution. What we need then is a way to relate δu_{\max} to $\langle\delta u^2\rangle$, and $\sqrt{\langle\delta B^2\rangle}$ to $\delta B_{\parallel,\max}$.

In the case of the bouncing ball, the time evolution of its velocity v and height z are straightforward to obtain, so we can in fact calculate these relations between v_{\max}^2 and $\langle\delta v^2\rangle$, and between z_{\max} and $\sqrt{\langle z^2\rangle}$. Before we do so, however, and use them in the problem at hand, we should investigate how far we can take the analogy between bouncing ball and fluid element in compressible, strongly magnetized turbulence. Would the time behavior of the fluid element have in fact the same functional form as in the bouncing ball?

The answer is "yes", provided that we can write a formally equivalent Lagrangian for the two systems, and show that the boundary conditions of the problem are similar. If we

take the magnetic field perturbation parallel to \vec{B}_0 , δB_{\parallel} , to be a generalized coordinate for the problem, then the generalized velocity would be $\delta \dot{B}_{\parallel}$, which, by virtue of flux freezing, is proportional to δu_{\perp} (the velocity of the fluid element perpendicular to the magnetic field)². In the bouncing ball case, we have a potential energy term that is proportional to z , and a kinetic energy term that is proportional to \dot{z}^2 . Similarly, for the fluid element responsible for a magnetic field compression or rarefaction, we have a potential energy term that is proportional to δB_{\parallel} , and a kinetic energy term that is proportional to $\delta u_{\perp}^2 \propto \delta \dot{B}_{\parallel}^2$. The Lagrangians of the two problems are thus formally equivalent. The boundary conditions of the problem are also similar: the presence of the bulk medium and its large-scale magnetic field acts as the “ground”, forcing the fluid element with increasing velocity undergoing a rarefaction to reverse course back toward increasing magnetic field with velocity decreasing in magnitude. As a result, the time evolution profiles of δB_{\parallel} and $\delta \dot{B}_{\parallel}$ will be similar to those of z and v , respectively, in the bouncing ball problem.

For the bouncing ball, over one period of the motion $\langle v^2 \rangle = v_{\max}^2/3$ and $\langle z^2 \rangle = 7h^2/15$. Therefore, by eliminating v_{\max}^2 in favor of $\langle v^2 \rangle$, and h in favor of $\sqrt{\langle z^2 \rangle}$, the relation between maximum kinetic and potential energies, $mv_{\max}^2/2 = 2mgh$, can be rewritten as,

$$\frac{1}{2}m\langle v^2 \rangle = \frac{2}{3}\sqrt{\frac{15}{7}}mg\sqrt{\langle z^2 \rangle} \approx mg\sqrt{\langle z^2 \rangle}, \quad (5.24)$$

which is equivalent to the energy equipartition that we derived analytically for sub-Alfvénic and compressible turbulence (§ 4).

5.0.2 Comments on the assumptions and approximations of the proposed method

Here we discuss some assumptions entering our proposed method which can limit its accuracy. Firstly, we assumed that oscillations are undamped in compressible turbulence, but in reality shocks lead to significant energy loss and nonideal effects (e.g., ambipolar diffusion) can induce significant loss of magnetic flux from the cloud. Even in ideal-MHD simulations there is significant energy dissipation due to the presence of shocks and numerical diffusion. In these cases, equipartition between the root-mean-square (rms) kinetic and magnetic energy is not guaranteed. In nature, equipartition can hold when there is a constant energy source at large scales injecting energy to the cloud. In numerical simulations this is achieved with the so called forcing, applied in most cases. Secondly, we assumed that magnetic pressure dominates over gas pressure. This is a reasonable approximation for clouds with $\mathcal{M}_A < 1$ and

²The result can be obtained, for example by differentiation with respect to time of Alfvén’s theorem.

$\mathcal{M}_s > 1$, but when $\vec{B}_0 \cdot \delta\vec{B} < 0$ the magnetic pressure may locally become comparable to the gas pressure (especially in cases when $\vec{B}_0 \cdot \delta\vec{B}$ is close to its negative minimum). However, an oscillator spends only a limited amount of time at its negative minimum, which through ergodicity means that gas pressure will be important only for a small volume fraction of the cloud. Thirdly, to arrive to Eq. (5.2) we assumed that gas density fluctuations are much smaller than u^2 , and hence that density is approximately constant in the Lagrangian, $\rho \approx \rho_0$ (Eq. 4.8). Thus, Eq. (5.2) omits any contribution from density fluctuations in the kinetic energy, $\langle \delta\rho u^2 \rangle / 2$.

Chapter 6

Numerical assessment of interstellar magnetic field strength estimation methods

6.0.1 How good are the energy equipartition assumptions?

In order to assess the validity of Eqs. (3.2) and (5.2), we tested them in numerical simulations. We computed the kinetic energy term ($\rho_0 \langle u_{\perp}^2 \rangle / 2$) and compared it against the two different magnetic energy terms.

In Fig. 6.1 we show in the vertical axis the ratio of kinetic over magnetic energy, with both terms calculated from Eq. (3.2) (DCF). In the horizontal axis, we show the ratio of kinetic over magnetic energy, with both terms calculated from the proposed equation (Eq. 5.2, henceforth ST). Different color points correspond to simulations with different \mathcal{M}_A , while different shapes correspond to simulations with different \mathcal{M}_s . Subsonic ($\mathcal{M}_s < 1$) simulation results are shown with dots, supersonic models with $1 < \mathcal{M}_s \leq 4$ are shown with an "x" and $\mathcal{M}_s > 4$ models are shown with triangles. The vertical line indicates exact equipartition à la ST and the horizontal line exact equipartition à la DCF. Diagonal lines separate the regions where each method outperforms the other. Green-shaded regions are closer to the horizontal than the vertical line; there, it is the quadratic term in magnetic energy that dominates and is better comparable to the kinetic energy. White-shaded regions are closer to the vertical line; there, it is the coupling term in the magnetic energy that dominates, and it is that term that is closer to the kinetic energy.

Our results suggest that Eq. (3.2) (DCF) is highly inaccurate (by factors of several to 100) in sub-Alfvénic simulations, performs comparably to Eq. (5.2) (ST) in trans-Alfvénic simulations, and clearly outperforms Eq. (5.2) (ST) only in trans-, super- Alfvénic turbulence

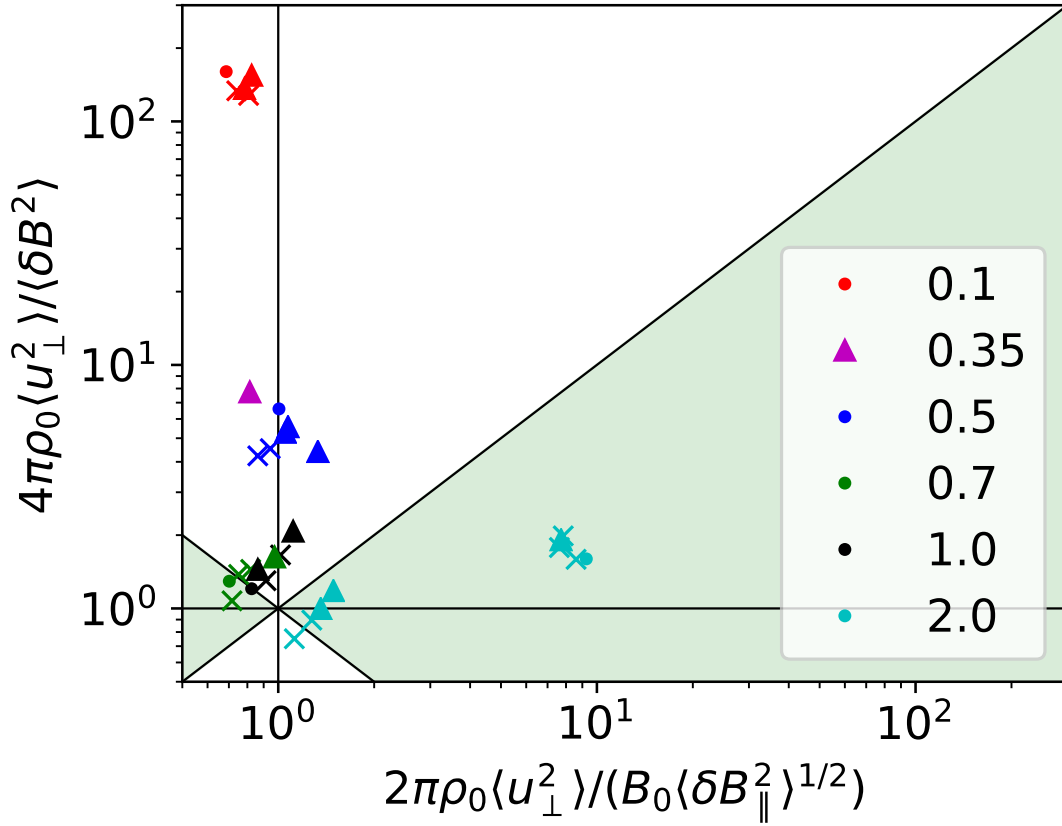


Fig. 6.1 Relative ratio of kinetic over magnetic energy density using Eq. (3.2) (vertical axis) and Eq. (5.2) (horizontal axis). Colors correspond to different \mathcal{M}_A as shown in the legend. Dots correspond to simulations with $\mathcal{M}_s < 1$, "x" to $1 < \mathcal{M}_s \leq 4$ and triangles to $\mathcal{M}_s > 4$.

simulations driven solenoidally (Fig. 6.2, and § 6.0.2). This shows the weakness of the incompressible approximation to accurately describe the energetics of sub-Alfvénic turbulence and indicates that the DCF method is precarious to use when the \mathcal{M}_A of a cloud is unknown. On the other hand, ST is fairly accurate (better than factor of 2) in the entire sub-, trans- Alfvénic regime, even for high \mathcal{M}_s cases. Overall, the coupling term dominates in the energetics over the δB^2 term when $\mathcal{M}_A < 1$ and cannot be ignored.

6.0.2 How does the forcing affect the energetics?

Turbulence in MHD simulations is driven in order to achieve the desired \mathcal{M}_s . Driving is implemented by injecting compressible or incompressible or a mixture of modes in the cloud through a stochastic process in Fourier space. This process is supposed to mimic the driving

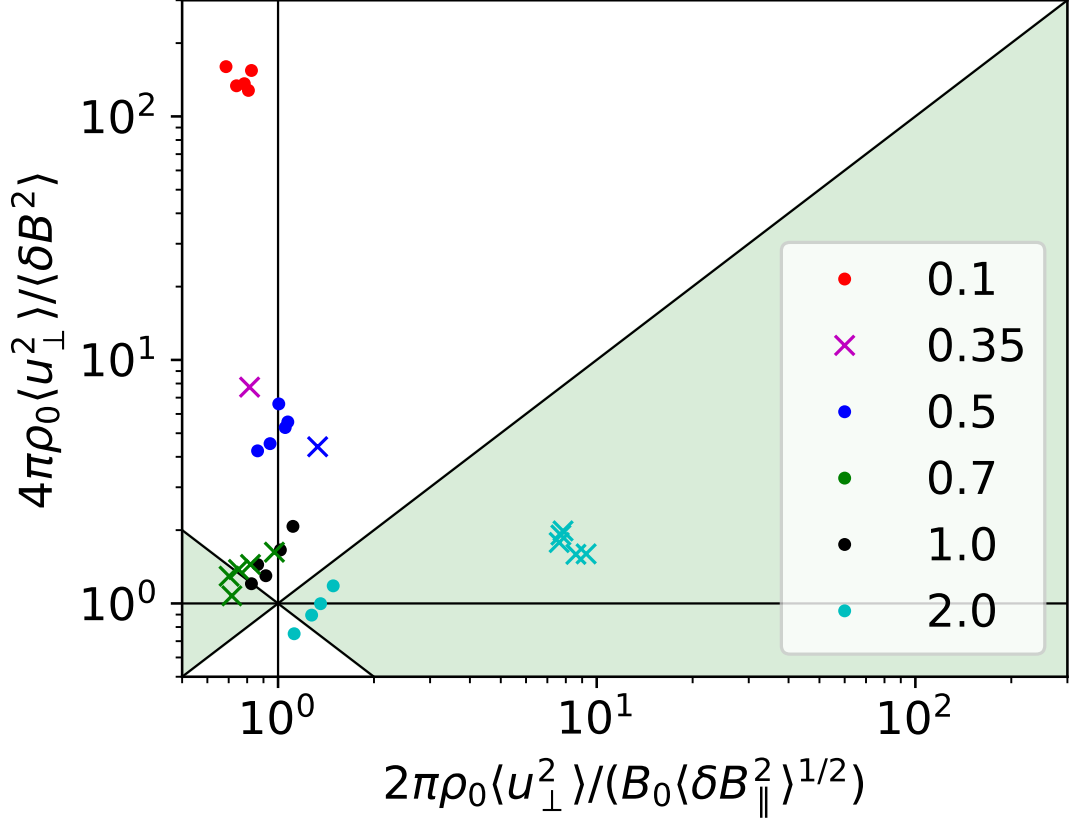


Fig. 6.2 Same as in Fig. 6.1, but the dots correspond to models driven with a mixture of compressible and solenoidal modes and "x" denotes models driven solenoidally.

mechanisms found in nature. We explored if there is any dependence of the results shown in Fig. 6.1 on the forcing mechanism.

In Fig. 6.2 we show the same data as in Fig. 6.1, but here dots correspond to models driven with a mixture of compressible and incompressible modes, and "x" represents solenoidally driven simulations. The driving mechanism of each simulation is shown in the second column of Table 6.2. The majority of simulations used in the current work were driven with an equal mixture of modes, but there are also a few driven solenoidally. Overall, our results in Fig. 6.2 are weakly affected by the forcing mechanism in the sub-Alfvénic simulations.

We compared the effect of forcing at models with $\mathcal{M}_A = 0.5$ and $\mathcal{M}_A = 2.0$, since we have an overlap of both solenoidally and mixed driven simulations. Blue points correspond to models with $\mathcal{M}_A = 0.5$. The solenoidally driven model (shown with the blue "x") has the largest kinetic over $B_0\langle \delta B_\parallel^2 \rangle^{1/2}$ ratio. The reason is that forcing injects only incompressible modes in the cloud which are only traced by δB^2 . On the other hand, when mixed forcing

Table 6.1 3D MHD simulations

M_S	V_A^{true}	σ_v	$\delta\theta$	$V_A^{DCF}(f=1)$	$\langle B_t^2 \rangle^{0.5}/B_0$	$V_A^{DCF+HH09}$	V_A^{new}
0.7	0.91	0.46	0.097	4.7	0.11	4.1	1.0
1.2	1.60	0.58	0.116	5.0	0.13	4.5	1.2
2.0	2.87	1.36	0.128	10.6	0.19	7.1	2.7
4.0	5.09	1.89	0.132	14.3	0.24	7.9	3.7
7.0	9.10	3.98	0.146	27.3	0.29	13.7	7.4

The following columns are measured in units of km s^{-1} : V_A^{true} , σ_v , V_A^{DCF} , $V_A^{DCF+HH09}$ and V_A^{new} . The quantities $\delta\theta$ and $\sqrt{\langle B_t^2 \rangle}/B_0$ are measured in radians.

is used the kinetic energy is equally shared among $B_0\langle\delta B_{\parallel}^2\rangle^{1/2}$ and δB^2 . For this reason, the blue "x" point is shifted toward larger and smaller values in the horizontal, and vertical axis respectively compared to the blue dots. However, the difference between the forcing mechanisms does not create significant deviations between these models. In sub-Alfvénic turbulence \vec{B}_0 is much stronger than the forced perturbations and determines how energy is transferred among the modes.

The effect of forcing in super-Alfvénic simulations is more prominent. We compared the models with $\mathcal{M}_A = 2.0$ (shown with cyan) and mixed forcing (denoted by dots) with the solenoidally driven models (denoted by \times). Models with mixed forcing are clustered in the bottom left corner of Fig. 6.2, while models with solenoidal forcing in the right bottom corner. The reason is that solenoidal modes are not represented by δB_x , and hence all the injected kinetic energy goes to $\delta B^2/(8\pi)$. On the other hand, when mixed forcing is applied the injected energy is shared. In super-Alfvénic turbulence $|\vec{B}_0| < |\delta\vec{B}|$, and hence the dynamics of the cloud are determined by $\delta\vec{B}$, instead of \vec{B}_0 . In these cases the mode of the forced fluctuations determines the cloud dynamics. Thus, there is a large separation between the solenoidal and mixed driven simulations with $\mathcal{M}_A = 2.0$ in Fig. 6.2. Magnetic field lines are highly curved in the solenoidally driven simulation, and hence $\delta B^2/(8\pi) \gg B_0\langle\delta B_{\parallel}^2\rangle^{1/2}$. On the other hand, in mixed driven simulations $\delta B^2/(8\pi) \approx 2B_0\langle\delta B_{\parallel}^2\rangle^{1/2}$. This is in striking contrast with the sub-Alfvénic turbulence where fluctuations evolve independently of the forcing mechanism and fluctuations are dictated by \vec{B}_0 and not by $\delta\vec{B}$.

6.0.3 Testing HH09 with 3D simulations

We apply the HH09 method to the polarization angle maps, $\chi(x, y)$, we created in Section 3.1.2 as suggested by [84]. We compute the dispersion function (Eq. 3.13) from our synthetic data, black dots in Fig. 6.3. We then fit to the black dots the right hand side of

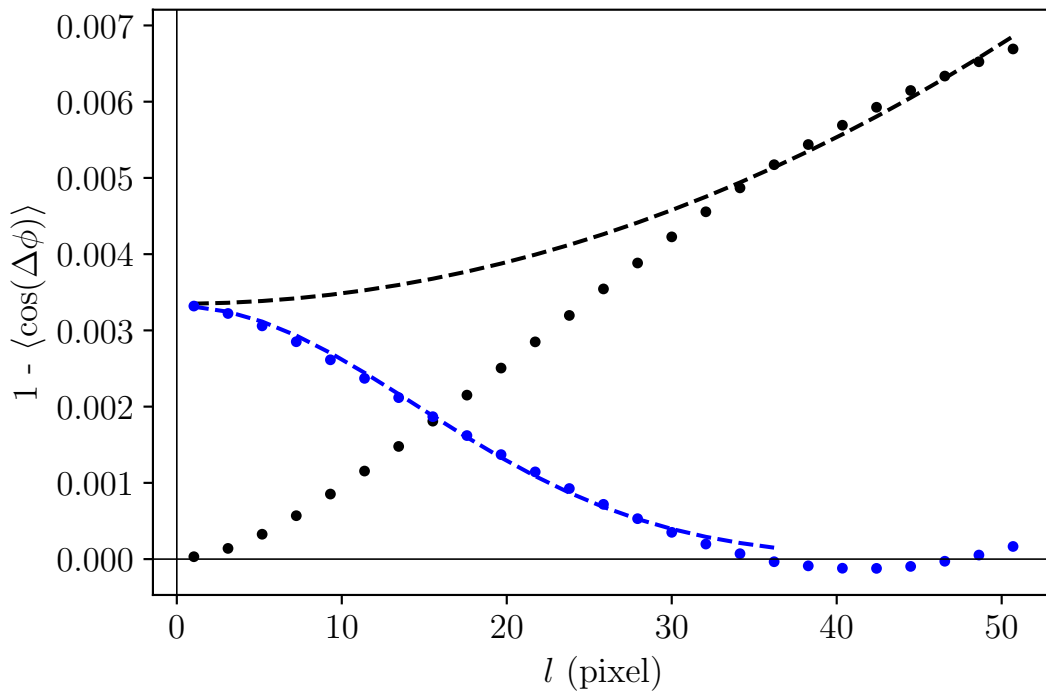


Fig. 6.3 Black dots correspond to the dispersion function computed using Eq. (3.13) for the $M_s = 0.7$ model. The model fit at large scales is shown with the black broken curve. Blue points mark the dispersion function subtracted with the black broken line and the blue line shows the fit of Eq. (6.1).

Eq. (3.14), without including the exponential term. This fit, shown with the black broken curve, is performed at larger scales, i.e $l > 20$ pixels. The black broken curve is then subtracted from the black points and the result, shown with the blue dots, corresponds to the turbulent auto-correlation function, i.e. to the second term of Eq. (3.14),

$$b^2(l) = \sqrt{2\pi} \frac{\langle B_t^2 \rangle}{B_0^2} \frac{\delta^3}{(\delta^2 + 2W^2)\Delta'} e^{l^2/2(\delta^2 + 2W^2)}. \quad (6.1)$$

We fit this term to the blue points and we derive the turbulent correlation length (blue broken curve in Fig. 6.3), δ . The turbulent-to-ordered magnetic field ratio is ,

$$\frac{\langle B_t^2 \rangle^{1/2}}{B_0} = b(0)\sqrt{N}, \quad (6.2)$$

where N is the number of turbulent cells along the line of sight and is defined as,

$$N = \frac{\delta^2 + 2W^2}{\sqrt{2\pi}\delta^3} \Delta', \quad (6.3)$$

where Δ' is computed as in [84]. Like in optical polarization data beam resolution is infinite in our synthetic observations, and hence $W = 0$ [55, 145]. In Appendix A we show the dispersion function plots for the rest of the models and in Table A.1 the best fit parameters are given. The turbulent-to-ordered ratio obtained for the different simulation models is shown in column $\langle B_t^2 \rangle^{1/2}/B_0$, in Table 6.1.

To obtain an estimate of $\delta u \sim \sqrt{\langle u_\perp^2 \rangle} \sim \sigma_{turb}$, we created spectroscopic data in the form of a position-position-velocity (PPV) cube [121]. We used the following equation,

$$I_\nu(x, y, \nu) = \sum_{LOS} \frac{\rho(x, y, z)}{\sqrt{2\pi}\sigma(x, y, z)} \exp \left[-\frac{(v_{los}(x, y, z) - \nu)^2}{2\sigma(x, y, z)^2} \right], \quad (6.4)$$

where $v_{los}(x, y, z)$ is the LOS velocity component and ν is the central velocity of each velocity channel. This equation assumes optically thin emission. In Eq. (6.4), $\sigma(x, y, z)$ is due to thermal broadening and is equal to $\sqrt{k_B T/m}$, where k_B is the Boltzmann constant. We then fitted Gaussian profiles to every I_ν spectrum and derived an "observed" line spread (σ_{obs}) as a free parameter of the fitting. We computed the turbulent velocity by subtracting in quadrature the thermal broadening,

$$\sigma_{turb} = \sqrt{\sigma_{obs}^2 - \frac{k_B T}{m}}. \quad (6.5)$$

The estimated Alfvén speed when the HH09 method is combined with DCF is shown in the same Table in the $V_A^{\text{DCF+HH09}}$ column. The DCF+HH09 estimates are significantly improved compared to the classical DCF values (column: $V_A^{\text{DCF}}(f=1)$) although the overestimation from the true Alfvén speed (V_A^{true}) is still prominent. We note, however, that if we consider that the effective cloud depth is equal to the cloud size, i.e. $\Delta' = 256$ pixels, the HH09 method produces more accurate estimates of the field strength for the models with $\mathcal{M}_s = 4.0$ and 7.0 .

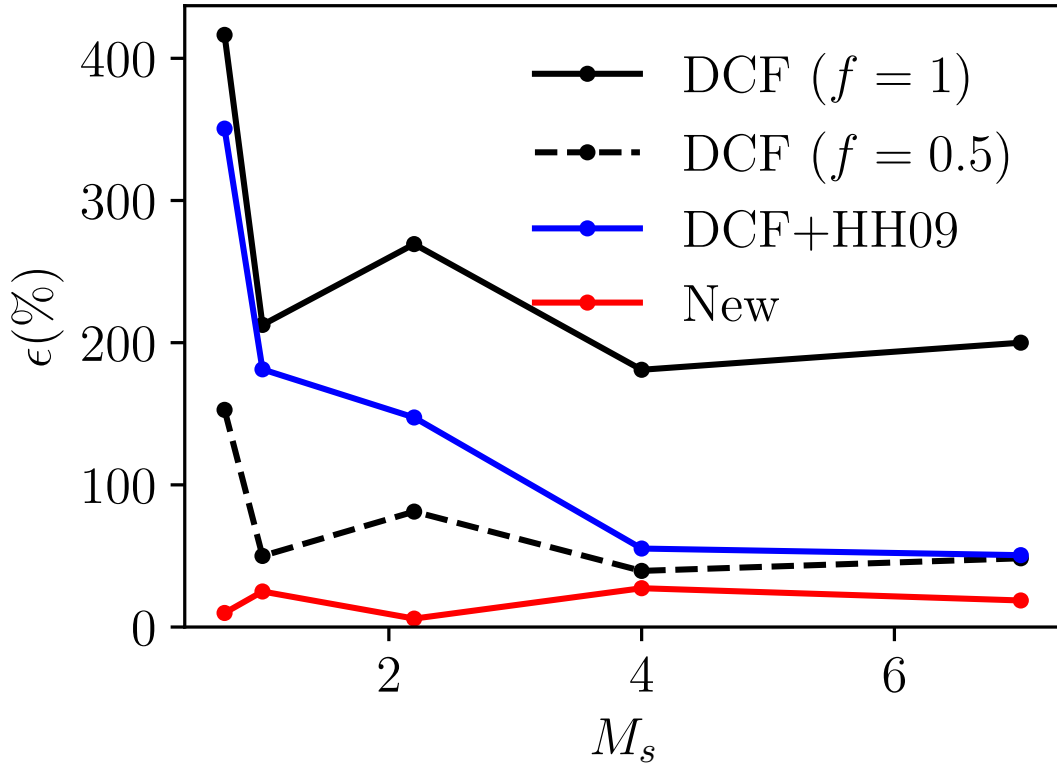


Fig. 6.4 Absolute relative deviation ($|\epsilon|$) of each method estimate for the different simulation models. All the models have $\mathcal{M}_A = 0.7$.

For comparison we also apply the proposed method to the same numerical data. We use the $\delta\theta$ and σ_v from Table 6.1. In the same Table we show in the V_A^{new} column the value computed using the proposed equation (5.4). It is evident that our model produces acceptably accurate estimates of the true V_A in all models.

We assess the accuracy of each method using the relative deviation of the estimated V_A from the true one is,

$$\varepsilon(\%) = 100 \frac{V_A^{true} - V_A^{est}}{V_A^{true}}. \quad (6.6)$$

where V_A^{true} is the true V_A and V_A^{est} is the estimated value from the various methods. In Fig. 6.4 we show $\varepsilon(\%)$ for all models. The black points correspond to DCF (Eq. 3.6) with $f = 1$ (solid line) and $f = 0.5$ (dotted line), blue to DCF+HH09 (Eq. 3.15), and red to the new proposed method (Eq. 5.5). DCF systematically overestimates the true value and even with the previously reported two-fold reduction, i.e. $f = 0.5$, the deviations are still significant. DCF+ HH09 produces very large estimates in the models with low \mathcal{M}_s , while at higher \mathcal{M}_s the method is more accurate. The proposed method produces very accurate values for the field strength independently of \mathcal{M}_s without using any external correction.

6.1 Testing scalings with numerical simulations

The major difference between DCF and our proposed method is the dependence of the magnetic field strength on $\delta\theta$. In DCF, B_0 scales as $\delta\theta^{-1}$ (Eq. 3.5), while in the proposed method it scales as $\sim \delta\theta^{-1/2}$ (Eq. 5.4). One can divide both equations with $\sqrt{4\pi\rho}$ and obtain the magnetic field strength in velocity units (the Alfvénic speed, V_A). The scaling relations of DCF and our new method expressed in terms of V_A are $V_A \sim \delta\theta^{-1}$, and $V_A \sim \delta\theta^{-1/2}$, respectively. The Alfvénic speed is $V_A = c_s \mathcal{M}_s / \mathcal{M}_A$, where c_s is the sound speed. Using the above equation with the corresponding $\delta\theta$ scaling dependence of the two methods we obtain:

$$\delta\theta \propto \begin{cases} \mathcal{M}_A, & \text{DCF} \\ \mathcal{M}_A^2, & \text{proposed method} \end{cases}. \quad (6.7)$$

This is the key difference between the two methods, and it is based on the different scaling relation of \mathcal{M}_A with the magnetic fluctuations in the incompressible [65] and compressible turbulence [49, 14]. We tested the two scalings in synthetic polarization data. We computed synthetic Q and U Stokes parameters (Eq. 5.8 and 5.9 in § 5) and the polarization angles as $\theta = 0.5 \arctan Q/U$. Then, we computed the dispersion of the θ angles, $\delta\theta$. All $\delta\theta$ values are shown in Table 6.2.

In Fig. 6.5 we show $\delta\theta$ as a function of \mathcal{M}_A (we do not show the solenoidally driven models with $\mathcal{M}_A = 2.0$ since their $\delta\theta$ is not representative of the actual fluctuating-to-ordered magnetic field ratio, § 6.2.2). The blue line corresponds to the scaling of the proposed method, and the magenta line to the DCF scaling. Both lines are normalized so that they pass through the simulated data for $\mathcal{M}_A = 1.0$. The scaling of our new method shows a remarkable

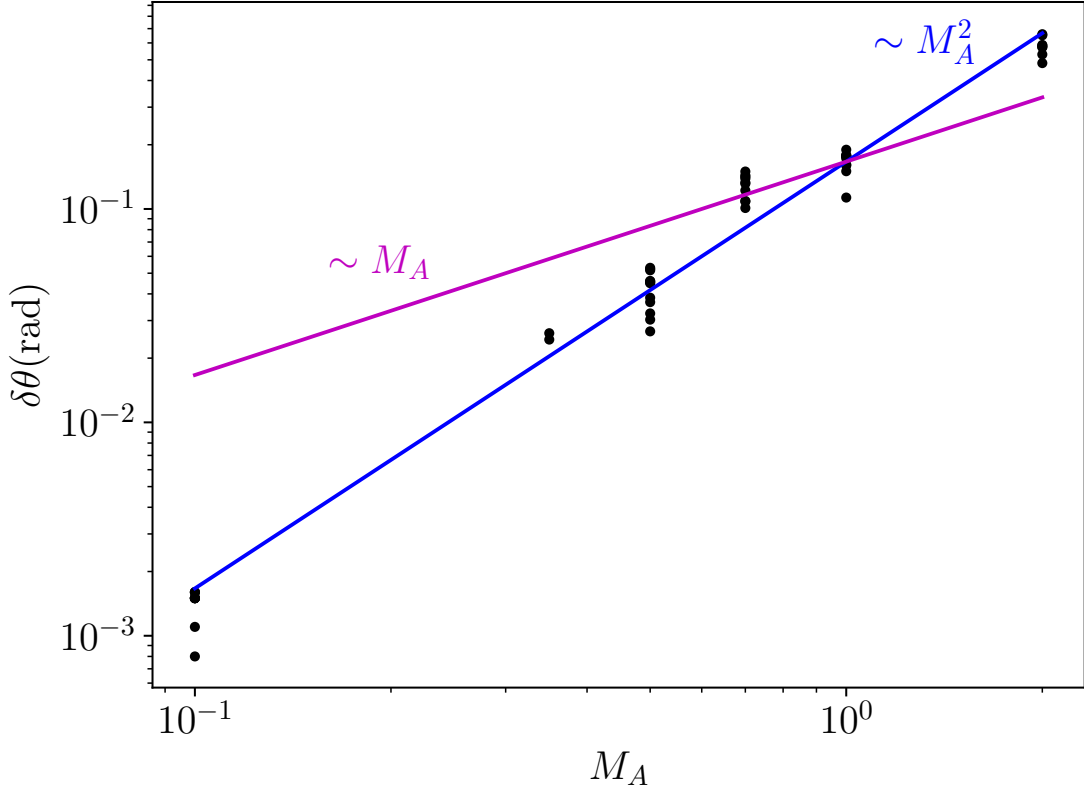


Fig. 6.5 Polarization angle dispersion as a function of the Alfvénic Mach number. Blue line: scaling of the proposed method; magenta line: DCF scaling. The two lines are normalized so that they pass through the data for $\mathcal{M}_A = 1.0$.

consistency with the data. In contrast, the DCF scaling fails to represent the synthetic data. Even if we fine-tune the DCF relation with the use of a factor f à la Ostriker et al. [139], agreement with the data is achieved only around the \mathcal{M}_A values used for the tuning. The scaling slope of DCF is clearly inconsistent with simulation data, regardless of the presence of f .

6.2 Applying the DCF and the proposed method in synthetic data

In this section, we explore the accuracy of the DCF and ST methods in estimating the magnetic field strength. We do not test the DCF+HH09 any further, since the HH09 method

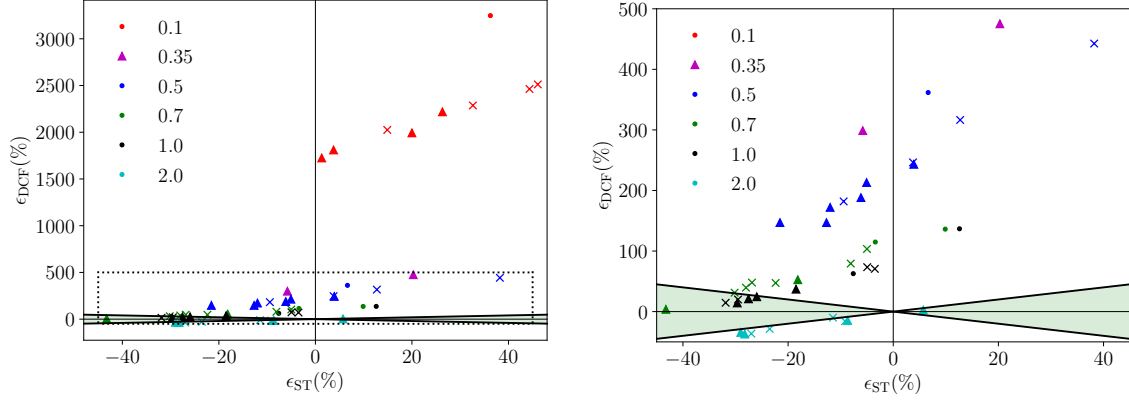


Fig. 6.6 **Left panel:** Relative error of the DCF method versus the relative error of the ST method. Colors correspond to different \mathcal{M}_A as shown in the legend. Dots correspond to simulations with $\mathcal{M}_s < 1$, "x" to $1 < \mathcal{M}_s \leq 4$, and triangles to $\mathcal{M}_s > 4$. The black dotted box marks the zoomed in region shown in the right panel. **Right panel:** Zoomed region of the left panel.

only accounts for projection effects and has other caveats (§ 3) not related with the omission of the compressible modes in the energy budget of a cloud.

To this end, we created synthetic data from every simulation and applied the DCF (with an optimization factor $f = 0.5$) and ST methods. Both methods can be significantly affected when the magnetic field is pointing toward the observer since the LOS angle fluctuations induces extra dispersion in $\delta\theta$ [139, 48, 74]. For this reason, we consider that \vec{B}_0 lies completely in the POS.

To obtain an estimate of $\delta\theta$, we applied the formalism of § 5 (Eqs. 5.8, and 5.9) to calculate the Stokes parameters for each LOS, we estimated polarization angles through $\tan 2\theta = U/2Q$, and calculated the dispersion of θ over the entire cloud through $\delta\theta = \sqrt{\langle \theta^2 \rangle_{2D}}$ (taking $\theta = 0$ in the direction of the mean magnetic field). We then applied the DCF method with $f = 0.5$, and the ST method, by inserting the synthetic δu and $\delta\theta$ in Eqs. (3.5) and (5.4), respectively. We divided both equations with $\sqrt{4\pi\rho_0}$ in order to derive the estimated magnetic field strength in Alfvénic speed units. Finally, we computed their relative error Eq. 6.6.

In Fig. 6.6 we show the relative error of DCF (ϵ_{DCF}) versus ST (ϵ_{ST}). Red color is used for points when $\mathcal{M}_A = 0.1$, magenta for $\mathcal{M}_A = 0.35$, blue for $\mathcal{M}_A = 0.5$, green for $\mathcal{M}_A = 0.7$, black for $\mathcal{M}_A = 1.0$ and cyan for $\mathcal{M}_A = 2.0$. We did not include models with $\mathcal{M}_A = 2.0$ and solenoidal forcing, since the polarization angle distribution of these models is uniform, and thus uninformative. Below we discuss the effect of forcing of these simulations in more detail (§ 6.2.2). The green shaded region corresponds to a smaller error for DCF than for ST.

We find that DCF is extremely inaccurate at low $\mathcal{M}_A \leq 0.5$: when the method fails, it fails by factors of several to tens. The accuracy of the method is improved for $\mathcal{M}_A \geq 1.0$, as expected, since it is in this regime for which the value of f we are using here ($f = 0.5$) has been optimized [139, 72, 142]. The overall trend of this figure is consistent with Fig. 6.1. The DCF method estimates are systematically biased toward larger values, because the kinetic energy of the cloud is much larger than the magnetic fluctuations, even for models with $\mathcal{M}_s = 0.5$ and 0.7. The incompressible approximation employed by DCF is reached when M_s tends to zero, but even for weakly compressible flows (e.g., $\mathcal{M}_s \approx 0.1$) compressible terms can dominate the dynamics [19]. Only in trans-, super- Alfvénic cases DCF starts yielding reasonable estimates, because in this regime the contribution of the $\delta B^2/(8\pi)$ term in the energy increases.

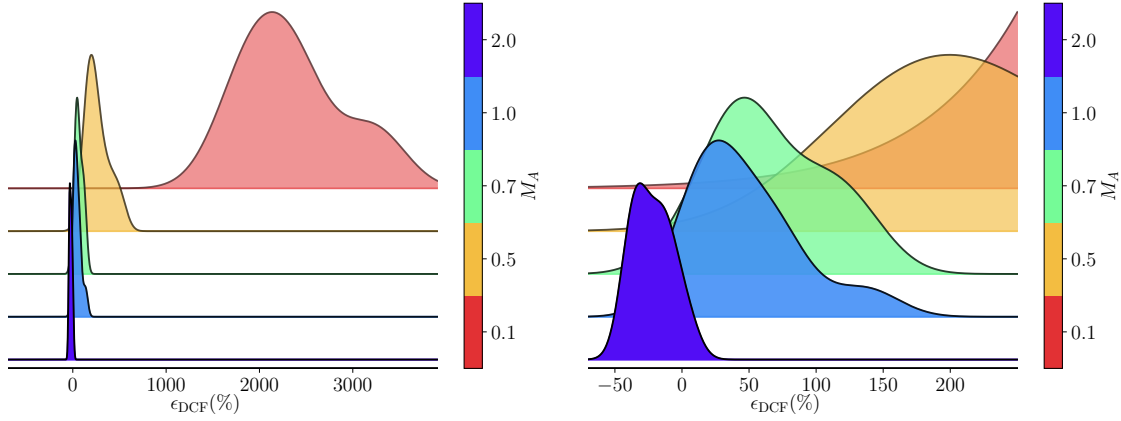


Fig. 6.7 **Left panel:** Kernel density estimation of ϵ_{DCF} for different \mathcal{M}_A simulations. **Right panel:** Zoomed in region of the left panel.

In contrast, the error of the ST method remains low and uniform across the different models, because the kinetic energy remains comparable to the $\vec{B}_0 \cdot \delta \vec{B}$ fluctuations over a wide range of \mathcal{M}_A (Fig. 6.1). The ST method overestimates the magnetic field strength at $\mathcal{M}_A = 0.1$, while at $\mathcal{M}_A = 0.5$ a transition happens. In the latter case half of the measurements overestimate the magnetic field strength, while the rest underestimate it. The underestimation is more prominent at large \mathcal{M}_s , since the deviation between the estimated turbulent velocity and the true one becomes larger (Table 6.2). ST systematically underestimates the magnetic field strength at models with $\mathcal{M}_A \geq 0.7$. However, in all cases the error of ST is lower than 50%.

6.2.1 Statistical properties of ϵ_{DCF} and ϵ_{ST} .

In Fig. 6.7 we show the error distribution for the DCF method, ϵ_{DCF} , at different \mathcal{M}_A , using kernel density estimation. The colorbar indicates the \mathcal{M}_A of each distribution. Red, yellow, green, cyan and blue correspond to simulations with \mathcal{M}_A of 0.1, 0.5, 0.7, 1.0, and 2.0, respectively. It is evident that as \mathcal{M}_A increases ϵ_{DCF} decreases. Distributions become more symmetric and narrow at larger \mathcal{M}_A since the properties of these models are more isotropic. The ϵ_{DCF} mean, median, and standard deviation of all the models with $M_A \geq 0.7$ are 34%, 28%, and 49% respectively. This shows that the method estimates are systematically biased toward large values and the distribution is skewed to positive values. We also computed the same statistical quantities for the absolute values of ϵ_{DCF} for the same models. The mean, median, and standard deviation of $|\epsilon_{\text{DCF}}|$ is 47%, 37%, and 37%, respectively. DCF is completely inaccurate at lower \mathcal{M}_A , and hence we do not report any statistics for these models.

The ϵ_{ST} distributions at different \mathcal{M}_A are shown in Fig. 6.8. Colors are the same as in Fig. 6.7. The ST estimates are biased toward larger values at $M_A = 0.1$, while at $M_A \geq 0.7$ the method estimates are systematically biased toward smaller values. The peak of the $M_A = 0.5$ distribution is close to zero and the probability of overestimating and underestimating the magnetic field strength is equal there. Distributions become more isotropic at larger \mathcal{M}_A , which, similarly to ϵ_{DCF} , happens because the turbulent properties of these models are more isotropic. The ϵ_{ST} mean, median, and standard deviation of all the models are -2% , -6% , and 24% , respectively and the distribution is close to a Gaussian. The same quantities for $|\epsilon_{\text{ST}}|$ are 20% , 18% , and 14% , respectively. The ϵ_{ST} distribution is more symmetric and peaks close to zero. Positive values are dominated by models with $M_A \leq 0.5$, while negative by models with $M_A \geq 0.7$. The right panel of Fig. 6.7 and Fig. 6.8 show the error distributions of the two methods (DCF and ST) on the same scale.

6.2.2 How does forcing affect the polarization data?

The dynamics of a sub-Alfvénic cloud are mainly determined by \vec{B}_0 and forcing has a weak role. On the other hand, in super-Alfvénic turbulence forcing plays a dominant role in the cloud dynamics (§ 6.0.2). We could not apply the two methods (ST and DCF) in simulations with $\mathcal{M}_A = 2.0$ that were driven solenoidally, but we did apply them to simulations with $\mathcal{M}_A = 2.0$ and mixed forcing. The reason is that forcing has a strong impact on the distribution of polarization angles in super-Alfvénic simulations. In Fig. 6.9 we show the normalized polarization angle distributions of simulations with $\mathcal{M}_A = 2.0$ and $\mathcal{M}_s = 2.0$. The black histogram corresponds to a cloud driven solenoidally, while the blue histogram to a cloud

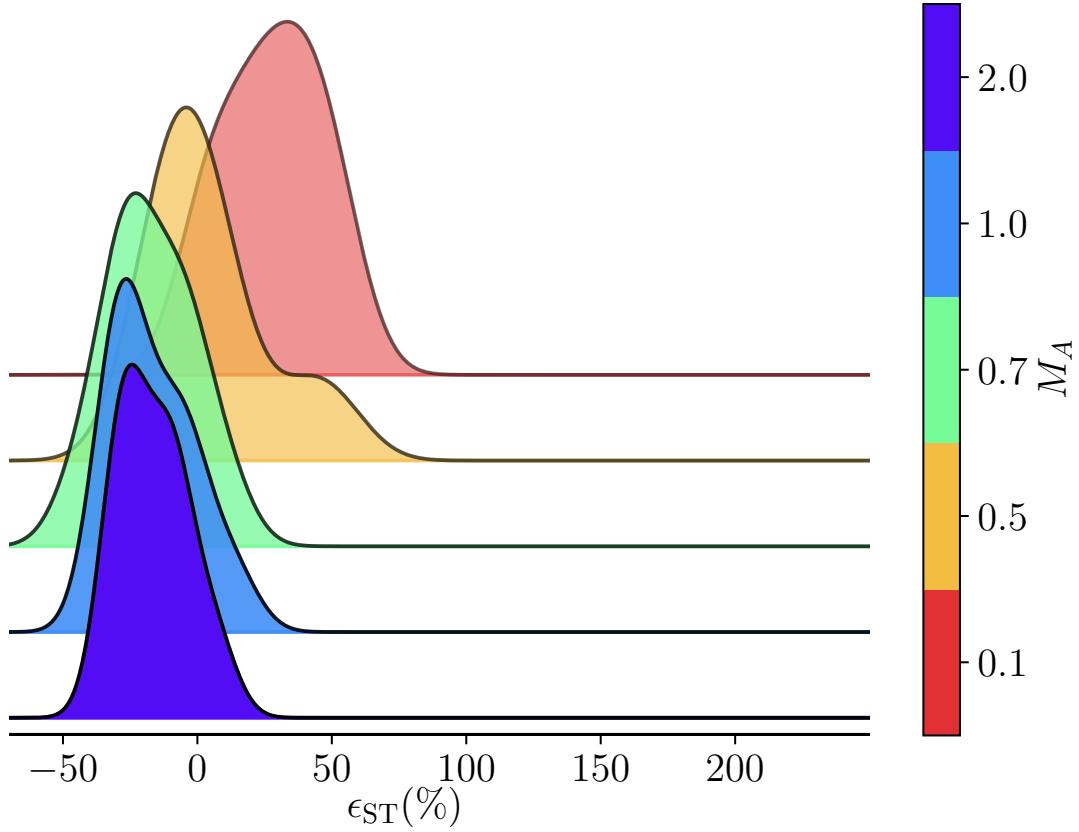


Fig. 6.8 Kernel density estimation of ϵ_{ST} of simulations with different \mathcal{M}_A .

driven with a mixture of modes. The black histogram is uniform and characterized by a spread equal to 48° , while the blue histogram has still a well defined mean with a spread equal to 28° . The dispersion in the black histogram (solenoidal driving) is so large it no longer encodes the magnetic fluctuations, due to the limited domain range, $\delta\theta \in [-90^\circ, 90^\circ]$. In this case neither of the two methods can be applied.

Table 6.2 Simulation properties and methods results.

Refs (1)	Driving (2)	\mathcal{M}_A (3)	\mathcal{M}_s (4)	$V_{A,true}$ (5)	σ_{turb} (6)	$\delta\theta(^{\circ})$ (7)	V_A^{ST} (8)	$\varepsilon_{ST}(\%)$ (9)	V_A^{DCF} (10)	$\varepsilon_{DCF}(\%)$ (11)
1	mixed	0.1	0.5	5	0.36/0.27	0.06/0.05	7.8/6.8	55/36	165/167	3210/3243
1	mixed	0.1	2.0	20	1.47/1.52	0.09/0.09	26.4/27.1	32.3/35	476/480	2280/2302
1	mixed	0.1	4.0	40	3.25/2.43	0.09/0.08	57.8/44.9	32.3/12.3	1034/830	2485/1977
1	mixed	0.1	10.0	100	5.63/6.73	0.08/0.09	103.8/117.5	3.8/17.5	1910/2049	1810/1949
1	mixed	0.1	20.0	200	13.76/11.25	0.09/0.09	252.6/202.6	26.3/1.3	4636/3648	2218/1724
1	mixed	0.5	0.5	1	0.33/0.27	1.73/1.53	1.5/1.1	51.2/6.5	6.1/4.6	514/361
1	mixed	0.5	2.0	4	1.15/1.41	2.96/1.86	3.6/5.5	-9.6/38.2	11.3/21.7	181/442
1	mixed	0.5	4.0	8	1.98/2.44	2.57/2.10	8.3/9.0	3.7/12.7	27.7/33.3	246/316
1	mixed	0.5	10.0	20	6.11/5.76	3.04/2.63	18.8/19.0	-6.1/-5.1	57.6/62.6	188/213
1	mixed	0.5	20.0	40	8.92/13.01	3.00/2.63	35/2/41.5	-12.0/3.9	109/137	172/243
1	mixed	1	0.5	0.5	0.26/0.27	9.24/6.48	0.46/0.56	-7.6/12.7	0.8/1.19	63/137
1	mixed	1	2.0	2	0.83/1.09	9.89/9.16	1.41/1.9	-29.5/-3.5	2.4/3.41	19.9/70.6
1	mixed	1	4.0	4	1.62/2.08	10.12/8.61	2.7/3.8	-31.9/-4.9	4.6/6.9	14.6/73.4
1	mixed	1	10.0	10	4.33/4.41	10.86/10.14	7.0/7.4	-29.67/-26.0	11.4/12.5	14.2/24.4
1	mixed	1	20.0	20	8.68/9.70	10.27/10.14	14.5/16.3	-27.5/-18.5	24.2/27.4	21/37.0
1	mixed	2.0	2.0	1	0.82/0.87	32.91/27.65	0.76/0.88	-23.5/-11.5	0.7/0.9	-28.6/-9.9
1	mixed	2.0	4.0	2	1.68/1.96	37.77/33.43	1.5/1.8	-27.0/-9.2	1.3/1.7	-36.4/-15.9
1	mixed	2.0	10.0	5	4.09/4.89	37.33/32.82	3.6/4.6	-28.2/-8.7	3.1/4.3	-37.1/-14.7
1	mixed	2.0	20.0	10	7.69/10.88	33.63/30.36	7.1/10.6	-29.0/5.8	6.5/10.3	-34.5/2.7
2	sol	0.7	0.7	0.91	0.46/0.39	6.21/5.79	0.99/0.87	9.5/-3.4	2.1/2.0	135/115
2	sol	0.7	1.0	1.60	0.58/0.71	7.00/6.25	1.2/1.6	-26.9/-5.0	2.4/3.3	47.9/103
2	sol	0.7	2.0	2.87	1.35/1.07	7.53/7.63	2.6/2.1	-8.1/-28.0	5.2/4.0	79.3/39.5
2	sol	0.7	4.0	5.09	1.89/2.08	8.11/7.96	3.6/3.9	-30.2/-22.4	6.7/7.5	31.3/47.3
2	sol	0.7	7.0	9.10	3.99/2.83	8.24/8.58	7.4/5.2	-18.1/-43.2	13.9/9.4	52.6/3.7
3	sol	0.5	7.5	2.86	0.76/0.71	2.6/2.9	2.5/2.2	-12.7/-21.5	8.1/7.1	185/147
4	sol	0.35	10	28.6	6.4/7.2	1.5/1.4	26.9/34.4	-5.8/20.3	348/525	299/475

Column 1: (1) Beattie et al. [14]; (2) Burkhart et al. [24]; (3) Körtgen and Soler [94]; (4) Mocz et al. [123]. Column 2: "sol" refers to solenoidal forcing, and "mixed" to mixed forcing. σ_{turb} is measured in km/s and $\delta\theta$ in degrees; when estimating V_A^{ST} and V_A^{DCF} , $\delta\theta$ is used in radians.

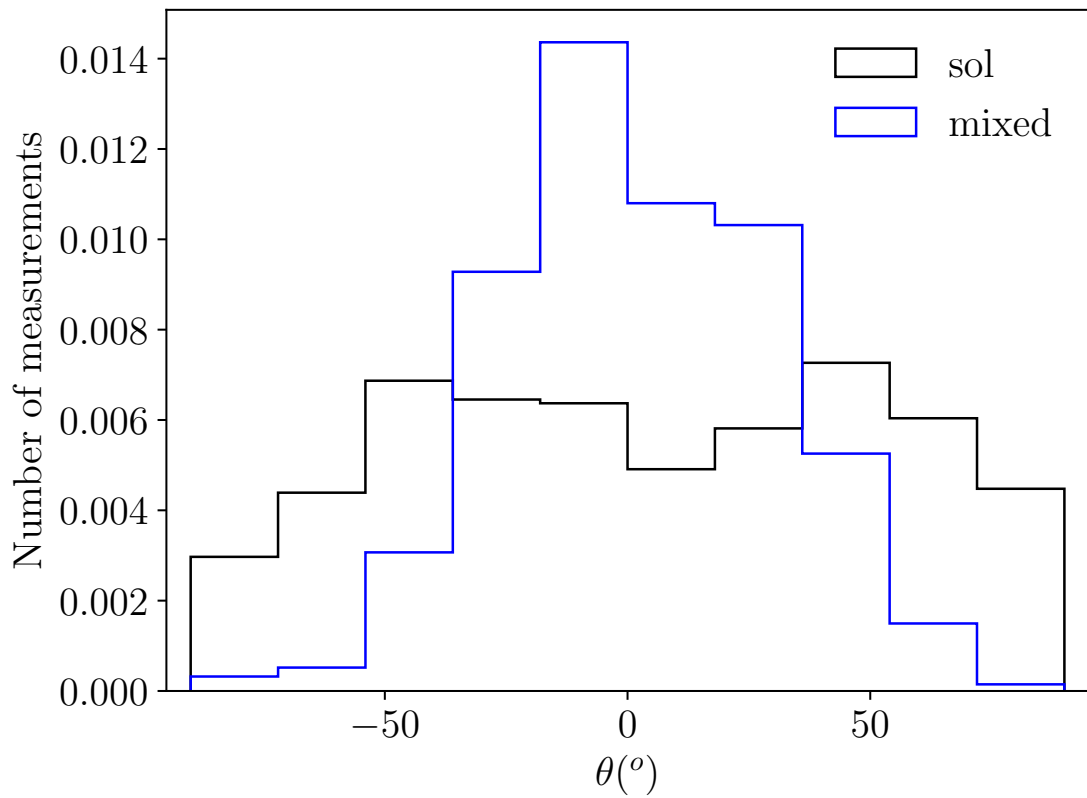


Fig. 6.9 Polarization angle distributions for two different simulations with $\mathcal{M}_A = 2.0$ and $\mathcal{M}_s = 2.0$. Black histogram corresponds to solenoidally driven cloud, while the blue to mixed forcing. Both histograms are normalized by dividing each bin with the total number of measurements. The legend shows the type of forcing.

Chapter 7

Conclusions

Dust polarization traces the magnetic field orientation in the POS, but not its strength. DCF and HH09 are the most widely applied methods that employ polarization data in order to estimate the strength of the field. They rely on the assumption that isotropic gas turbulent motions induce the propagation of small amplitude Alfvén waves, $|\delta\vec{B}| \ll |\vec{B}_0|$. Observations indicate that turbulence in the ISM is highly anisotropic (§ 3.1.2). The sufficiently high \mathcal{M}_s in the ISM [70] implies that compressible modes are important. The DCF method neglects the compressible modes, and hence the estimates of the magnetic field it provides deviate significantly from the true value. We presented a Lagrangian description of the energy transfer between kinetic and magnetic fluctuations of compressible and sub-Alfvénic fluids. From the flux-freezing theorem, we showed that δB_{\parallel} and δB_{\perp} are generalized coordinates of the fluid element Lagrangian. We derived analytically the linear relations, as a function of \mathcal{M}_A , which connect kinetic and magnetic energy terms of sub-Alfvénic fluids. We found that when $\mathcal{M}_A \leq 1$, the total magnetic energy density transferred to kinetic is equal to $\left(2B_0\sqrt{\langle\delta B_{\parallel}^2\rangle} + \langle\delta B^2\rangle\right)/8\pi$ (§ 4).

Using our analytical energy relations we derived a new method for estimating the magnetic field strength from dust polarization which, unlike DCF, includes the compressible modes. We inferred that $\delta\theta \propto \mathcal{M}_A^2$, while the DCF method, which employs the incompressible approximation, infers that $\delta\theta \propto \mathcal{M}_A$. We tested both scalings with synthetic data that we produced from ideal-MHD numerical simulations of isothermal clouds without self-gravity, spanning a wide range of \mathcal{M}_A and \mathcal{M}_s ($\mathcal{M}_s \in [0.5, 20]$ and $\mathcal{M}_A \in [0.1, 2.0]$). In total we used 26 different models. We found that the synthetic polarization data can be fit very well with our new scaling and not with the DCF scaling (Fig. 6.5).

The major difference between the two methods is that in the DCF energy equation (Eq. 3.2) by definition $\delta\vec{B} \cdot \vec{B}_0 = 0$, since only Alfvénic distortions are assumed to be present.

On the other hand, we relaxed this assumption and considered the more general case of compressible fluctuations where $\delta\vec{B} \cdot \vec{B}_0 \neq 0$ (Eq. 5.4).

We have explored whether the averaging over the total volume of a cloud can make this term vanish in the energetics, even if locally it is nonzero. We showed that $\langle \delta\vec{B} \cdot \vec{B}_0 \rangle = 0$ is obtained only if the zero-point of the magnetic "potential energy" is taken to be at $\delta\vec{B} = 0$, rather than at the point of minimum potential energy, $\delta\vec{B} = -\delta\vec{B}_{\text{max}}$. By making a simple analogy with the problem of a bouncing ball in Newtonian gravity, we showed that for compressible fluctuations the correct energy conservation equation is obtained when comparing the kinetic energy with the rms of the $\vec{B}_0 \cdot \delta\vec{B}$ in the magnetic energy equation, which then naturally leads to our new equation for the magnetic field strength (Eq. 5.4). We have tested our theoretical arguments with numerical data and found that indeed the rms of $\vec{B}_0 \cdot \delta\vec{B}$ compares very well with the kinetic energy in all cases studied, with the exception of super-Alfvénic simulations with solenoidal forcing (see Fig. 6.1). On the other hand, when we omit this term, the kinetic energy can be up to two orders of magnitude larger than the magnetic energy (§ 4). This explains why our method predicts the right scaling between $\delta\theta$ - \mathcal{M}_A , while DCF do not.

We explored if $\vec{B}_0 \cdot \delta\vec{B}$ is imprinted in $\delta\theta$. We showed analytically that when $|\vec{B}_0| \gg |\delta\vec{B}|$ the zeroth order approximation of $\delta\theta$ refers to perpendicular magnetic field fluctuations and the first order corrections correspond to compressible modes. However, the rms amplitude of parallel and perpendicular fluctuations is in all cases comparable, with deviations smaller than a factor of 2. As a result, $\delta\theta$ provides, indirectly, information about the amplitude of parallel fluctuations even to zeroth order.

We tested the accuracy of the two methods in estimating the magnetic field strength. We found that the DCF method with a "fudge factor" $f = 0.5$ failed completely in clouds with $\mathcal{M}_A \leq 0.5$ and only started producing reasonable estimates when $\mathcal{M}_A \gtrsim 0.7$. The lowest errors for DCF were achieved for trans-,super- Alfvénic turbulence, $\mathcal{M}_A \geq 1.0$, because this is the regime for which the "fudge factor" $f = 0.5$ we have used was fine-tuned [139, 72, 142]. Even in this regime ($\mathcal{M}_A \geq 0.7$ clouds), the relative error of DCF lied in the range $[-37, 137]\%$. Over the entire \mathcal{M}_A range, the error of DCF lied in the range $[-37, 3500]\%$. ; Even when DCF was combined with the HH09 method, in order to account for projection effects, the estimates improved only in a few cases (§ 6.0.3).

The proposed method, on the other hand, gave good results for all \mathcal{M}_A examined here, without any fine tuning: the relative deviation from the true value lied in the range $[-43, 51]\%$ over the entire \mathcal{M}_A . We did not find any strong dependence of the accuracy of the methods on \mathcal{M}_s . Even in the cases where DCF would outperform the proposed method, the proposed

method would still provide an adequate estimate of the magnetic field strength, while the reverse is not true.

The main question posed in the current thesis was: How can we estimate the magnetic field strength from dust polarization with high accuracy, such that deviations do not exceed the factor of two? We conclude that the answer to this question is the following equation:

$$B_0 = \sqrt{4\pi\rho} \frac{\langle u_{\perp}^2 \rangle^{1/2}}{\sqrt{2\delta\theta}}.$$

References

- [1] Alfvén, H. (1942). Existence of Electromagnetic-Hydrodynamic Waves. *Nature*, 150(3805):405–406.
- [2] Alves, J., Lombardi, M., and Lada, C. J. (2017). The shapes of column density PDFs. The importance of the last closed contour. *A&A*, 606:L2.
- [3] Alves, M. I. R., Boulanger, F., Ferrière, K., and Montier, L. (2018). The Local Bubble: a magnetic veil to our Galaxy. *A&A*, 611:L5.
- [4] Andersson, B. G., Lazarian, A., and Vaillancourt, J. E. (2015). Interstellar Dust Grain Alignment. *ARA&A*, 53:501–539.
- [5] Andersson, B. G., Lopez-Rodriguez, E., Medan, I., Soam, A., Hoang, T., Vaillancourt, J. E., Lazarian, A., Sandin, C., Mattsson, L., and Tahani, M. (2022). Grain Alignment in the Circumstellar Shell of IRC+10° 216. *ApJ*, 931(2):80.
- [6] André, P., Hughes, A., Guillet, V., Boulanger, F., Bracco, A., Ntormousi, E., Arzoumanian, D., Maury, A. J., Bernard, J. P., Bontemps, S., Ristorcelli, I., Girart, J. M., Motte, F., Tassis, K., Pantin, E., Montmerle, T., Johnstone, D., Gabici, S., Efstathiou, A., Basu, S., Béthermin, M., Beuther, H., Braine, J., Francesco, J. D., Falgarone, E., Ferrière, K., Fletcher, A., Galametz, M., Giard, M., Hennebelle, P., Jones, A., Kepley, A. A., Kwon, J., Lagache, G., Lesaffre, P., Levrier, F., Li, D., Li, Z. Y., Mao, S. A., Nakagawa, T., Onaka, T., Paladino, R., Peretto, N., Poglitsch, A., Revéret, V., Rodriguez, L., Sauvage, M., Soler, J. D., Spinoglio, L., Tabatabaei, F., Tritsis, A., van der Tak, F., Ward-Thompson, D., Wiesemeyer, H., Ysard, N., and Zhang, H. (2019). Probing the cold magnetised Universe with SPICA-POL (B-BOP). *PASA*, 36:e029.
- [7] André, P., Men'shchikov, A., Bontemps, S., Könyves, V., Motte, F., Schneider, N., Didelon, P., Minier, V., Saraceno, P., Ward-Thompson, D., di Francesco, J., White, G., Molinari, S., Testi, L., Abergel, A., Griffin, M., Henning, T., Royer, P., Merín, B., Vavrek, R., Attard, M., Arzoumanian, D., Wilson, C. D., Ade, P., Aussel, H., Baluteau, J. P., Benedettini, M., Bernard, J. P., Blommaert, J. A. D. L., Cambrésy, L., Cox, P., di Giorgio, A., Hargrave, P., Hennemann, M., Huang, M., Kirk, J., Krause, O., Launhardt, R., Leeks, S., Le Pennec, J., Li, J. Z., Martin, P. G., Maury, A., Olofsson, G., Omont, A., Peretto, N., Pezzuto, S., Prusti, T., Roussel, H., Russeil, D., Sauvage, M., Sibthorpe, B., Sicilia-Aguilar, A., Spinoglio, L., Waelkens, C., Woodcraft, A., and Zavagno, A. (2010). From filamentary clouds to prestellar cores to the stellar IMF: Initial highlights from the Herschel Gould Belt Survey. *A&A*, 518:L102.

- [8] Andreussi, T., Morrison, P. J., and Pegoraro, F. (2016). Hamiltonian magnetohydrodynamics: Lagrangian, Eulerian, and dynamically accessible stability—Examples with translation symmetry. *Physics of Plasmas*, 23(10):102112.
- [9] Arzoumanian, D., Furuya, R. S., Hasegawa, T., Tahani, M., Sadavoy, S., Hull, C. L. H., Johnstone, D., Koch, P. M., Inutsuka, S., Doi, Y., Hoang, T., Onaka, T., Iwasaki, K., Shimajiri, Y., Inoue, T., Peretto, N., André, P., Bastien, P., Berry, D., Chen, H. R. V., Di Francesco, J., Eswaraiah, C., Fanciullo, L., Fissel, L. M., Hwang, J., Kang, J. h., Kim, G., Kim, K. T., Kirchschrager, F., Kwon, W., Lee, C. W., Liu, H. L., Lyo, A. R., Pattle, K., Soam, A., Tang, X., Whitworth, A., Ching, T. C., Coudé, S., Wang, J. W., Ward-Thompson, D., Lai, S. P., Qiu, K., Bourke, T. L., Byun, D. Y., Chen, M., Chen, Z., Chen, W. P., Cho, J., Choi, Y., Choi, M., Chrysostomou, A., Chung, E. J., Dai, S., Diep, P. N., Duan, H. Y., Duan, Y., Eden, D., Fiege, J., Franzmann, E., Friberg, P., Fuller, G., Gledhill, T., Graves, S., Greaves, J., Griffin, M., Gu, Q., Han, I., Hatchell, J., Hayashi, S., Houde, M., Jeong, I. G., Kang, M., Kang, S. j., Kataoka, A., Kawabata, K., Kemper, F., Kim, M. R., Kim, K. H., Kim, J., Kim, S., Kirk, J., Kobayashi, M. I. N., Könyves, V., Kusune, T., Kwon, J., Lacaille, K., Law, C. Y., Lee, C. F., Lee, Y. H., Lee, S. S., Lee, H., Lee, J. E., Li, H. b., Li, D., Li, D. L., Liu, J., Liu, T., Liu, S. Y., Lu, X., Mairs, S., Matsumura, M., Matthews, B., Moriarty-Schieven, G., Nagata, T., Nakamura, F., Nakanishi, H., Ngoc, N. B., Ohashi, N., Park, G., Parsons, H., Pyo, T. S., Qian, L., Rao, R., Rawlings, J., Rawlings, M., Retter, B., Richer, J., Rigby, A., Saito, H., Savini, G., Scaife, A., Seta, M., Shinnaga, H., Tamura, M., Tang, Y. W., Tomisaka, K., Tram, L. N., Tsukamoto, Y., Viti, S., Wang, H., Xie, J., Yen, H. W., Yoo, H., Yuan, J., Yun, H. S., Zenko, T., Zhang, G., Zhang, C. P., Zhang, Y., Zhou, J., Zhu, L., de Looze, I., Dowell, C. D., Eyres, S., Falle, S., Friesen, R., Robitaille, J. F., and van Loo, S. (2021). Dust polarized emission observations of NGC 6334. BISTRO reveals the details of the complex but organized magnetic field structure of the high-mass star-forming hub-filament network. *A&A*, 647:A78.
- [10] Basu, S., Ciolek, G. E., Dapp, W. B., and Wurster, J. (2009a). Magnetically-regulated fragmentation induced by nonlinear flows and ambipolar diffusion. *New Astron.*, 14(5):483–495.
- [11] Basu, S., Ciolek, G. E., Dapp, W. B., and Wurster, J. (2009b). Magnetically-regulated fragmentation induced by nonlinear flows and ambipolar diffusion. *New Astron.*, 14(5):483–495.
- [12] Beattie, J. R. and Federrath, C. (2020). Filaments and striations: anisotropies in observed, supersonic, highly magnetized turbulent clouds. *MNRAS*, 492(1):668–685.
- [13] Beattie, J. R., Federrath, C., Klessen, R. S., and Schneider, N. (2019). The relation between the turbulent Mach number and observed fractal dimensions of turbulent clouds. *MNRAS*, 488(2):2493–2502.
- [14] Beattie, J. R., Federrath, C., and Seta, A. (2020). Magnetic field fluctuations in anisotropic, supersonic turbulence. *MNRAS*.
- [15] Beattie, J. R., Krumholz, M. R., Skolidis, R., Federrath, C., Seta, A., Crocker, R. M., Mocz, P., and Kriel, N. (2022). Energy balance and Alfvén Mach numbers in compressible magnetohydrodynamic turbulence with a large-scale magnetic field. *arXiv e-prints*, page arXiv:2202.13020.

- [16] Beattie, J. R., Mocz, P., Federrath, C., and Klessen, R. S. (2021). A multishock model for the density variance of anisotropic, highly magnetized, supersonic turbulence. *MNRAS*, 504(3):4354–4368.
- [17] Bellomi, E., Godard, B., Hennebelle, P., Valdivia, V., Pineau des Forêts, G., Lesaffre, P., and Péroult, M. (2020). 3D chemical structure of diffuse turbulent ISM. I. Statistics of the HI-to-H₂ transition. *A&A*, 643:A36.
- [18] Bhattacharjee, A. and Hameiri, E. (1988). Energy confinement in turbulent fluid plasmas. *Physics of Fluids*, 31(5):1153–1160.
- [19] Bhattacharjee, A., Ng, C. S., and Spangler, S. R. (1998). Weakly Compressible Magnetohydrodynamic Turbulence in the Solar Wind and the Interstellar Medium. *ApJ*, 494(1):409–418.
- [20] Bialy, S. and Burkhart, B. (2020). The Driving Scale-Density Decorrelation Scale Relation in a Turbulent Medium. *ApJ*, 894(1):L2.
- [21] Brandenburg, A. and Ntormousi, E. (2022). Dynamo effect in unstirred self-gravitating turbulence. *MNRAS*, 513(2):2136–2151.
- [22] Brunt, C. M. (2010). The density variance - Mach number relation in the Taurus molecular cloud. *A&A*, 513:A67.
- [23] Burkhart, B., Appel, S. M., Bialy, S., Cho, J., Christensen, A. J., Collins, D., Federrath, C., Fielding, D. B., Finkbeiner, D., Hill, A. S., Ibáñez-Mejía, J. C., Krumholz, M. R., Lazarian, A., Li, M., Mocz, P., Mac Low, M. M., Naiman, J., Portillo, S. K. N., Shane, B., Slepian, Z., and Yuan, Y. (2020). The Catalogue for Astrophysical Turbulence Simulations (CATS). *ApJ*, 905(1):14.
- [24] Burkhart, B., Falceta-Gonçalves, D., Kowal, G., and Lazarian, A. (2009). Density Studies of MHD Interstellar Turbulence: Statistical Moments, Correlations and Bispectrum. *ApJ*, 693(1):250–266.
- [25] Burkhart, B., Lee, M.-Y., Murray, C. E., and Stanimirović, S. (2015). The Lognormal Probability Distribution Function of the Perseus Molecular Cloud: A Comparison of HI and Dust. *ApJ*, 811(2):L28.
- [26] Burkhart, B. and Mocz, P. (2019). The Self-gravitating Gas Fraction and the Critical Density for Star Formation. *ApJ*, 879(2):129.
- [27] Chandrasekhar, S. and Fermi, E. (1953a). Magnetic Fields in Spiral Arms. *ApJ*, 118:113.
- [28] Chandrasekhar, S. and Fermi, E. (1953b). Problems of Gravitational Stability in the Presence of a Magnetic Field. *ApJ*, 118:116.
- [29] Chandrasekhar, S. and Kendall, P. C. (1957). On Force-Free Magnetic Fields. *ApJ*, 126:457.
- [30] Ching, T. C., Li, D., Heiles, C., Li, Z. Y., Qian, L., Yue, Y. L., Tang, J., and Jiao, S. H. (2022). An early transition to magnetic supercriticality in star formation. *Nature*, 601(7891):49–52.

- [31] Chitsazzadeh, S., Houde, M., Hildebrand, R. H., and Vaillancourt, J. (2012). Characterization of Turbulence from Submillimeter Dust Emission. *ApJ*, 749(1):45.
- [32] Cho, J. and Lazarian, A. (2002). Compressible Sub-Alfvénic MHD Turbulence in Low- β Plasmas. *Phys. Rev. Lett.*, 88(24):245001.
- [33] Cho, J. and Lazarian, A. (2003). Compressible magnetohydrodynamic turbulence: mode coupling, scaling relations, anisotropy, viscosity-damped regime and astrophysical implications. *MNRAS*, 345(12):325–339.
- [34] Cho, J. and Vishniac, E. T. (2000). The Generation of Magnetic Fields through Driven Turbulence. *ApJ*, 538(1):217–225.
- [35] Cho, J. and Yoo, H. (2016). A Technique for Constraining the Driving Scale of Turbulence and a Modified Chandrasekhar-Fermi Method. *ApJ*, 821(1):21.
- [36] Chuss, D. T., Andersson, B. G., Bally, J., Dotson, J. L., Dowell, C. D., Guerra, J. A., Harper, D. A., Houde, M., Jones, T. J., Lazarian, A., Lopez Rodriguez, E., Michail, J. M., Morris, M. R., Novak, G., Siah, J., Staguhn, J., Vaillancourt, J. E., Volpert, C. G., Werner, M., Wollack, E. J., Benford, D. J., Berthoud, M., Cox, E. G., Crutcher, R., Dale, D. A., Fissel, L. M., Goldsmith, P. F., Hamilton, R. T., Hanany, S., Henning, T. K., Looney, L. W., Moseley, S. H., Santos, F. P., Stephens, I., Tassis, K., Trinh, C. Q., Van Camp, E., Ward-Thompson, D., and HAWC + Science Team (2019). HAWC+/SOFIA Multiwavelength Polarimetric Observations of OMC-1. *ApJ*, 872(2):187.
- [37] Clark, S. E., Peek, J. E. G., and Putman, M. E. (2014). Magnetically Aligned H I Fibers and the Rolling Hough Transform. *ApJ*, 789(1):82.
- [38] Cox, N. L. J., Arzoumanian, D., André, P., Rygl, K. L. J., Prusti, T., Men'shchikov, A., Royer, P., Kóspál, Á., Palmeirim, P., Ribas, A., Könyves, V., Bernard, J. P., Schneider, N., Bontemps, S., Merin, B., Vavrek, R., Alves de Oliveira, C., Didelon, P., Pilbratt, G. L., and Waelkens, C. (2016). Filamentary structure and magnetic field orientation in Musca. *A&A*, 590:A110.
- [39] Crutcher, R. M. and Kemball, A. J. (2019). Review of Zeeman Effect Observations of Regions of Star Formation K Zeeman Effect, Magnetic Fields, Star formation, Masers, Molecular clouds. *Frontiers in Astronomy and Space Sciences*, 6:66.
- [40] Crutcher, R. M., Wandelt, B., Heiles, C., Falgarone, E., and Troland, T. H. (2010). Magnetic Fields in Interstellar Clouds from Zeeman Observations: Inference of Total Field Strengths by Bayesian Analysis. *ApJ*, 725(1):466–479.
- [41] Davis, Leverett, J. and Greenstein, J. L. (1951). The Polarization of Starlight by Aligned Dust Grains. *ApJ*, 114:206.
- [42] Davis, L. (1951). The strength of interstellar magnetic fields. *Phys. Rev.*, 81:890–891.
- [43] Dolginov, A. Z. and Mitrofanov, I. G. (1976). Orientation of Cosmic Dust Grains. *Ap&SS*, 43(2):291–317.
- [44] Draine, B. T. (2011). *Physics of the Interstellar and Intergalactic Medium*.

- [45] Draine, B. T. and Weingartner, J. C. (1996). Radiative Torques on Interstellar Grains. I. Superthermal Spin-up. *ApJ*, 470:551.
- [46] Dubey, A., Fisher, R., Graziani, C., Jordan, G. C., I., Lamb, D. Q., Reid, L. B., Rich, P., Sheeler, D., Townsley, D., and Weide, K. (2008). Challenges of Extreme Computing using the FLASH code. In Pogorelov, N. V., Audit, E., and Zank, G. P., editors, *Numerical Modeling of Space Plasma Flows*, volume 385 of *Astronomical Society of the Pacific Conference Series*, page 145.
- [47] Evans, N. J., Kim, J.-G., and Ostriker, E. C. (2022). Slow Star Formation in the Milky Way: Theory Meets Observations. *ApJ*, 929(1):L18.
- [48] Falceta-Gonçalves, D., Lazarian, A., and Kowal, G. (2008). Studies of Regular and Random Magnetic Fields in the ISM: Statistics of Polarization Vectors and the Chandrasekhar-Fermi Technique. *ApJ*, 679(1):537–551.
- [49] Federrath, C. (2016a). Magnetic field amplification in turbulent astrophysical plasmas. *Journal of Plasma Physics*, 82(6):535820601.
- [50] Federrath, C. (2016b). Magnetic field amplification in turbulent astrophysical plasmas. *Journal of Plasma Physics*, 82(6):535820601.
- [51] Federrath, C., Klessen, R. S., Iapichino, L., and Beattie, J. R. (2021). The sonic scale of interstellar turbulence. *Nature Astronomy*, 5:365–371.
- [52] Field, G. B., Goldsmith, D. W., and Habing, H. J. (1969). Cosmic-Ray Heating of the Interstellar Gas. *ApJ*, 155:L149.
- [53] Fissel, L. M., Ade, P. A. R., Angilè, F. E., Ashton, P., Benton, S. J., Devlin, M. J., Dober, B., Fukui, Y., Galitzki, N., Gandilo, N. N., Klein, J., Korotkov, A. L., Li, Z.-Y., Martin, P. G., Matthews, T. G., Moncelsi, L., Nakamura, F., Netterfield, C. B., Novak, G., Pascale, E., Poidevin, F., Santos, F. P., Savini, G., Scott, D., Shariff, J. A., Diego Soler, J., Thomas, N. E., Tucker, C. E., Tucker, G. S., and Ward-Thompson, D. (2016). Balloon-Borne Submillimeter Polarimetry of the Vela C Molecular Cloud: Systematic Dependence of Polarization Fraction on Column Density and Local Polarization-Angle Dispersion. *ApJ*, 824(2):134.
- [54] Franco, G. A. P. and Alves, F. O. (2015). Tracing the Magnetic Field Morphology of the Lupus I Molecular Cloud. *ApJ*, 807(1):5.
- [55] Franco, G. A. P., Alves, F. O., and Girart, J. M. (2010). Detailed Interstellar Polarimetric Properties of the Pipe Nebula at Core Scales. *ApJ*, 723(1):146–165.
- [56] Fryxell, B., Olson, K., Ricker, P., Timmes, F. X., Zingale, M., Lamb, D. Q., MacNeice, P., Rosner, R., Truran, J. W., and Tufo, H. (2000). FLASH: An Adaptive Mesh Hydrodynamics Code for Modeling Astrophysical Thermonuclear Flashes. *ApJS*, 131(1):273–334.
- [57] Fujimura, D. and Tsuneta, S. (2009). Properties of Magnetohydrodynamic Waves in the Solar Photosphere Obtained with Hinode. *ApJ*, 702(2):1443–1457.

- [58] Gaia Collaboration, Brown, A. G. A., Vallenari, A., Prusti, T., de Bruijne, J. H. J., Babusiaux, C., Bailer-Jones, C. A. L., Biermann, M., Evans, D. W., Eyer, L., and et al. (2018). Gaia Data Release 2. Summary of the contents and survey properties. *A&A*, 616:A1.
- [59] Gaia Collaboration, Brown, A. G. A., Vallenari, A., Prusti, T., de Bruijne, J. H. J., Babusiaux, C., Biermann, M., Creevey, O. L., Evans, D. W., Eyer, L., Hutton, A., Jansen, F., Jordi, C., Klioner, S. A., Lammers, U., Lindegren, L., Luri, X., Mignard, F., Panem, C., Pourbaix, D., Randich, S., Sartoretti, P., Soubiran, C., Walton, N. A., Arenou, F., Bailer-Jones, C. A. L., Bastian, U., Cropper, M., Drimmel, R., Katz, D., Lattanzi, M. G., van Leeuwen, F., Bakker, J., Cacciari, C., Castañeda, J., De Angeli, F., Ducourant, C., Fabricius, C., Fouesneau, M., Frémat, Y., Guerra, R., Guerrier, A., Guiraud, J., Jean-Antoine Piccolo, A., Masana, E., Messineo, R., Mowlavi, N., Nicolas, C., Nienartowicz, K., Pailer, F., Panuzzo, P., Riclet, F., Roux, W., Seabroke, G. M., Sordo, R., Tanga, P., Thévenin, F., Gracia-Abril, G., Portell, J., Teyssier, D., Altmann, M., Andrae, R., Bellas-Velidis, I., Benson, K., Berthier, J., Blomme, R., Brugaletta, E., Burgess, P. W., Busso, G., Carry, B., Cellino, A., Cheek, N., Clementini, G., Damerdj, Y., Davidson, M., Delchambre, L., Dell’Oro, A., Fernández-Hernández, J., Galluccio, L., García-Lario, P., Garcia-Reinaldos, M., González-Núñez, J., Gosset, E., Haigron, R., Halbwachs, J. L., Hambly, N. C., Harrison, D. L., Hatzidimitriou, D., Heiter, U., Hernández, J., Hestroffer, D., Hodgkin, S. T., Holl, B., Janßen, K., Jevardat de Fombelle, G., Jordan, S., Krone-Martins, A., Lanzafame, A. C., Löffler, W., Lorca, A., Manteiga, M., Marchal, O., Marrese, P. M., Moitinho, A., Mora, A., Muinonen, K., Osborne, P., Pancino, E., Pauwels, T., Petit, J. M., Recio-Blanco, A., Richards, P. J., Riello, M., Rimoldini, L., Robin, A. C., Roegiers, T., Rybizki, J., Sarro, L. M., Siopis, C., Smith, M., Sozzetti, A., Ulla, A., Utrilla, E., van Leeuwen, M., van Reeve, W., Abbas, U., Abreu Aramburu, A., Accart, S., Aerts, C., Aguado, J. J., Ajaj, M., Altavilla, G., Álvarez, M. A., Álvarez Cid-Fuentes, J., Alves, J., Anderson, R. I., Anglada Varela, E., Antoja, T., Audard, M., Baines, D., Baker, S. G., Balaguer-Núñez, L., Balbinot, E., Balog, Z., Barache, C., Barbato, D., Barros, M., Barstow, M. A., Bartolomé, S., Bassilana, J. L., Bauchet, N., Baudesson-Stella, A., Becciani, U., Bellazzini, M., Bernet, M., Bertone, S., Bianchi, L., Blanco-Cuaresma, S., Boch, T., Bombrun, A., Bossini, D., Bouquillon, S., Bragaglia, A., Bramante, L., Breedt, E., Bressan, A., Brouillet, N., Bucciarelli, B., Burlacu, A., Busonero, D., Butkevich, A. G., Buzzi, R., Caffau, E., Cancelliere, R., Cánovas, H., Cantat-Gaudin, T., Carballo, R., Carlucci, T., Carnerero, M. I., Carrasco, J. M., Casamiquela, L., Castellani, M., Castro-Ginard, A., Castro Sampil, P., Chaoul, L., Charlot, P., Chemin, L., Chiavassa, A., Cioni, M. R. L., Comoretto, G., Cooper, W. J., Cornez, T., Cowell, S., Crifo, F., Crosta, M., Crowley, C., Dafonte, C., Dapergolas, A., David, M., David, P., de Laverny, P., De Luise, F., De March, R., De Ridder, J., de Souza, R., de Teodoro, P., de Torres, A., del Peloso, E. F., del Pozo, E., Delbo, M., Delgado, A., Delgado, H. E., Delisle, J. B., Di Matteo, P., Diakite, S., Diener, C., Distefano, E., Dolding, C., Eappachen, D., Edvardsson, B., Enke, H., Esquej, P., Fabre, C., Fabrizio, M., Faigler, S., Fedorets, G., Fernique, P., Fienga, A., Figueras, F., Fouron, C., Fragkoudi, F., Fraile, E., Franke, F., Gai, M., Garabato, D., Garcia-Gutierrez, A., García-Torres, M., Garofalo, A., Gavras, P., Gerlach, E., Geyer, R., Giacobbe, P., Gilmore, G., Girona, S., Giuffrida, G., Gomel, R., Gomez, A., Gonzalez-Santamaria, I., González-Vidal, J. J., Granvik, M., Gutiérrez-Sánchez, R., Guy, L. P., Hauser, M., Haywood, M., Helmi, A., Hidalgo, S. L., Hilger, T., Hładczuk, N., Hobbs, D., Holland, G., Huckle, H. E., Jasiewicz, G., Jonker, P. G., Juaristi Campillo, J., Julbe, F., Karbevská, L., Kervella, P., Khanna, S., Kochoska, A., Kontizas, M., Kordopatis,

- G., Korn, A. J., Kostrzewa-Rutkowska, Z., Kruszyńska, K., Lambert, S., Lanza, A. F., Lasne, Y., Le Campion, J. F., Le Fustec, Y., Lebreton, Y., Lebzelter, T., Leccia, S., Leclerc, N., Lecoeur-Taibi, I., Liao, S., Licata, E., Lindstrøm, E. P., Lister, T. A., Livanou, E., Lobel, A., Madrero Pardo, P., Managau, S., Mann, R. G., Marchant, J. M., Marconi, M., Marcos Santos, M. M. S., Marinoni, S., Marocco, F., Marshall, D. J., Martin Polo, L., Martín-Fleitas, J. M., Masip, A., Massari, D., Mastrobuono-Battisti, A., Mazeh, T., McMillan, P. J., Messina, S., Michalik, D., Millar, N. R., Mints, A., Molina, D., Molinaro, R., Molnár, L., Montegriffo, P., Mor, R., Morbidelli, R., Morel, T., Morris, D., Mulone, A. F., Munoz, D., Muraveva, T., Murphy, C. P., Musella, I., Noval, L., Ordénovic, C., Orrù, G., Osinde, J., Pagani, C., Pagano, I., Palaversa, L., Palicio, P. A., Panahi, A., Pawlak, M., Peñalosa Esteller, X., Penttilä, A., Piersimoni, A. M., Pineau, F. X., Plachy, E., Plum, G., Poggio, E., Poretti, E., Poujoulet, E., Prša, A., Pulone, L., Racero, E., Ragaini, S., Rainer, M., Raiteri, C. M., Rambaux, N., Ramos, P., Ramos-Lerate, M., Re Fiorentin, P., Regibo, S., Reylé, C., Ripepi, V., Riva, A., Rixon, G., Robichon, N., Robin, C., Roelens, M., Rohrbasser, L., Romero-Gómez, M., Rowell, N., Royer, F., Rybicki, K. A., Sadowski, G., Sagristà Sellés, A., Sahlmann, J., Salgado, J., Salguero, E., Samaras, N., Sanchez Gimenez, V., Sanna, N., Santoveña, R., Sarasso, M., Schultheis, M., Sciacca, E., Segol, M., Segovia, J. C., Ségransan, D., Semeux, D., Shahaf, S., Siddiqui, H. I., Siebert, A., Siltala, L., Slezak, E., Smart, R. L., Solano, E., Solitro, F., Souami, D., Souchay, J., Spagna, A., Spoto, F., Steele, I. A., Steidelmüller, H., Stephenson, C. A., Süveges, M., Szabados, L., Szegedi-Elek, E., Taris, F., Tauran, G., Taylor, M. B., Teixeira, R., Thuillot, W., Tonello, N., Torra, F., Torra, J., Turon, C., Unger, N., Vaillant, M., van Dillen, E., Vanel, O., Vecchiato, A., Viala, Y., Vicente, D., Voutsinas, S., Weiler, M., Wevers, T., Wyrzykowski, Ł., Yoldas, A., Yvard, P., Zhao, H., Zorec, J., Zucker, S., Zurbach, C., and Zwitter, T. (2021). Gaia Early Data Release 3. Summary of the contents and survey properties. *A&A*, 649:A1.
- [60] Galanti, B. and Tsinober, A. (2004). Is turbulence ergodic? *Physics Letters A*, 330(3-4):173–180.
- [61] Gan, Z., Li, H., Fu, X., and Du, S. (2022). On the Existence of Fast Modes in Compressible Magnetohydrodynamic Turbulence. *ApJ*, 926(2):222.
- [62] Girart, J. M., Rao, R., and Marrone, D. P. (2006). Magnetic Fields in the Formation of Sun-Like Stars. *Science*, 313(5788):812–814.
- [63] Goldreich, P. and Kylafis, N. D. (1981). On mapping the magnetic field direction in molecular clouds by polarization measurements. *ApJ*, 243:L75–L78.
- [64] Goldreich, P. and Kylafis, N. D. (1982). Linear polarization of radio frequency lines in molecular clouds and circumstellar envelopes. *ApJ*, 253:606–621.
- [65] Goldreich, P. and Sridhar, S. (1995). Toward a Theory of Interstellar Turbulence. II. Strong Alfvénic Turbulence. *ApJ*, 438:763.
- [66] Goldreich, P. and Sridhar, S. (1997). Magnetohydrodynamic Turbulence Revisited. *ApJ*, 485(2):680–688.
- [67] Goldsmith, P. F. (2013). Diffuse Molecular Cloud Densities from UV Measurements of CO Absorption. *ApJ*, 774(2):134.

- [68] Goldsmith, P. F., Heyer, M., Narayanan, G., Snell, R., Li, D., and Brunt, C. (2008). Large-Scale Structure of the Molecular Gas in Taurus Revealed by High Linear Dynamic Range Spectral Line Mapping. *ApJ*, 680(1):428–445.
- [69] Green, G. M., Schlafly, E. F., Finkbeiner, D., Rix, H.-W., Martin, N., Burgett, W., Draper, P. W., Flewelling, H., Hodapp, K., Kaiser, N., Kudritzki, R.-P., Magnier, E. A., Metcalfe, N., Tonry, J. L., Wainscoat, R., and Waters, C. (2018). Galactic reddening in 3D from stellar photometry - an improved map. *MNRAS*, 478(1):651–666.
- [70] Heiles, C. and Troland, T. H. (2003). The Millennium Arecibo 21 Centimeter Absorption-Line Survey. I. Techniques and Gaussian Fits. *ApJS*, 145(2):329–354.
- [71] Heitsch, F. and Hartmann, L. (2008). Rapid Molecular Cloud and Star Formation: Mechanisms and Movies. *ApJ*, 689(1):290–301.
- [72] Heitsch, F., Zweibel, E. G., Mac Low, M.-M., Li, P., and Norman, M. L. (2001). Magnetic Field Diagnostics Based on Far-Infrared Polarimetry: Tests Using Numerical Simulations. *ApJ*, 561(2):800–814.
- [73] Hennebelle, P. and Pérault, M. (1999). Dynamical condensation in a thermally bistable flow. Application to interstellar cirrus. *A&A*, 351:309–322.
- [74] Hensley, B. S., Zhang, C., and Bock, J. J. (2019). An Imprint of the Galactic Magnetic Field in the Diffuse Unpolarized Dust Emission. *ApJ*, 887(2):159.
- [75] Heyer, M., Gong, H., Ostriker, E., and Brunt, C. (2008). Magnetically Aligned Velocity Anisotropy in the Taurus Molecular Cloud. *ApJ*, 680(1):420–427.
- [76] Heyvaerts, J. and Priest, E. R. (1983). Coronal heating by phase-mixed shear Alfvén waves. *A&A*, 117:220–234.
- [77] Higdon, J. C. (1984). Density fluctuations in the interstellar medium: Evidence for anisotropic magnetogasdynamic turbulence. I - Model and astrophysical sites. *ApJ*, 285:109–123.
- [78] Hildebrand, R. H., Kirby, L., Dotson, J. L., Houde, M., and Vaillancourt, J. E. (2009). Dispersion of Magnetic Fields in Molecular Clouds. I. *ApJ*, 696(1):567–573.
- [79] Hill, A. S., Benjamin, R. A., Kowal, G., Reynolds, R. J., Haffner, L. M., and Lazarian, A. (2008). The Turbulent Warm Ionized Medium: Emission Measure Distribution and MHD Simulations. *ApJ*, 686(1):363–378.
- [80] Hiltner, W. A. (1949). Polarization of Light from Distant Stars by Interstellar Medium. *Science*, 109(2825):165.
- [81] Hoq, S., Clemens, D. P., Guzmán, A. E., and Cashman, L. R. (2017). Tracing the Magnetic Field of IRDC G028.23-00.19 Using NIR Polarimetry. *ApJ*, 836(2):199.
- [82] Houde, M. (2004). Evaluating the Magnetic Field Strength in Molecular Clouds. *ApJ*, 616(2):L111–L114.
- [83] Houde, M., Fletcher, A., Beck, R., Hildebrand, R. H., Vaillancourt, J. E., and Stil, J. M. (2013). Characterizing Magnetized Turbulence in M51. *ApJ*, 766(1):49.

- [84] Houde, M., Vaillancourt, J. E., Hildebrand, R. H., Chitsazadeh, S., and Kirby, L. (2009). Dispersion of Magnetic Fields in Molecular Clouds. II. *ApJ*, 706(2):1504–1516.
- [85] Hoyle, F. (1953). On the Fragmentation of Gas Clouds Into Galaxies and Stars. *ApJ*, 118:513.
- [86] Hull, C. L. H. and Zhang, Q. (2019). Interferometric observations of magnetic fields in forming stars. *Frontiers in Astronomy and Space Sciences*, 6:3.
- [87] Jeans, J. H. (1902). The Stability of a Spherical Nebula. *Philosophical Transactions of the Royal Society of London Series A*, 199:1–53.
- [88] Jiang, H., Li, H.-b., and Fan, X. (2020). Bayesian Revisit of the Relationship between the Total Field Strength and the Volume Density of Interstellar Clouds. *ApJ*, 890(2):153.
- [89] Kainulainen, J., Beuther, H., Henning, T., and Plume, R. (2009). Probing the evolution of molecular cloud structure. From quiescence to birth. *A&A*, 508(3):L35–L38.
- [90] Kainulainen, J. and Tan, J. C. (2013). High-dynamic-range extinction mapping of infrared dark clouds. Dependence of density variance with sonic Mach number in molecular clouds. *A&A*, 549:A53.
- [91] Kalberla, P. M. W. and Haud, U. (2018). Properties of cold and warm H I gas phases derived from a Gaussian decomposition of HI4PI data. *A&A*, 619:A58.
- [92] Kennicutt, Robert C., J. (1998a). Star Formation in Galaxies Along the Hubble Sequence. *ARA&A*, 36:189–232.
- [93] Kennicutt, Robert C., J. (1998b). The Global Schmidt Law in Star-forming Galaxies. *ApJ*, 498(2):541–552.
- [94] Körtgen, B. and Soler, J. D. (2020). The relative orientation between the magnetic field and gas density structures in non-gravitating turbulent media. *MNRAS*, 499(4):4785–4792.
- [95] Krumholz, M. R. (2014). The big problems in star formation: The star formation rate, stellar clustering, and the initial mass function. *PhR*, 539:49–134.
- [96] Krumholz, M. R. and Federrath, C. (2019). The Role of Magnetic Fields in Setting the Star Formation Rate and the Initial Mass Function. *Frontiers in Astronomy and Space Sciences*, 6:7.
- [97] Krumholz, M. R. and McKee, C. F. (2005). A General Theory of Turbulence-regulated Star Formation, from Spirals to Ultraluminous Infrared Galaxies. *ApJ*, 630(1):250–268.
- [98] Krumholz, M. R. and Tan, J. C. (2007). Slow Star Formation in Dense Gas: Evidence and Implications. *ApJ*, 654(1):304–315.
- [99] Kudoh, T. and Basu, S. (2003). Nonlinear Hydromagnetic Wave Support of a Stratified Molecular Cloud. *ApJ*, 595(2):842–857.
- [100] Kulsrud, R. M. (2005). *Plasma physics for astrophysics*.

- [101] Kuznetsova, A., Hartmann, L., and Ballesteros-Paredes, J. (2018). Kinematics and structure of star-forming regions: insights from cold collapse models. *MNRAS*, 473(2):2372–2377.
- [102] Lallement, R., Capitanio, L., Ruiz-Dern, L., Danielski, C., Babusiaux, C., Vergely, L., Elyajouri, M., Arenou, F., and Leclerc, N. (2018). Three-dimensional maps of interstellar dust in the Local Arm: using Gaia, 2MASS, and APOGEE-DR14. *A&A*, 616:A132.
- [103] Lazarian, A. and Hoang, T. (2007). Radiative torques: analytical model and basic properties. *MNRAS*, 378(3):910–946.
- [104] Lazarian, A., Yuen, K. H., and Pogosyan, D. (2022). Magnetic field strength from turbulence theory (I): Using differential measure approach (DMA). *arXiv e-prints*, page arXiv:2204.09731.
- [105] Lee, H. M. and Draine, B. T. (1985). Infrared extinction and polarization due to partially aligned spheroidal grains : models for the dust toward the BN object. *ApJ*, 290:211–228.
- [106] Leike, R. H. and Enßlin, T. A. (2019). Charting nearby dust clouds using Gaia data only. *A&A*, 631:A32.
- [107] Li, P. S., Lopez-Rodriguez, E., Ajeddig, H., André, P., McKee, C. F., Rho, J., and Klein, R. I. (2022). Mapping the magnetic field in the Taurus/B211 filamentary cloud with SOFIA HAWC + and comparing with simulation. *MNRAS*, 510(4):6085–6109.
- [108] Lim, J., Cho, J., and Yoon, H. (2020). Generation of Solenoidal Modes and Magnetic Fields in Turbulence Driven by Compressive Driving. *ApJ*, 893(1):75.
- [109] Lithwick, Y. and Goldreich, P. (2001). Compressible Magnetohydrodynamic Turbulence in Interstellar Plasmas. *ApJ*, 562(1):279–296.
- [110] Liu, J., Zhang, Q., Commercon, B., Valdivia, V., Maury, A., and Qiu, K. (2021). Calibrating the Davis-Chandrasekhar-Fermi method with numerical simulations: uncertainties in estimating the magnetic field strength from statistics of field orientations. *arXiv e-prints*, page arXiv:2106.09934.
- [111] Liu, J., Zhang, Q., and Qiu, K. (2022). Magnetic field properties in star formation: a review of their analysis methods and interpretation. *arXiv e-prints*, page arXiv:2208.06492.
- [112] Longcope, D. W. and Klapper, I. (1997). Dynamics of a Thin Twisted Flux Tube. *ApJ*, 488(1):443–453.
- [113] Mac Low, M.-M., Klessen, R. S., Burkert, A., and Smith, M. D. (1998). Kinetic energy decay rates of supersonic and super-alfvénic turbulence in star-forming clouds. *Phys. Rev. Lett.*, 80:2754–2757.
- [114] Magyar, N., Van Doorsselaere, T., and Goossens, M. (2019). The Nature of Elsässer Variables in Compressible MHD. *ApJ*, 873(1):56.

- [115] Malinen, J., Juvela, M., Zahorecz, S., Rivera-Ingraham, A., Montillaud, J., Arimatsu, K., Bernard, J. P., Doi, Y., Haikala, L. K., Kawabe, R., Marton, G., McGehee, P., Pelkonen, V. M., Ristorcelli, I., Shimajiri, Y., Takita, S., Tóth, L. V., Tsukagoshi, T., and Ysard, N. (2014). Multiwavelength study of the high-latitude cloud L1642: chain of star formation. *A&A*, 563:A125.
- [116] Malinen, J., Montier, L., Montillaud, J., Juvela, M., Ristorcelli, I., Clark, S. E., Berné, O., Bernard, J. P., Pelkonen, V. M., and Collins, D. C. (2016). Matching dust emission structures and magnetic field in high-latitude cloud L1642: comparing Herschel and Planck maps. *MNRAS*, 460(2):1934–1945.
- [117] Maron, J. and Goldreich, P. (2001). Simulations of Incompressible Magnetohydrodynamic Turbulence. *ApJ*, 554(2):1175–1196.
- [118] McKee, C. F. and Ostriker, E. C. (2007). Theory of Star Formation. *ARA&A*, 45(1):565–687.
- [119] McKee, C. F. and Ostriker, J. P. (1977). A theory of the interstellar medium: three components regulated by supernova explosions in an inhomogeneous substrate. *ApJ*, 218:148–169.
- [120] Mestel, L. and Spitzer, L., J. (1956). Star formation in magnetic dust clouds. *MNRAS*, 116:503.
- [121] Miville-Deschênes, M. A., Levrier, F., and Falgarone, E. (2003). On the Use of Fractional Brownian Motion Simulations to Determine the Three-dimensional Statistical Properties of Interstellar Gas. *ApJ*, 593(2):831–847.
- [122] Miville-Deschênes, M. A. and Martin, P. G. (2007). Physical properties of a very diffuse HI structure at high Galactic latitude. *A&A*, 469(1):189–199.
- [123] Mocz, P., Burkhart, B., Hernquist, L., McKee, C. F., and Springel, V. (2017). Moving-mesh Simulations of Star-forming Cores in Magneto-gravo-turbulence. *ApJ*, 838(1):40.
- [124] Molina, F. Z., Glover, S. C. O., Federrath, C., and Klessen, R. S. (2012). The density variance-Mach number relation in supersonic turbulence - I. Isothermal, magnetized gas. *MNRAS*, 423(3):2680–2689.
- [125] Molinari, S., Swinyard, B., Bally, J., Barlow, M., Bernard, J. P., Martin, P., Moore, T., Noriega-Crespo, A., Plume, R., Testi, L., Zavagno, A., Abergel, A., Ali, B., Anderson, L., André, P., Baluteau, J. P., Battersby, C., Beltrán, M. T., Benedettini, M., Billot, N., Blommaert, J., Bontemps, S., Boulanger, F., Brand, J., Brunt, C., Burton, M., Calzoletti, L., Carey, S., Caselli, P., Cesaroni, R., Cernicharo, J., Chakrabarti, S., Chrysostomou, A., Cohen, M., Compiegne, M., de Bernardis, P., de Gasperis, G., di Giorgio, A. M., Elia, D., Faustini, F., Flagey, N., Fukui, Y., Fuller, G. A., Ganga, K., Garcia-Lario, P., Glenn, J., Goldsmith, P. F., Griffin, M., Hoare, M., Huang, M., Ikhenade, D., Joblin, C., Joncas, G., Juvela, M., Kirk, J. M., Lagache, G., Li, J. Z., Lim, T. L., Lord, S. D., Marengo, M., Marshall, D. J., Masi, S., Massi, F., Matsuura, M., Minier, V., Miville-Deschênes, M. A., Montier, L. A., Morgan, L., Motte, F., Mottram, J. C., Müller, T. G., Natoli, P., Neves, J., Olmi, L., Paladini, R., Paradis, D., Parsons, H., Peretto, N., Pestalozzi, M., Pezzuto, S., Piacentini, F., Piazzi, L., Polychroni, D., Pomarès, M., Popescu, C. C., Reach,

- W. T., Ristorcelli, I., Robitaille, J. F., Robitaille, T., Rodón, J. A., Roy, A., Royer, P., Russeil, D., Saraceno, P., Sauvage, M., Schilke, P., Schisano, E., Schneider, N., Schuller, F., Schulz, B., Sibthorpe, B., Smith, H. A., Smith, M. D., Spinoglio, L., Stamatellos, D., Strafella, F., Stringfellow, G. S., Sturm, E., Taylor, R., Thompson, M. A., Traficante, A., Tuffs, R. J., Umana, G., Valenziano, L., Vavrek, R., Veneziani, M., Viti, S., Waelkens, C., Ward-Thompson, D., White, G., Wilcock, L. A., Wyrowski, F., Yorke, H. W., and Zhang, Q. (2010). Clouds, filaments, and protostars: The Herschel Hi-GAL Milky Way. *A&A*, 518:L100.
- [126] Monin, A. S. and I'Agglom, A. M. (1971). *Statistical fluid mechanics; mechanics of turbulence*.
- [127] Montgomery, D., Brown, M. R., and Matthaeus, W. H. (1987). Density fluctuation spectra in magnetohydrodynamic turbulence. *J. Geophys. Res.*, 92(A1):282–284.
- [128] Montgomery, D. and Turner, L. (1981). Anisotropic magnetohydrodynamic turbulence in a strong external magnetic field. *Physics of Fluids*, 24(5):825–831.
- [129] Mouschovias, T. C. (1976a). Nonhomologous contraction and equilibria of self-gravitating, magnetic interstellar clouds embedded in an intercloud medium: star formation. I. Formulation of the problem and method of solution. *ApJ*, 206:753–767.
- [130] Mouschovias, T. C. (1976b). Nonhomologous contraction and equilibria of self-gravitating, magnetic interstellar clouds embedded in an intercloud medium: star formation. I. Formulation of the problem and method of solution. *ApJ*, 206:753–767.
- [131] Mouschovias, T. C. (1976c). Nonhomologous contraction and equilibria of self-gravitating, magnetic interstellar clouds embedded in an intercloud medium: star formation. II. Results. *ApJ*, 207:141–158.
- [132] Mouschovias, T. C. (1976d). Nonhomologous contraction and equilibria of self-gravitating, magnetic interstellar clouds embedded in an intercloud medium: star formation. II. Results. *ApJ*, 207:141–158.
- [133] Mouschovias, T. C., Ciolek, G. E., and Morton, S. A. (2011). Hydromagnetic waves in weakly-ionized media - I. Basic theory, and application to interstellar molecular clouds. *MNRAS*, 415(2):1751–1782.
- [134] Mouschovias, T. C. and Spitzer, L., J. (1976). Note on the collapse of magnetic interstellar clouds. *ApJ*, 210:326.
- [135] Mouschovias, T. C., Tassis, K., and Kunz, M. W. (2006). Observational Constraints on the Ages of Molecular Clouds and the Star Formation Timescale: Ambipolar-Diffusion-controlled or Turbulence-induced Star Formation? *ApJ*, 646(2):1043–1049.
- [136] Myers, P. C. and Goodman, A. A. (1991). On the Dispersion in Direction of Interstellar Polarization. *ApJ*, 373:509.
- [137] Nguyen, H., Dawson, J. R., Lee, M.-Y., Murray, C. E., Stanimirović, S., Heiles, C., Miville-Deschênes, M. A., and Petzler, A. (2019). Exploring the Properties of Warm and Cold Atomic Hydrogen in the Taurus and Gemini Regions. *ApJ*, 880(2):141.

- [138] Orkisz, J. H., Pety, J., Gerin, M., Bron, E., Guzmán, V. V., Bardeau, S., Goicoechea, J. R., Gratier, P., Le Petit, F., Levrier, F., Liszt, H., Öberg, K., Peretto, N., Roueff, E., Sievers, A., and Tremblin, P. (2017). Turbulence and star formation efficiency in molecular clouds: solenoidal versus compressive motions in Orion B. *A&A*, 599:A99.
- [139] Ostriker, E. C., Stone, J. M., and Gammie, C. F. (2001). Density, Velocity, and Magnetic Field Structure in Turbulent Molecular Cloud Models. *ApJ*, 546(2):980–1005.
- [140] Oughton, S. and Matthaeus, W. H. (2020). Critical Balance and the Physics of Magnetohydrodynamic Turbulence. *ApJ*, 897(1):37.
- [141] Oughton, S., Priest, E. R., and Matthaeus, W. H. (1994). The influence of a mean magnetic field on three-dimensional magnetohydrodynamic turbulence. *Journal of Fluid Mechanics*, 280:95–117.
- [142] Padoan, P., Goodman, A., Draine, B. T., Juvela, M., Nordlund, Å., and Rögnerdsson, Ö. E. (2001). Theoretical Models of Polarized Dust Emission from Protostellar Cores. *ApJ*, 559(2):1005–1018.
- [143] Palmeirim, P., André, P., Kirk, J., Ward-Thompson, D., Arzoumanian, D., Könyves, V., Didelon, P., Schneider, N., Benedettini, M., Bontemps, S., Di Francesco, J., Elia, D., Griffin, M., Hennemann, M., Hill, T., Martin, P. G., Men'shchikov, A., Molinari, S., Motte, F., Nguyen Luong, Q., Nutter, D., Peretto, N., Pezzuto, S., Roy, A., Rygl, K. L. J., Spinoglio, L., and White, G. L. (2013). Herschel view of the Taurus B211/3 filament and striations: evidence of filamentary growth? *A&A*, 550:A38.
- [144] Panopoulou, G., Tassis, K., Blinov, D., Pavlidou, V., King, O. G., Paleologou, E., Ramaprakash, A., Angelakis, E., Baloković, M., Das, H. K., Feiler, R., Hovatta, T., Khodade, P., Kiehlmann, S., Kus, A., Kylafis, N., Liodakis, I., Mahabal, A., Modi, D., Myserlis, I., Papadakis, I., Papamastorakis, I., Pazderska, B., Pazderski, E., Pearson, T. J., Rajarshi, C., Readhead, A. C. S., Reig, P., and Zensus, J. A. (2015). Optical polarization map of the Polaris Flare with RoboPol. *MNRAS*, 452(1):715–726.
- [145] Panopoulou, G. V., Psaradaki, I., and Tassis, K. (2016). The magnetic field and dust filaments in the Polaris Flare. *MNRAS*, 462(2):1517–1529.
- [146] Passot, T. and Vázquez-Semadeni, E. (1998). Density probability distribution in one-dimensional polytropic gas dynamics. *Phys. Rev. E*, 58(4):4501–4510.
- [147] Passot, T. and Vázquez-Semadeni, E. (2003). The correlation between magnetic pressure and density in compressible MHD turbulence. *A&A*, 398:845–855.
- [148] Pattle, K. and Fissel, L. (2019). Submillimeter and Far-infrared Polarimetric Observations of Magnetic Fields in Star-Forming Regions. *Frontiers in Astronomy and Space Sciences*, 6:15.
- [149] Pattle, K., Fissel, L., Tahani, M., Liu, T., and Ntormousi, E. (2022). Magnetic fields in star formation: from clouds to cores. *arXiv e-prints*, page arXiv:2203.11179.

- [150] Pattle, K., Ward-Thompson, D., Berry, D., Hatchell, J., Chen, H.-R., Pon, A., Koch, P. M., Kwon, W., Kim, J., Bastien, P., Cho, J., Coudé, S., Di Francesco, J., Fuller, G., Furuya, R. S., Graves, S. F., Johnstone, D., Kirk, J., Kwon, J., Lee, C. W., Matthews, B. C., Mottram, J. C., Parsons, H., Sadavoy, S., Shinnaga, H., Soam, A., Hasegawa, T., Lai, S.-P., Qiu, K., and Friberg, P. (2017). The JCMT BISTRO Survey: The Magnetic Field Strength in the Orion A Filament. *ApJ*, 846(2):122.
- [151] Pelgrims, V., Ferrière, K., Boulanger, F., Lallement, R., and Montier, L. (2020). Modeling the magnetized Local Bubble from dust data. *A&A*, 636:A17.
- [152] Pillai, T., Kauffmann, J., Tan, J. C., Goldsmith, P. F., Carey, S. J., and Menten, K. M. (2015). Magnetic Fields in High-mass Infrared Dark Clouds. *ApJ*, 799(1):74.
- [153] Planck Collaboration, Ade, P. A. R., Aghanim, N., Alves, M. I. R., Arnaud, M., Arzoumanian, D., Ashdown, M., Aumont, J., Baccigalupi, C., Banday, A. J., Barreiro, R. B., Bartolo, N., Battaner, E., Benabed, K., Benoît, A., Benoit-Lévy, A., Bernard, J. P., Bersanelli, M., Bielewicz, P., Bock, J. J., Bonavera, L., Bond, J. R., Borrill, J., Bouchet, F. R., Boulanger, F., Bracco, A., Burigana, C., Calabrese, E., Cardoso, J. F., Catalano, A., Chiang, H. C., Christensen, P. R., Colombo, L. P. L., Combet, C., Couchot, F., Crill, B. P., Curto, A., Cuttaia, F., Danese, L., Davies, R. D., Davis, R. J., de Bernardis, P., de Rosa, A., de Zotti, G., Delabrouille, J., Dickinson, C., Diego, J. M., Dole, H., Donzelli, S., Doré, O., Douspis, M., Ducout, A., Dupac, X., Efstathiou, G., Elsner, F., Enßlin, T. A., Eriksen, H. K., Falceta-Gonçalves, D., Falgarone, E., Ferrière, K., Finelli, F., Forni, O., Frailis, M., Fraisse, A. A., Franceschi, E., Frejsel, A., Galeotta, S., Galli, S., Ganga, K., Ghosh, T., Giard, M., Gjerløw, E., González-Nuevo, J., Górski, K. M., Gregorio, A., Gruppuso, A., Gudmundsson, J. E., Guillet, V., Harrison, D. L., Helou, G., Hennebelle, P., Henrot-Versillé, S., Hernández-Monteagudo, C., Herranz, D., Hildebrandt, S. R., Hivon, E., Holmes, W. A., Hornstrup, A., Huppenberger, K. M., Hurier, G., Jaffe, A. H., Jaffe, T. R., Jones, W. C., Juvela, M., Keihänen, E., Keskitalo, R., Kisner, T. S., Knoche, J., Kunz, M., Kurki-Suonio, H., Lagache, G., Lamarre, J. M., Lasenby, A., Lattanzi, M., Lawrence, C. R., Leonardi, R., Levrier, F., Liguori, M., Lilje, P. B., Linden-Vørnle, M., López-Caniego, M., Lubin, P. M., Macías-Pérez, J. F., Maino, D., Mandolesi, N., Mangilli, A., Maris, M., Martin, P. G., Martínez-González, E., Masi, S., Matarrese, S., Melchiorri, A., Mendes, L., Mennella, A., Migliaccio, M., Miville-Deschênes, M. A., Moneti, A., Montier, L., Morgante, G., Mortlock, D., Munshi, D., Murphy, J. A., Naselsky, P., Nati, F., Netterfield, C. B., Noviello, F., Novikov, D., Novikov, I., Oppermann, N., Oxborrow, C. A., Pagano, L., Pajot, F., Paladini, R., Paoletti, D., Pasian, F., Perotto, L., Pettorino, V., Piacentini, F., Piat, M., Pierpaoli, E., Pietrobon, D., Plaszczynski, S., Pointecouteau, E., Polenta, G., Ponthieu, N., Pratt, G. W., Prunet, S., Puget, J. L., Rachen, J. P., Reinecke, M., Remazeilles, M., Renault, C., Renzi, A., Ristorcelli, I., Rocha, G., Rossetti, M., Roudier, G., Rubiño-Martín, J. A., Rusholme, B., Sandri, M., Santos, D., Savelainen, M., Savini, G., Scott, D., Soler, J. D., Stolyarov, V., Sudiwala, R., Sutton, D., Suur-Uski, A. S., Sygnet, J. F., Tauber, J. A., Terenzi, L., Toffolatti, L., Tomasi, M., Tristram, M., Tucci, M., Umana, G., Valenziano, L., Valiviita, J., Van Tent, B., Vielva, P., Villa, F., Wade, L. A., Wandelt, B. D., Wehus, I. K., Ysard, N., Yvon, D., and Zonca, A. (2016a). Planck intermediate results. XXXV. Probing the role of the magnetic field in the formation of structure in molecular clouds. *A&A*, 586:A138.
- [154] Planck Collaboration, Ade, P. A. R., Aghanim, N., Alves, M. I. R., Arnaud, M., Arzoumanian, D., Ashdown, M., Aumont, J., Baccigalupi, C., Banday, A. J., Barreiro,

- R. B., Bartolo, N., Battaner, E., Benabed, K., Benoît, A., Benoit-Lévy, A., Bernard, J. P., Bersanelli, M., Bielewicz, P., Bock, J. J., Bonavera, L., Bond, J. R., Borrill, J., Bouchet, F. R., Boulanger, F., Bracco, A., Burigana, C., Calabrese, E., Cardoso, J. F., Catalano, A., Chiang, H. C., Christensen, P. R., Colombo, L. P. L., Combet, C., Couchot, F., Crill, B. P., Curto, A., Cuttaia, F., Danese, L., Davies, R. D., Davis, R. J., de Bernardis, P., de Rosa, A., de Zotti, G., Delabrouille, J., Dickinson, C., Diego, J. M., Dole, H., Donzelli, S., Doré, O., Douspis, M., Ducout, A., Dupac, X., Efstathiou, G., Elsner, F., Enßlin, T. A., Eriksen, H. K., Falceta-Gonçalves, D., Falgarone, E., Ferrière, K., Finelli, F., Forni, O., Frailis, M., Fraisse, A. A., Franceschi, E., Frejsel, A., Galeotta, S., Galli, S., Ganga, K., Ghosh, T., Giard, M., Gjerløw, E., González-Nuevo, J., Górski, K. M., Gregorio, A., Gruppuso, A., Gudmundsson, J. E., Guillet, V., Harrison, D. L., Helou, G., Hennebelle, P., Henrot-Versillé, S., Hernández-Monteagudo, C., Herranz, D., Hildebrandt, S. R., Hivon, E., Holmes, W. A., Hornstrup, A., Huppenberger, K. M., Hurier, G., Jaffe, A. H., Jaffe, T. R., Jones, W. C., Juvela, M., Keihänen, E., Keskitalo, R., Kisner, T. S., Knoche, J., Kunz, M., Kurki-Suonio, H., Lagache, G., Lamarre, J. M., Lasenby, A., Lattanzi, M., Lawrence, C. R., Leonardi, R., Levrier, F., Liguori, M., Lilje, P. B., Linden-Vørnle, M., López-Caniego, M., Lubin, P. M., Macías-Pérez, J. F., Maino, D., Mandolesi, N., Mangilli, A., Maris, M., Martin, P. G., Martínez-González, E., Masi, S., Matarrese, S., Melchiorri, A., Mendes, L., Mennella, A., Migliaccio, M., Miville-Deschênes, M. A., Moneti, A., Montier, L., Morgante, G., Mortlock, D., Munshi, D., Murphy, J. A., Naselsky, P., Nati, F., Netterfield, C. B., Noviello, F., Novikov, D., Novikov, I., Oppermann, N., Oxborrow, C. A., Pagano, L., Pajot, F., Paladini, R., Paoletti, D., Pasian, F., Perotto, L., Pettorino, V., Piacentini, F., Piat, M., Pierpaoli, E., Pietrobon, D., Plaszczyński, S., Pointecouteau, E., Polenta, G., Ponthieu, N., Pratt, G. W., Prunet, S., Puget, J. L., Rachen, J. P., Reinecke, M., Remazeilles, M., Renault, C., Renzi, A., Ristorcelli, I., Rocha, G., Rossetti, M., Roudier, G., Rubiño-Martín, J. A., Rusholme, B., Sandri, M., Santos, D., Savelainen, M., Savini, G., Scott, D., Soler, J. D., Stolyarov, V., Sudiwala, R., Sutton, D., Suur-Uski, A. S., Sygnet, J. F., Tauber, J. A., Terenzi, L., Toffolatti, L., Tomasi, M., Tristram, M., Tucci, M., Umana, G., Valenziano, L., Valiviita, J., Van Tent, B., Vielva, P., Villa, F., Wade, L. A., Wandelt, B. D., Wehus, I. K., Ysard, N., Yvon, D., and Zonca, A. (2016b). Planck intermediate results. XXXV. Probing the role of the magnetic field in the formation of structure in molecular clouds. *A&A*, 586:A138.
- [155] Ponnada, S. B., Panopoulou, G. V., Butsky, I. S., Hopkins, P. F., Loebman, S. R., Hummels, C., Ji, S., Wetzel, A., Faucher-Giguère, C.-A., and Hayward, C. C. (2022). Magnetic Fields on FIRE: Comparing B-fields in the multiphase ISM and CGM of Simulated L_* Galaxies to Observations. *arXiv e-prints*, page arXiv:2206.04764.
- [156] Portillo, S. K. N., Slepian, Z., Burkhart, B., Kahraman, S., and Finkbeiner, D. P. (2018). Developing the 3-point Correlation Function for the Turbulent Interstellar Medium. *ApJ*, 862(2):119.
- [157] Salpeter, E. E. (1976). Planetary nebulae, supernova remnants, and the interstellar medium. *ApJ*, 206:673–678.
- [158] Schmidt, M. (1959). The Rate of Star Formation. *ApJ*, 129:243.
- [159] Schmidt, M. (1963). The Rate of Star Formation. II. The Rate of Formation of Stars of Different Mass. *ApJ*, 137:758.

- [160] Shebalin, J. V., Matthaeus, W. H., and Montgomery, D. (1983). Anisotropy in MHD turbulence due to a mean magnetic field. *Journal of Plasma Physics*, 29(3):525–547.
- [161] Skalidis, R., Sternberg, J., Beattie, J. R., Pavlidou, V., and Tassis, K. (2021a). Why take the square root? An assessment of interstellar magnetic field strength estimation methods. *A&A*, 656:A118.
- [162] Skalidis, R. and Tassis, K. (2021). High-accuracy estimation of magnetic field strength in the interstellar medium from dust polarization. *A&A*, 647:A186.
- [163] Skalidis, R., Tassis, K., Panopoulou, G. V., Pineda, J. L., Gong, Y., Mandarakas, N., Blinov, D., Kiehlmann, S., and Kypriotakis, J. A. (2021b). HI-H₂ transition: exploring the role of the magnetic field. *arXiv e-prints*, page arXiv:2110.11878.
- [164] Soler, J. D., Alves, F., Boulanger, F., Bracco, A., Falgarone, E., Franco, G. A. P., Guillet, V., Hennebelle, P., Levrier, F., Martin, P. G., and Miville-Deschênes, M. A. (2016). Magnetic field morphology in nearby molecular clouds as revealed by starlight and submillimetre polarization. *A&A*, 596:A93.
- [165] Soler, J. D., Hennebelle, P., Martin, P. G., Miville-Deschênes, M. A., Netterfield, C. B., and Fissel, L. M. (2013). An Imprint of Molecular Cloud Magnetization in the Morphology of the Dust Polarized Emission. *ApJ*, 774(2):128.
- [166] Springel, V. (2010). E pur si muove: Galilean-invariant cosmological hydrodynamical simulations on a moving mesh. *MNRAS*, 401(2):791–851.
- [167] Spruit, H. C. (2013). Essential Magnetohydrodynamics for Astrophysics. *arXiv e-prints*, page arXiv:1301.5572.
- [168] Sridhar, S. and Goldreich, P. (1994). Toward a Theory of Interstellar Turbulence. I. Weak Alfvénic Turbulence. *ApJ*, 432:612.
- [169] Stephens, I. W., Looney, L. W., Dowell, C. D., Vaillancourt, J. E., and Tassis, K. (2011). The Galactic Magnetic Field’s Effect in Star-forming Regions. *ApJ*, 728(2):99.
- [170] Tahani, M. (2022). Three-dimensional magnetic fields of molecular clouds. *Frontiers in Astronomy and Space Sciences*, 9:940027.
- [171] Tahani, M., Glover, J., Lupypciw, W., West, J. L., Kothes, R., Plume, R., Inutsuka, S., Lee, M. Y., Grenier, I. A., Knee, L. B. G., Brown, J. C., Doi, Y., Robishaw, T., and Haverkorn, M. (2022). Orion A’s complete 3D magnetic field morphology. *A&A*, 660:L7.
- [172] Tahani, M., Plume, R., Brown, J. C., and Kainulainen, J. (2018). Helical magnetic fields in molecular clouds?. A new method to determine the line-of-sight magnetic field structure in molecular clouds. *A&A*, 614:A100.
- [173] Tanaka, K. E. I., Tan, J. C., Zhang, Y., and Hosokawa, T. (2018). The Impact of Feedback in Massive Star Formation. II. Lower Star Formation Efficiency at Lower Metallicity. *ApJ*, 861(1):68.

- [174] Tang, Y.-W., Koch, P. M., Peretto, N., Novak, G., Duarte-Cabral, A., Chapman, N. L., Hsieh, P.-Y., and Yen, H.-W. (2019). Gravity, Magnetic Field, and Turbulence: Relative Importance and Impact on Fragmentation in the Infrared Dark Cloud G34.43+00.24. *ApJ*, 878(1):10.
- [175] Tassis, K. and Mouschovias, T. C. (2004). Ambipolar-Diffusion Timescale, Star Formation Timescale, and the Ages of Molecular Clouds: Is There a Discrepancy? *ApJ*, 616(1):283–287.
- [176] Tassis, K., Ramaprakash, A. N., Readhead, A. C. S., Potter, S. B., Wehus, I. K., Panopoulou, G. V., Blinov, D., Eriksen, H. K., Hensley, B., Karakci, A., Kypriotakis, J. A., Maharana, S., Ntormousi, E., Pavlidou, V., Pearson, T. J., and Skalidis, R. (2018). PASIPHAЕ: A high-Galactic-latitude, high-accuracy optopolarimetric survey. *arXiv e-prints*, page arXiv:1810.05652.
- [177] Tritsis, A., Panopoulou, G. V., Mouschovias, T. C., Tassis, K., and Pavlidou, V. (2015). Magnetic field-gas density relation and observational implications revisited. *MNRAS*, 451(4):4384–4396.
- [178] Tritsis, A. and Tassis, K. (2016). Striations in molecular clouds: streamers or MHD waves? *MNRAS*, 462(4):3602–3615.
- [179] Tritsis, A. and Tassis, K. (2018). Magnetic seismology of interstellar gas clouds: Unveiling a hidden dimension. *Science*, 360(6389):635–638.
- [180] Vazquez-Semadeni, E. (1994). Hierarchical Structure in Nearly Pressureless Flows as a Consequence of Self-similar Statistics. *ApJ*, 423:681.
- [181] Vázquez-Semadeni, E., Gómez, G. C., Jappsen, A. K., Ballesteros-Paredes, J., González, R. F., and Klessen, R. S. (2007). Molecular Cloud Evolution. II. From Cloud Formation to the Early Stages of Star Formation in Decaying Conditions. *ApJ*, 657(2):870–883.
- [182] Vázquez-Semadeni, E., Gómez, G. C., Jappsen, A. K., Ballesteros-Paredes, J., and Klessen, R. S. (2009). High- and Low-Mass Star-Forming Regions from Hierarchical Gravitational Fragmentation. High Local Star Formation Rates with Low Global Efficiencies. *ApJ*, 707(2):1023–1033.
- [183] Vázquez-Semadeni, E., Palau, A., Ballesteros-Paredes, J., Gómez, G. C., and Zamora-Avilés, M. (2019). Global hierarchical collapse in molecular clouds. Towards a comprehensive scenario. *MNRAS*, 490(3):3061–3097.
- [184] Wiebe, D. S. and Watson, W. D. (2004). Irregular Magnetic Fields and the Far-Infrared Polarimetry of Dust Emission from Interstellar Clouds. *ApJ*, 615(1):300–314.
- [185] Yang, L., Zhang, L., He, J., Tu, C., Li, S., Wang, X., and Wang, L. (2018). Coexistence of slow-mode and alfvén-mode waves and structures in 3d compressive MHD turbulence. *The Astrophysical Journal*, 866(1):41.
- [186] Yoon, H. and Cho, J. (2019). Effects of Turbulence Driving and Sonic Mach Number on the Davis-Chandrasekhar-Fermi Method. *ApJ*, 880(2):137.

-
- [187] Zamora-Avilés, M. and Vázquez-Semadeni, E. (2014). An Evolutionary Model for Collapsing Molecular Clouds and their Star Formation Activity. II. Mass Dependence of the Star Formation Rate. *ApJ*, 793(2):84.
- [188] Zuckerman, B. and Evans, N. J., I. (1974). Models of Massive Molecular Clouds. *ApJ*, 192:L149.
- [189] Zuckerman, B. and Palmer, P. (1974). Radio radiation from interstellar molecules. *ARA&A*, 12:279–313.
- [190] Zweibel, E. G. (1990). Magnetic Field Line Tangling and Polarization Measurements in Clumpy Molecular Gas. *ApJ*, 362:545.
- [191] Zweibel, E. G. (1996). Polarimetry and the Theory of the Galactic Magnetic Field. In Roberge, W. G. and Whittet, D. C. B., editors, *Polarimetry of the Interstellar Medium*, volume 97 of *Astronomical Society of the Pacific Conference Series*, page 486.

Appendix A

Dispersion function fitting

Table A.1 Fitting parameters of the HH09 method.

M_s	δ (pixel)	m	$b(0)$	Δ' (pixels)	N
0.7	15.5	0.0012	0.06	117	3.5
1.2	13.7	0.0016	0.07	117	3.4
2.2	13.1	0.0015	0.10	117	3.6
4.0	10.3	0.0009	0.12	108	4.2
7.0	8.6	0.0011	0.13	112	5.2

$b(0)$ is computed from equation (3.14).

The dispersion function fits for the models with $M_s = 1.2 - 7.0$ are shown in Fig. A.1. The best fit parameters for every model is given in Table A.1.

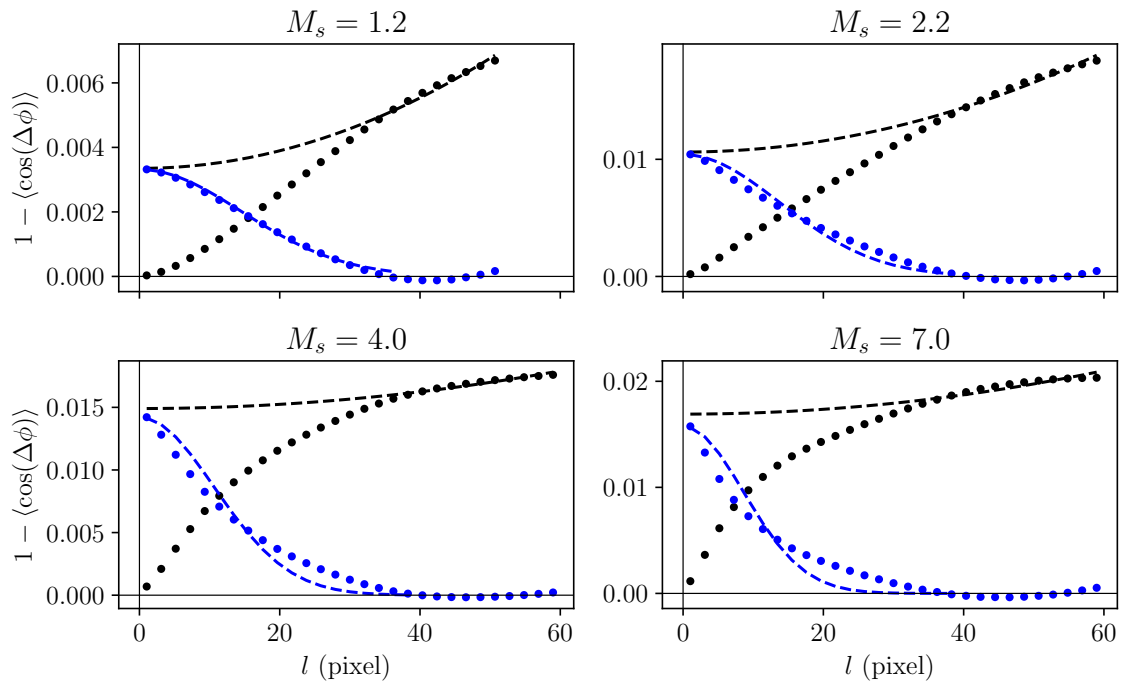


Fig. A.1 As in Fig. 6.3 for the simulation models with $M_s = 1.2 - 7.0$.